



TECHNISCHE
UNIVERSITÄT
WIEN



DISSERTATION

Spatial Consistency of 3D Channel Models

This dissertation is submitted for the degree of
"Doktor der Technischen Wissenschaften"

Dipl.-Ing. Fjolla Ademaj

Born March 29, 1989

Student ID: 1429883

July 2019

Faculty of Electrical Engineering and Information Technology
TU Wien

Advisor:

Univ. Prof. Dr.-Ing. Markus Rupp

Institute of Telecommunications
Technische Universität Wien
Vienna, Austria

Examiners:

Prof. Dr. Bernard H. Fleury

Department of Electronic Systems
Aalborg University
Aalborg, Denmark

Associate Prof. Ke Guan

School of Electronic and Information Engineering
Beijing Jiaotong University
Beijing, China

Abstract

Developing realistic channel models is one of the greatest challenges for describing wireless communications. Their quality is crucial for accurately predicting the performance of a wireless system. While on the one hand, channel models have to be accurate in describing the physical properties of wave propagation, on the other hand, they have to be as least complex as possible. With the recent emergence of antennas with a massive amount of elements as a promising technology for a further enhancement of spectral efficiency, new channel models that characterize the propagation environment in both azimuth and elevation become necessary. While standardization bodies such as 3rd Generation Partnership Project (3GPP) and International Telecommunications Unit (ITU) have introduced a 3-dimensional (3D) geometry-based stochastic channel model, a system-level modeling has been missing to serve the purpose of further analysis and evaluations. Furthermore, with such a channel characterization, where both geometry and statistics are jointly combined, it is crucial that spatial consistency is included in the model.

Facing the challenge of channel parameters being both position- and time-dependent, as well as the lack of spatial consistency, this dissertation presents a system-level framework and design of the 3D geometry-based stochastic channel models enhanced with spatial consistency.

In the first part of this dissertation, the design of the 3D geometry-based stochastic channel models (GSCMs) on an existing system-level tool is considered. The focus is put on modeling aspects of large-scale and small-scale fading being both position- and time-dependent, a challenge for the already complex structure of system-level tools. A novel design is proposed for spatial granularity and time line structure of simulation tools that reduces the simulation complexity and enables the generation of the channel impulse response at runtime. Furthermore, the proposed design facilitates the key functionality of wireless communications, mobility of the user and a time evolution of the channel impulse response while the user is on the move. It is shown that this structure is a key element in shaping the design of the upcoming fifth generation (5G) and beyond system-level tools.

Modeling of the spatial consistency is discussed in the second part of this dissertation. Two novel models are proposed: The first one establishes spatial correlation properties among propagation conditions such as line of sight (LOS), non line of sight (NLOS), indoors and outdoors based on 2-dimensional spatial filtering. Further it is shown that this model yields a realistic behavior mimicking the effects of blockages in 3D. The second model introduces spatially consistent small-scale fading. A correlation among random variables is proposed based on a specific resolution, namely the de-correlation distance, that indicates the range in which random variables are independent. Further, the model is validated by comparing to statistical measures extracted from extensive ray-tracing simulations. The proposed model is in a very good agreement with statistical channel properties obtained from ray-tracing. At the end, the proposed model is parametrized, and based on hypothesis testing the de-correlation distance values for various scenarios are determined.

Kurzfassung

Die Entwicklung realistischer Kanalmodelle ist eine der größten Herausforderungen für die Beschreibung der drahtlosen Kommunikation. Ihre Qualität ist entscheidend für die genaue Vorher sage der Leistungsfähigkeit eines drahtlosen Systems. Einerseits müssen die Kanalmodelle die physikalischen Eigenschaften der Wellenausbreitung genau beschreiben, andererseits müssen sie so unkompliziert wie möglich sein. Mit dem jüngsten Aufkommen von Antennen mit einer großen Anzahl von Elementen als vielversprechende Technologie zur weiteren Verbesserung der spektralen Effizienz werden neue Kanalmodelle erforderlich, die die Ausbreitungsumgebung sowohl im Azimut als auch in die Elevation charakterisieren. Da Standardisierungsgremien wie 3rd Generation Partnership Project (3GPP) und International Telecommunications Unit (ITU) ein 3-dimensional (3D) geometriebasiertes stochastisches Kanalmodell eingeführt haben, fehlt eine "System-Level" Modellierung, um weitere Analysen und Bewertungen durchführen zu können. Darüber hinaus ist es bei einer solchen Kanalcharakterisierung, bei der Geometrie und Statistik gemeinsam kombiniert werden, entscheidend, dass die räumliche Konsistenz in das Modell einbezogen wird.

Angesichts der Herausforderung, dass die Kanalparameter sowohl orts- als auch zeitabhängig sind, sowie der fehlenden räumlichen Konsistenz, präsentiert diese Dissertation ein "System-Level" Framework und das Design der 3D geometriebasierten stochastischen Kanalmodelle, die mit räumlichen Konsistenz erweitert sind.

Im ersten Teil dieser Dissertation wird das Design von 3D geometry-based stochastic channel models (GSCMs) auf einem vorhandenen Tool auf "System-Level" behandelt. Der Schwerpunkt liegt auf der Modellierung von Aspekten des orts- und zeitabhängigen großräumiges und kleinräumiges Fading, eine Herausforderung für die ohnehin komplexe Struktur auf "System-level" Tools. Es wird ein neuartiges Design für die räumliche Granularität und Zeitlinienstruktur von Simulationstool vorgeschlagen, das die Komplexität der Simulation verringert und die Erzeugung der Kanalimpulsantwort zur Laufzeit ermöglicht. Darüber hinaus erleichtert das vorgeschlagene Design die Schlüsselfunktionalität der drahtlosen Kommunikationen, die Mobilität des Benutzers und eine zeitliche Entwicklung der Kanalimpulsantwort, während der Benutzer in Bewegung ist. Es wird gezeigt, dass diese Struktur ein Schlüsselement bei der Gestaltung des Designs der System-Level Tools für die kommende fünfte Generation (5G) und darüber hinaus.

Die Modellierung der räumlichen Konsistenz wird im zweiten Teil dieser Dissertation diskutiert. Es werden zwei neue Modelle vorgeschlagen: Das erste erstellt räumliche Korrelationseigenschaften zwischen Ausbreitungsbedingungen wie line of sight (LOS), non line of sight (NLOS), drinnen und draußen basierend auf 2-dimensional (2D) räumlicher Filterung. Des Weiteren wird gezeigt, dass dieses Modell ein realistisches Verhalten liefert, das die Auswirkungen von Abschattungen in 3D nachahmt. Das zweite Modell führt ein räumlich gleichmäßiges kleinräumiges Fading ein. Eine Korrelation zwischen Zufallsvariablen wird vorgeschlagen, basierend auf einer bestimmten Auflösung, sogenannte Dekorrelationsentfernung, die den Bereich angibt, in dem Zufallsvariablen

unabhängig sind. Darüber hinaus wird das Modell durch Vergleich mit statistischen Maßen validiert, die aus umfangreichen Ray-Tracing Simulationen extrahiert wurden. Das vorgeschlagene Modell stimmt sehr gut mit den statistischen Kanaleigenschaften überein, die durch Ray-Tracing erhalten wurden. Am Ende wird das vorgeschlagene Modell parametrisiert und anhand von Hypothesentests die Dekorrelationsentfernungswerte für verschiedene Szenarien ermittelt.

Acknowledgments

First and foremost I want to express my deep gratitude to my advisor Prof. Markus Rupp for encouraging my research on wireless cellular networks and for sharing his profound technical and scientific knowledge. His guidance helped me in all the time of my doctoral studies. I am also thankful to Prof. Bernard H. Fleury and Prof. Ke Guan who agreed to review this thesis.

My thesis would not have been possible without the financial support of the Christian Doppler Laboratory together with the companies Kathrein (special thanks goes to Georg Schell, Ronald Gabriel and Gerd Saala), A1 (special thanks goes to Waltraud Müllner), and Nokia (special thanks goes to Gottfried Schnabl).

Throughout my doctoral studies, I had the pleasure to work with a great team of students and researchers that established the Vienna Cellular Communication Simulators, which are now applied all over the globe. I want to significantly thank Martin Taranetz and Stefan Schwarz for being always up for numerous fruitful discussions. Their feedback and constructive criticism greatly enhanced the quality of this work. Next, I want to thank my colleague and friend Martin Müller for the great times we spent preparing and correcting together as teaching assistants. A special thank goes to my dear friend Golsa for her friendship and kindness and Samira with whom I spent most of the time in the office sharing both stressful and joyful moments.

During a short visit as a research scholar at the Beijing Jiaotong University in China, I was given the opportunity to work with a great research group at the State Key Laboratory of Rail Traffic Control and Safety. I want to deeply thank Danping He for the great hospitality during my stay and all members of the lab for their friendliness and for making it such a great experience.

My acknowledgement would be incomplete without thanking the biggest source of my strength, my family. My dear parents Agim and Sahadete, my brother Gurakuq and my sister Vjosa for their unconditional support, care and love. The last word goes for my love, Taulant; I am truly thankful for having you in my life!

Contents

1. Introduction	1
1.1. Motivation and Scope of the Thesis	1
1.2. Outline and Contributions	3
1.3. Notation	6
2. System-level Modeling and Propagation Effects	7
2.1. Survey on Existing Simulation Tools	8
2.2. System-level Modeling	8
2.2.1. Physical Layer Modeling	9
2.2.2. Physical Layer Abstraction	10
2.3. Propagation Mechanisms	11
2.3.1. Propagation Models	11
2.3.2. Geometry-based Stochastic Channel Models	12
2.4. The 3-Dimensional Geometry-based Stochastic Channel Model	13
2.4.1. Path loss	14
2.4.2. Large-scale Fading	16
2.4.3. Small-scale Fading	16
3. System-Level Modeling of Geometry-based Stochastic Channel Model	19
3.1. GSCM 3D MIMO Channel Model in System-Level Tools	20
3.1.1. Procedure for Generating Channel Coefficients	21
3.1.2. Antenna Array Modeling	25
3.2. Spatial Granularity and Complexity Reduction	26
3.2.1. Time line Structure for fifth generation (5G) and Beyond Simulation Tools	29
3.3. System-level Performance Evaluation	31
3.3.1. Simulation Run Times	32
3.3.2. Throughput Performance Evaluation	35
3.4. Spatial Resolution of Antenna Arrays	39
3.4.1. System Model	40
3.4.2. Simulations	43
3.5. Summary	49
4. Modeling Spatial Correlation for Geometry-based Stochastic Channel Models	51
4.1. Introduction	52
4.1.1. Spatial Consistency Model	53
4.2. Modeling Spatially Correlated LOS/NLOS and Indoor/Outdoor state	54
4.2.1. Correlated LOS/NLOS State	54

Contents

4.2.2. Correlated Indoor/Outdoor State	57
4.2.3. Evaluation of Statistics	59
4.3. Modeling Spatially Correlated Small-scale Parameters	61
4.3.1. Correlated Random Variables	61
4.3.2. Statistical Properties	62
4.3.3. Spatially Correlated SSP Model	64
4.4. Summary	66
5. Statistical Evaluation of Spatial Consistency Model based on Ray-Tracing	69
5.1. Deterministic Model - Ray Tracing	70
5.2. Analysis of Spatial Consistency in a Typical Urban Scenario	72
5.2.1. System Model	73
5.2.2. Simulation Results	75
5.3. Statistical Evaluation of Spatially Correlated SSP Model	78
5.3.1. Statistical Analysis	78
5.3.2. Simulation Results	78
5.4. Model Parametrization	85
5.4.1. Hypothesis Testing	85
5.4.2. Results	86
5.5. Complementary Aspects	88
5.5.1. Computational Complexity	88
5.5.2. Correlation of Angular Sign	89
5.5.3. Frequency Impact on Spatial Correlation	90
5.6. Summary	91
6. Conclusions	93
6.1. Summary of Contributions	94
6.2. Open Issues and Outlook	95
6.3. Conclusion	96
A. List of Abbreviations	97
B. Calibration of the 3GPP 3D Channel Model	99
C. Angular Distributions	103
Bibliography	107

1

Introduction

1.1. Motivation and Scope of the Thesis

The multiple-input multiple-output (MIMO) technology, well-established by the time Long Term Evolution (LTE) was developed, was shown to be an effective means for improving capacity and reliability of wireless cellular communications through spatial multiplexing and transmit/receive antenna diversity, respectively. With at most eight active antenna ports per base station (BS), and a few antennas per mobile device, nowadays this technique can no longer satisfy the ever increasing data rate and latency requirements. A MIMO system with a large number of base station antennas, referred to as *massive* MIMO [51, 67, 39, 40] or as full dimension (FD)-MIMO, its official name in 3rd Generation Partnership Project (3GPP) [53, 78, 50], can provide enormous enhancements in spectral efficiency without the need for BS densification or degrading the power efficiency.

On the other hand, the requirement to achieve extremely high data rates, has motivated research in the millimeter-wave (mm-Wave) bands where numerous spectrum resources are available [66, 82]. What is common for both techniques, is the use of a large number of antenna elements, arranged as an antenna array. In massive MIMO systems, spectral efficiency is enhanced by serving many users in parallel over tailored minimally interfering 3-dimensional (3D) beams. For mm-Wave transmission, on the other hand, a large number of antenna elements is a prerequisite to compensate for the severe path loss caused when operating in such large frequency ranges. Figure 1.1 illustrates a typical urban environment, where users in various propagation conditions, i.e., outdoors, indoors, line of sight (LOS), non line of sight (NLOS), moving users are served by sharp beams.

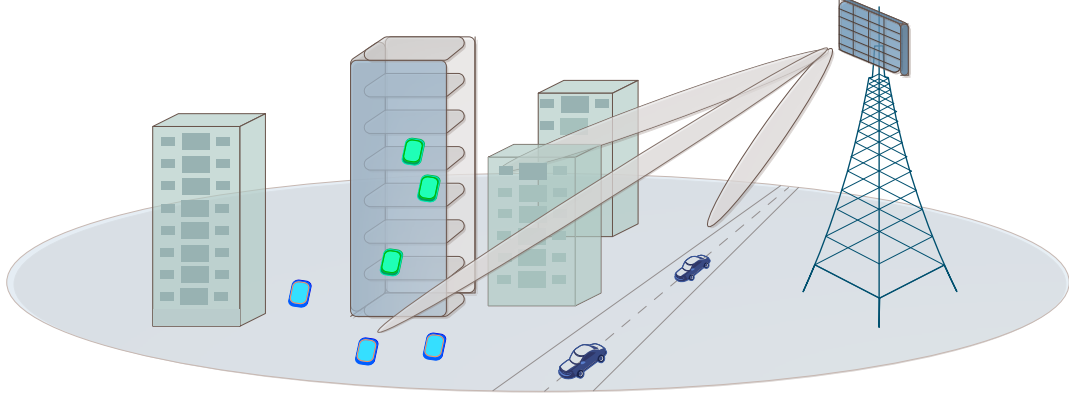


Figure 1.1.: System model comprising a single BS equipped with a 2-dimensional (2D) antenna array. Indoor users are denoted by green circles, outdoor users are indicated by red squares. ©2016 IEEE, [64].

A crucial component to enable the investigation of massive MIMO and beamforming are channel models that consider the propagation in both vertical (elevation) and horizontal (azimuth) directions, thus characterizing the propagation environment in three dimensions. To achieve this, the geometric structure of the antenna array and the propagation effects between transmitter and receiver, as well as, their positions in 3D space need to be reflected in the channel model. In this regard, a channel model that makes use of geometric information, such as the angular spread in azimuth and elevation as well as physical location and orientation of antenna arrays at transmitter and receiver, is essential.

Commonly, this channel model type is known as geometry-based stochastic channel model (GSCM) and is adopted by standardization bodies such as the 3GPP and International Telecommunications Union (ITU). The GSCM can be regarded as a balance between the two extremes of purely deterministic and purely stochastic channel modeling. While for purely deterministic modeling, i.e., ray tracing approaches, the simulated environment is completely deterministic, the GSCM reflects the statistics of a typical (urban, sub-urban, rural, etc.) environment. In contrast to purely stochastic modeling, which requires only the power delay profile (PDP) of the channel, the GSCM model introduces a larger set of parameters dependent on both spatial- and time domain characteristics and determines the effective PDP based on positions of random scattering objects.

Widely used geometry-based stochastic channel models are the 3GPP-Spatial Channel Model (SCM) specified in study item 3GPP TR25996 and the Wireless World Initiative New Radio (WINNER) channel model [18]. While these models are only defined for the azimuth dimension, an extension to 3D modeling including also the elevation angle was provided first, in the WINNER+ model and later, in the 3GPP 3D channel model [43, 72].

The GSCM follows the design based on the concept of *drops*, thus being suitable for system-level

tools, where simulations are performed in a sequence of drops¹. A drop is defined as one simulation run with a certain duration in time during which the random parameters defining the channel stay fixed. However, the drop concept is not applicable for GSCM, for the reason that it fails to accurately describe the physical channel properties, thus causing spatial inconsistency:

- within one drop, the location of scattering clusters is random and uncorrelated between different users (spatial locations). In this way, two users at almost the same location do not share similar environment characteristics, or similar clusters.
- for simulations incorporating movement, i.e., car and train scenarios, with GSCM there is no spatial consistency between consecutive snapshots of a moving user.

Therefore, for the utilization of the 3D GSCM in system-level tools, it is imperative to first solve the problem of *spatial consistency*. While, in literature there have been a few approaches how to cope with the issue of spatial consistency, they all have the tendency to go towards a deterministic or quasi-deterministic modeling. Examples of such approaches are the model introduced [18] and recently resolved in the quasi deterministic radio channel generator (QuaDRiGa) model [48], and the COST 2100 channel model, where a global set of scatterers is shared by all users through so-called visibility regions [32]. The main drawback of the deterministic approach is the high simulation complexity and large overhead that it imposes. Therefore such examples are only used as channel simulators and are not integrated on system-level tools. The main objective of this thesis is to model the spatial consistency and enhance the GSCM, without a further increase in simulation complexity.

The second issue that comes with the utilization of 3D GSCM in simulation tools is its high complexity that comes with the large number of parameters than need to be generated, when compared to simplistic PDP-based channel models. In simulation tools, it is always desirable to introduce accurate and realistic models, while keeping the complexity at minimum. At the end, channel models enable further investigations of various techniques and scenarios, therefore have to be practical. In particular, with the already complex system-level tools incorporating a large number network nodes, this thesis deals with designing a time line structure that allows for a reduction in complexity and incorporates an evolution of channel characteristics at simulation runtime.

1.2. Outline and Contributions

This section provides a short abstract of each chapter and exclusively refers to literature, which was published by the author.

¹In system-level several statistically independent drops are simulated in order to obtain a statistical representation of system performance.

Chapter 2: System-level Modeling and Propagation Effects

This chapter provides an overview on system-level modeling, focusing on the structure of a specific system-level tool. In the first part concepts of physical layer abstraction are discussed, whereas the second part emphasises propagation effects and modeling approaches of such effects. In particular, the focus is put in the description of geometry-based stochastic channel, that is considered throughout this thesis.

Chapter 3: System-Level Modeling of Geometry-based Stochastic Channel Model

Following the description of the system-level simulator introduced in the previous chapter, this chapter provides modeling aspects and the design of a 3D GSCM² in this simulator. Dealing with channel parameters that are both position- and time-dependent, a model on spatial granularity of the channel impulse response generation is introduced, and a new time line structure for the fifth generation (5G) of mobile communications and beyond simulation tools is proposed, allowing to simulate moving users and generate a continuous channel at runtime. The chapter next focuses on evaluating the simulation complexity when utilizing this specific channel model on the already-complex structure of system-level. In the last part, modeling of the antenna array is presented and a systematic procedure for evaluating the spatial resolution of 2D antenna arrays under realistic channel conditions is introduced.

The contributions of this chapter are published in the following papers:

- [i] F. Ademaj, M. Taranetz, and M. Rupp, “3GPP 3D MIMO Channel Model: A Holistic Implementation Guideline for Open Source SImulation Tools”, *EURASIP Journal on Wireless Communications and Networking*, vol. 2016, no. 1, p. 55, 2016. [Online]. Available: <https://doi.org/10.1186/s13638-016-0549-9>
- [ii] F. Ademaj, M. Taranetz, and M. Rupp, “Implementation, validation and application of the 3GPP 3D MIMO channel model in open source simulation tools”, in *2015 International Symposium on Wireless Communication Systems (ISWCS)*, 2015, pp. 721–725
- [iii] F. Ademaj, M. Taranetz, and M. Rupp, “Evaluating the spatial resolution of 2D antenna arrays for massive MIMO transmissions”, in *2016 24th European Signal Processing Conference (EUSIPCO)*, 2016, pp. 1995–1999
- [iv] M. K. Müller, F. Ademaj, T. Dittrich, A. Fastenbauer, B. R. Elbal, A. Nabavi, L. Nagel, S. Schwarz, and M. Rupp, “Flexible multi-node simulation of cellular mobile communications: The Vienna 5G System Level Simulator”, *EURASIP Journal on Wireless Communications and Networking*, vol. 2018, no. 1, p. 17, 2018

²Specifically, the 3GPP 3D channel model is considered [72].

Chapter 4: Modeling Spatial Correlation for Geometry-based Stochastic Channel Models

The GSCM model considered in Chapter 3, has not been designed for simulations requiring both spatio- and temporal properties of the channel, as massive MIMO and 3D beamforming. In this chapter, the GSCMs is enhanced by introducing a novel model for spatial consistency. With this model, propagation characteristics of two closely spaced users reflect a high correlation.

The contributions of this chapter are published in the following papers:

- [v] F. Ademaj, M. K. Müller, S. Schwarz, and M. Rupp, “Modeling of Spatially Correlated Geometry-Based Stochastic Channels”, in *2017 IEEE 86th Vehicular Technology Conference (VTC-Fall)*, 2017, pp. 1–6
- [vi] F. Ademaj, S. Schwarz, K. Guan, and M. Rupp, “Ray-Tracing based Validation of Spatial Consistency for Geometry-Based Stochastic Channels”, in *2018 IEEE 88th Vehicular Technology Conference (VTC-Fall)*, 2018, pp. 1–5

Chapter 5: Statistical Evaluation of Spatial Consistency Model based on Ray-Tracing

This chapter completes the picture of spatially consistent GSCM by first comparing the behaviour of the model in Chapter 4, with the performance evaluated by a ray-tracing tool. Second, the proposed model is validated statistically by comparing it with statistical channel properties from ray-tracing simulations. At the end, utilizing hypothesis testing over obtained ray-tracing statistics, the proposed model is parametrized for various 3GPP scenarios under LOS and NLOS propagation conditions.

The contributions of this chapter are published in the following papers:

- [vii] F. Ademaj, S. Schwarz, T. Berisha, and M. Rupp, “A Spatial Consistency Model for Geometry-based Stochastic Channels”, *submitted to IEEE Access*, 2019. [Online]. Available: <https://owncloud.nt.tuwien.ac.at/index.php/s/igAyCWNjRH3QFyL>
- [viii] F. Ademaj and S. Schwarz, “Spatial Consistency of Multipath Components in a Typical Urban Scenario”, in *European Conference on Antennas and Propagation (EuCAP)*, 2019, pp. 1–5

1.3. Notation

The following notation is used throughout this dissertation:

Symbol	Annotation
$\mathcal{U}(a, b)$	Uniform distribution on the interval (a, b)
$\mathcal{U}(\{-1, 1\})$	Uniform distribution on the discrete set $\{-1, 1\}$
$\mathcal{N}(\mu, \sigma^2)$	Normal distribution with mean μ and variance σ^2
p_{LOS}	Probability to be in LOS
$\tilde{\cdot}$	Correlated random variable
$\lceil \cdot \rceil$	Rounding to the next larger integer
g^{-1}	Mapping function
$\text{erf}(\cdot)$	Error function
ρ	Correlation coefficient
Cov	Covariance
Var	Variance
$d_{\text{3D}}^{(in)}$	Distance in 3D for the indoor area
$d_{\text{3D}}^{(out)}$	Distance in 3D for the outdoor area
PL	Path loss
τ_n	Delay of the n -th multipath
P_n	Power of the n -th multipath
ϕ	Azimuth angle
θ	Elevation angle
$G_{q,\phi}$	Antenna element field pattern in azimuth
$G_{q,\theta}$	Antenna element field pattern in elevation
$F_{p,\phi}$	Antenna field pattern in azimuth
$F_{p,\theta}$	Antenna field pattern in elevation
P_p	Total number of antenna elements in one array
Q	Number of antenna elements mapped to a single port

2

System-level Modeling and Propagation Effects

Performance evaluation is an important aspect in the development of mobile communication systems. Referring to the development of fourth generation (4G) of mobile communication systems, a global standard defined by International Telecommunication Union - Radiocommunication Sector (ITU-R), the set of requirements that this standard should fulfil is determined with the International Mobile Telecommunications (IMT)-Advanced specification [21]. Similarly, with IMT-2020, the overall roadmap for the development of fifth generation (5G) of mobile communications systems is established. These requirements, specified in IMT-Advanced and IMT-2020, include *analytical verifications* by conducting numerical calculations of peak spectral efficiency, latency and handover interruption times, and *performance evaluation by simulations* in regard to cell spectral efficiency, cell-edge user spectral efficiency, physical resource allocation, mobility etc., [33, 21]. While an analytical verification is achieved by means of calculations, simulations on the other hand, require modeling of wireless cellular communication systems.

Modeling in the context of wireless networks is in general a difficult task. The large size of the network, heterogeneity of network entities (i.e., base station (BS) types, user types), and all the physical effects of the transmit-receive chain that need to be considered lead to a complex system modeling. On the one hand, it is desirable to keep the computational costs at a minimum, while, on the other hand, it is crucial to preserve accuracy. A commonly employed solution, to reduce the simulation complexity, is to divide the simulations into two stages or levels of abstraction, known as link-level and system-level [33].

- *Link-level simulations* assess the performance of the physical layer and those higher layer aspects directly related to the radio interface. Mostly, only a single radio link is evaluated, rarely some few users. Commonly, they serve to study channel estimation, modulation and coding, feedback techniques, and multiple-input multiple-output (MIMO) performance [29, 89, 69].
- *System-level simulations* aim to evaluate the performance of a large network comprising a substantial number of BSs and users [22, 13]. Generally, system-level simulations are employed to evaluate the performance of scheduling and physical resource allocation [38, 24], the multi-user gains [26], mobility management, interference control, and network planning and optimization.

2.1. Survey on Existing Simulation Tools

There exist various system-level modeling tools that distinguish based on the implementation approach and those being specific for a certain technology. Many existing simulators can be seen as specific *modules* integrated in a larger suite of what is known as *network simulators*. Examples of such tools include the *Riverbed SteelCentral NetModeler* (formerly *OPNET Modeler Suite*) [57], *OMNeT++* [100], *GNS3* [93], *ns-2* [98], [99] [99], *IT++* [95], *Hurricane II* [94] and *openWNS* [23]. These solutions are packet oriented and model the full protocol stack or large parts of the protocol stack. However, a drawback of such simulators is the large computational complexity, which makes it difficult to utilize them for system-level simulations. There exist also system-level simulators specifically designed for a certain technology, i.e., LTE-Advanced (LTE-A) [31, 25, 97, 61] or 5G [55, 85, 87]. While, compared to the previous group, these tools provide a deeper level of details, still they vary largely in terms of complexity, usability, scalability and accessibility. Many of these simulators are developed by network operators and vendors, and thus typically are not intended for commercial distribution [55, 31, 25, 97, 61]. Subsequently, only a few simulation tools are openly available, including here technology-specific *LTE-Sim* [27], *Vienna LTE-A Downlink System-Level Simulator* [106], *Vienna 5G System-Level Simulator* [105].

The next section introduces the fundamental principles of system-level modeling and the interaction with link-level. As an example, the structure of the Vienna LTE-A Downlink System-Level Simulator and its successor, Vienna 5G System-Level Simulator is presented.

2.2. System-level Modeling

Simulating the physical layer across a large network consisting of many BSs and users becomes practically impossible [22]. Therefore, the approach of dividing simulations in two levels, *link-level*

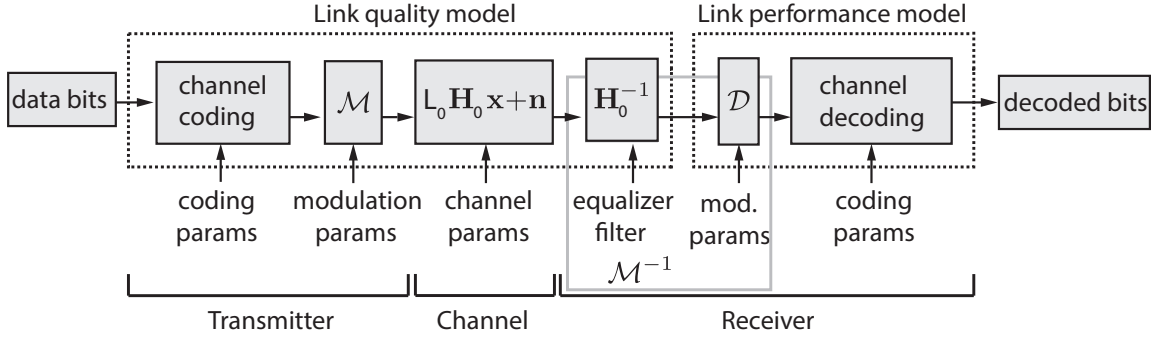


Figure 2.1: Generalized description of the PHY layer for applicable for LTE-A and 5G NR. The link between transmitter and receiver is separated into link quality- and link performance model [69].

and *system-level* has proved to be an efficient solution [33, 69]. In order to reduce the complexity of system-level simulations, the physical (PHY) layer is modeled in the link-level and then applied in system-level by means of an abstraction model, referred to as *physical layer abstraction*.

2.2.1. Physical Layer Modeling

This section provides a brief introduction into modeling concepts of the physical layer of LTE-A and 5G on system level. The LTE-A PHY layer procedure described by the bit-interleaved coded modulation (BICM)-system [37] is also robust for the description 5G new radio (NR) [71, 89], as indicated in Fig. 2.1. It consists of a transmitter including the channel coder, bit interleaver and the modulator denoted by \mathcal{M} . In the channel coder various coding schemes can be incorporated such as convolutional, turbo, low-density parity-check code (LDPC), and polar codes [89][Table 2]. The 5G NR as well as Long Term Evolution (LTE) relies on adaptive modulation and coding (AMC) in order to provide adaptability to the channel conditions. According to 3GPP [73], the cyclic prefix orthogonal frequency division multiplexing (OFDM) established for LTE-A, will also be the baseline multicarrier scheme applied in 5G. Still, in the development of link- and system-level tools, it is desirable to provide a flexible design that allows for implementation of various schemes, not only the standardized ones, but also novel schemes developed by researches [76, 79, 96, 88, 81]. For example, authors in [89] have shown a flexible modular structure of PHY layer modeling that allows for various schemes such as filtered-OFDM [42] and Filter-bank multicarrier (FBMC) [88, 80, 81].

The signal propagation over an $N_{\text{Tx}} \times N_{\text{Rx}}$ MIMO channel is commonly modeled by slowly-varying, position-dependent *large-scale fading* L_0 , *small-scale fading* \mathbf{H}_0 and additive white Gaussian noise (AWGN). The channel coefficients are typically calculated from classical power delay profile (PDP)-based channel models such as Vehicular-A [7] or Typical Urban (TU) [19], or by considering Rayleigh and Ricean fading. The receiver encompasses an equalizer filter and a demodulator (\mathcal{M}^{-1}) as well as

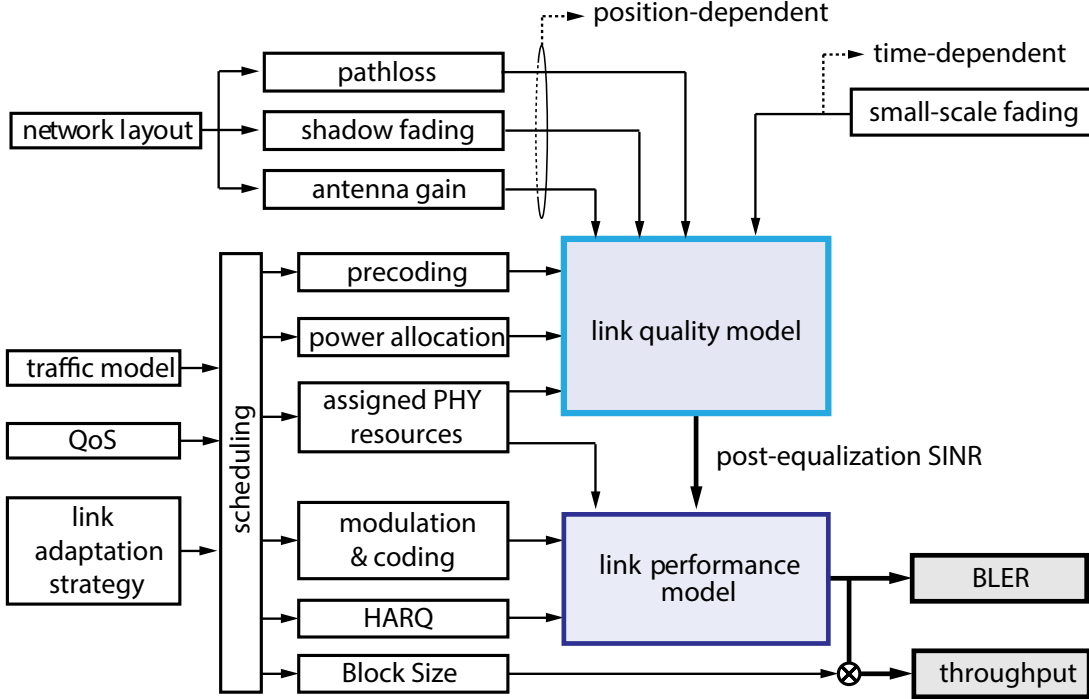


Figure 2.2.: Link abstraction model as employed in the Vienna 5G and LTE-A Downlink System-Level Simulator [69].

a decoder, which provides de-interleaving and channel decoding. Commonly, low-complexity models for equalizers are applied such as zero forcing (ZF)- and minimum mean-squared error (MMSE).

2.2.2. Physical Layer Abstraction

The abstraction of the PHY layer has to encompass the performance of a single link, given a set of input parameters, without performing all the PHY layer processing of the transmitter-receiver chain. This abstraction must be reasonably accurate, computationally simple, relatively independent of channel models, and extensible to interference models and multi-antenna processing methods.

The link quality model measures the quality of the received signal after equalization. Commonly, post-equalization signal to interference- and noise ratio (SINR) is the metric selected as output of the link quality model. Based on the post-equalization SINR of link quality model, the link performance model predicts the block-error ratio (BLER). From the BLER metric and based on the employed modulation and coding scheme (MCS), further parameters indicating the network performance are derived such as throughput and spectral efficiency. The translation from SINR-to-BLER is done by employing a mapping known in literature as *effective SINR mapping*. With this mapping, first the

received SINR values over allocated OFDM subcarriers are mapped to a single effective SINR value, which is then mapped to a BLER value. Based on the function utilized to map a vector of SINR values to a single *effective* SINR value, there exist several approaches for the *effective SINR mapping*. The one employed in the Vienna 5G and LTE-A Downlink System-Level Simulators is the so-called mutual information effective SINR mapping (MIESM) which is proved to be effective and accurate. A detailed description of the MIESM can be found in [37, 14].

Based on [69], the structure of system-level employing the PHY layer abstraction described above is illustrated in Fig. 2.2. The figure indicates the relation between link quality model and link performance model emphasising the most important input components applied to the two abstraction models. Apart from core structure of the PHY layer abstraction on system-level simulator, another very important aspect is modeling of the radio propagation effects between transmitter and receiver, referred to as *channel model*. The quality of the applied channel models is crucial for accurately predicting the performance of a wireless cellular network. Next section provides an overview on various existing channel models.

2.3. Propagation Mechanisms

The mechanisms which influence radio propagation are complex and diverse, and can generally be attributed to four basic propagation mechanisms [6]: free-space path loss, reflection, scattering and diffraction. The *free-space path loss* is the basic case of propagation, where between the transmitter and receiver only free-space is present. In a more realistic scenario, around transmitter and receiver various obstacles are present. *Reflections* occur when the propagating wave impinges on the smooth surface of an obstacle with dimensions much larger than the wavelength of the radio wave. If an obstacle has a rough surface, waves are *scattered*. Scattering causes a re-radiation of the impinged wave in many different directions. *Diffraction* occurs when the propagating wave between the transmitter and receiver is obstructed by an impenetrable body. Based on Huygen's principle, secondary waves are formed behind the obstacle even though there is no line of sight (LOS) between the transmitter and receiver.

2.3.1. Propagation Models

In the modeling of wireless communication systems, the aforementioned mechanisms are commonly captured by various channel models. A good characterization of the channel is an essential prerequisite for the development and evaluation of new technologies. Depending on the application and purpose of study, there exist several types of channel models. Following the specific approach of modeling, channel models can be classified into two large categories: analytical and physical models [16]. The analytical models describe the channel in a mathematical way without explicitly considering the wave

propagation properties. The effects of the wave propagation in the random scattering environment are rather condensed in statistical distributions of the channel coefficients. An example of analytical models is the well known Kronecker channel model used to characterize the correlation in-between transmit antennas and in-between receive antennas [10].

Physical models describe the channel between transmitter and receiver based on the electromagnetic properties of the environment. Physical models can again be categorized in three major groups, based on the modeling approach:

- Stochastic models: the physical channel parameters (e.g., power delay profile, angular profile) are determined in a completely stochastic way by prescribing probability distribution functions without assuming an underlying geometry. Examples of such models specified by 3rd Generation Partnership Project (3GPP) are Typical Urban, Pedestrian A and B, Vehicular A and B [83, 7].
- Deterministic models: the generation of channel parameters completely depends on the geometry of the environment, therefore channel characteristics are dependent on the applied scenario. Deterministic models are mostly represented by ray-tracing techniques [3].
- Geometry-based stochastic models: as indicated by its name, this channel model stands in between deterministic and purely stochastic models. While the geometry of transmitter and receiver is known, the environment in-between is not explicitly specified. In this way, multipaths are characterized with delay, power and direction of rays generated as a result of a random scattering environment. Such parameters are determined by means of statistical distributions that are parametrized from measurements. This model allows the separation of antenna parameters from propagation parameters, thus is convenient for the evaluation of massive MIMO systems and is frequently adopted by standardization bodies such as the 3GPP and International Telecommunications Union (ITU).

2.3.2. Geometry-based Stochastic Channel Models

The geometry-based stochastic channel model (GSCM) concept became important with the emergence of multi-antenna techniques in the early 2000s. Widely used GSCMs are the 3GPP Spatial Channel Model (SCM) specified in study item TR25996 [12] which supports a few scenarios, the extended version of 3GPP SCM (extended-SCM (ESCM)) which extends the SCM to more scenarios and larger bandwidths, and the Wireless World Initiative New Radio (WINNER) [15] which provides 15 different scenarios including urban-, rural- and moving environments.

In the aforementioned models the modeling of wave propagation is considered only in the horizontal direction, thus supporting beamforming only in the horizontal domain. With the introduction of *massive MIMO*, as a promising technology in 5G, a new channel model is required that considers

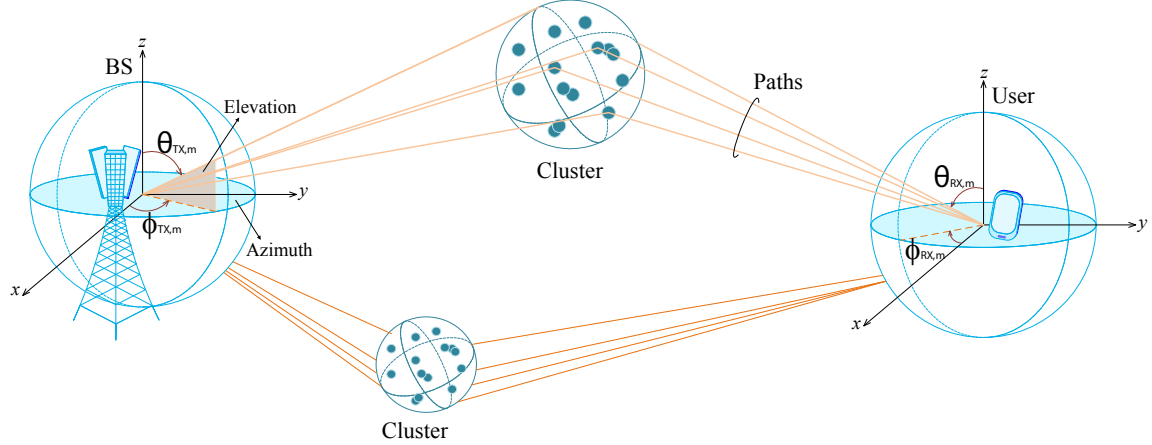


Figure 2.3.: Scattering concept in the 3D GSCM. The figure illustrates the propagation considering two clusters, each resolvable into a number of paths. Elevation and azimuth angles at the transmitter and receiver denoted as θ and ϕ , respectively.

the propagation in both vertical (elevation) and horizontal (azimuth) direction. To achieve this, the geometric structure of the antenna array and the propagation effects between transmitter and receiver, as well as, their positions in 3-dimensional (3D) space need to be reflected in the channel model.

2.4. The 3-Dimensional Geometry-based Stochastic Channel Model

The concept of a geometry-based stochastic channel model for a link between a transmitter and a receiver is shown in Fig. 2.3, where scattering regions, referred to as clusters, are represented by large circles comprising several scattering objects. Each cluster contains several rays and the number of clusters and rays varies for different scenarios and propagation conditions.

The deterministic part of the model is represented by modeling of the path loss, whereas the stochastic part of the model is determined by two levels of randomness:

- large-scale parameter (LSP): define parameters such as the root mean square (RMS) delay spread, angular spread of departure- and arrival in azimuth and elevation, shadow fading and K-Ricean factor, which mostly change prominently over larger distances (i.e., larger than several wavelengths). In a multi-link scenario, correlation properties that describe variations of LSPs over distance have to be considered. That is, the LSPs of two user links towards the same BS would experience correlations that are proportional to the relative distance between

the two users. Commonly, this is achieved by considering the LSPs as correlated multivariate random process [18].

- small-scale parameter (SSP): characterize the actual multipath components by means of delay, power and angular values. The principle of generating multipath components follows a random scattering environment determined by several distributions and statistics of correlated LSPs. For instance, an exponential delay distribution with a specific RMS delay spread derived from correlated LSPs is commonly applied to determine the multipath delays.

In the reminder of this chapter, the 3GPP 3D channel model is considered, discussing its main modeling concepts.

2.4.1. Path loss

The 3GPP 3D channel model specifies three propagation conditions, LOS, non line of sight (NLOS) and outdoor-to-indoor (O-to-I). The probability of being in LOS is determined for a specific scenario, i.e., urban or rural. For example, for the urban micro cell (UMi) scenario, the LOS probability follows

$$p_{\text{LOS}}(d_{2\text{D}}^{(\text{out})}) = \begin{cases} 1, & d_{2\text{D}}^{(\text{out})} \leq 18 \text{ m} \\ \frac{18}{d_{2\text{D}}^{(\text{out})}} + \exp\left(-\frac{d_{2\text{D}}^{(\text{out})}}{63}\right) \left(1 - \frac{18}{d_{2\text{D}}^{(\text{out})}}\right), & d_{2\text{D}}^{(\text{out})} > 18 \text{ m} \end{cases}, \quad (2.1)$$

where $d_{2\text{D}}^{(\text{out})}$ denotes the distance between BS and user projected on the earth surface (2D or azimuth), as illustrated in Fig. 2.4.

For the case of a macro BS where the BS height is larger (25 m according to the 3GPP), represented by urban macro cell (UMa) scenario, the LOS probability depends on the height of the user, height of the BS and their corresponding distance.

Based on the propagation condition, the experienced path loss can be defined as

$$\text{PL} = \text{PL}\left(d_{3\text{D}}^{(\text{out})} + d_{3\text{D}}^{(\text{in})}\right) + \beta_w + \text{PL}\left(d_{2\text{D}}^{(\text{in})}\right), \quad (2.2)$$

where the first term represents the path loss experienced on the overall distance between BS and user, the second term β_w denotes the loss through wall if the user is indoors, and the third term represents the additional losses due to distance, inside the building where the user is located. The distance $d_{2\text{D}}^{(\text{in})}$ represents the distance of indoor user from the outer wall of the building as is assumed uniformly distributed between 0 and 25 m. Each of terms can then be individually modeled and are scenario specific.

2.4. The 3-Dimensional Geometry-based Stochastic Channel Model

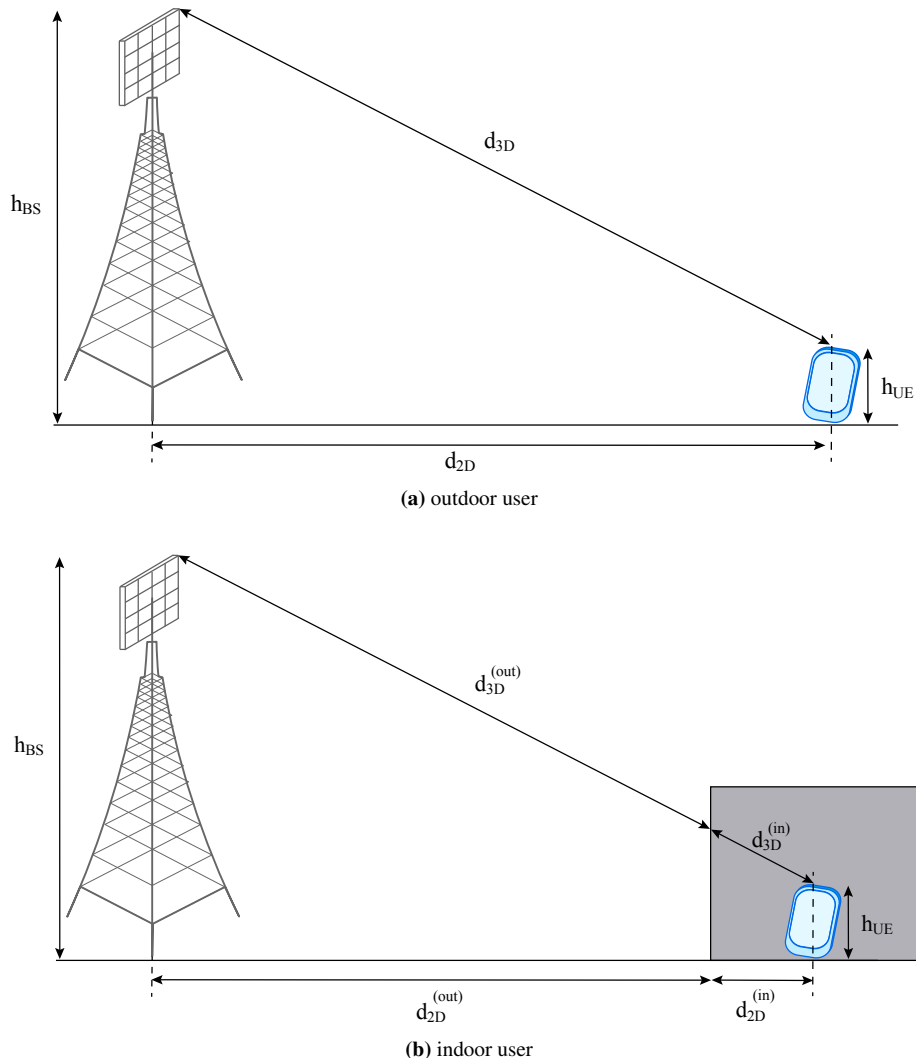


Figure 2.4.: Definition of distances between BS and user considering azimuth and elevation dimensions, according to [43].

2.4.2. Large-scale Fading

The variations of the signal propagation along transmission path are described by second order statistics commonly represented by shadow fading, delay spread and angular distributions, that are referred as LSPs. They are considered as an average over a typical channel i.e., distance of some tens of wavelengths. In the 3GPP 3D channel model, LSPs are modeled as log-normally distributed random variables with mean and variance parametrized for a specific environment. A parametrization of mean and variance for LSPs is done based on measurements and can be found in [43][Table 7.3-6].

LSPs are used as control parameters for the generation of SSPs.

2.4.3. Small-scale Fading

The SSPs incorporate delays, cluster powers as well as angles of departure and -arrival in azimuth and elevation direction, respectively thus describing multipath components. The 3GPP 3D channel model considers N clusters of scatterers, where each cluster is resolvable to M paths. For describing the propagation path between transmitter and receiver, only the last bounce of scatterers is considered in the model for arrival angles. Similarly, only the first bounce of scatterers for departure angles is assumed.

The multipath components for n th cluster are modeled as follows:

- Delay,

$$\tau_n = -r_\tau \sigma_{\text{DS}} \ln(X_n), \quad (2.3)$$

where r_τ is the delay proportionality factor, σ_{DS} denotes the delay spread derived from LSP statistics, $n = 1, \dots, N$ is the cluster index and $X_n \sim \mathcal{U}(0, 1)$ is a random variable representing the randomness of delay over multiple paths.

- Power,

$$P_n = \exp\left(-\tau_n \frac{r_\tau - 1}{r_\tau \sigma_{\text{DS}}}\right) 10^{\frac{-Z_n}{10}}, \quad (2.4)$$

where $Z_n \sim \mathcal{N}(0, \zeta^2)$ is the shadowing term per cluster with variance ζ^2 .

- Directions in azimuth are modeled as inverse Gaussian with probability distribution function

$$\phi'_{n,\text{AoA}} = \frac{2\sigma_{\text{ASA}}/1.4\sqrt{-\ln(P_n/\max(P_n))}}{C_\phi}, \quad (2.5)$$

2.4. The 3-Dimensional Geometry-based Stochastic Channel Model

where σ_{ASA} denotes the LSP of angular spread, and C_ϕ is defined as a scaling factor related to the total number of clusters, i.e., for $N = 20$, $C_\phi = 1.289$. The azimuth angles are then calculated according to

$$\phi_{n,\text{AoA}} = X_n \phi'_{n,\text{AoA}} + Y_n + \phi_{\text{LOS},\text{AoA}}, \quad (2.6)$$

where $X_n \sim \mathcal{U}(\{1, -1\})$ is a random variable applied to assign positive and negative sign to the angles, and variable $Y_n \sim \mathcal{N}(0, (\sigma_{\text{ASA}}/7)^2)$ additionally introduces random variation. The parameter $\phi_{\text{LOS},\text{AoA}}$ denotes the LOS angle defined from geometry.

- Directions in elevation follow a Lapacian distribution

$$\theta'_{n,\text{EoA}} = \frac{-\sigma_{\text{ESA}} \ln(P_n / \max(P_n))}{C_\theta}, \quad (2.7)$$

where σ_{ESA} is the LSP angular spread for elevation angle and C_θ is defined as a scaling factor for elevation proportional to the number of clusters, similar to the azimuth case. Further, with the given distribution, elevation angles are calculated as

$$\theta_{n,\text{EoA}} = X_n \theta'_{n,\text{EoA}} + Y_n + \theta_{\text{LOS},\text{EoA}}, \quad (2.8)$$

where similar to the azimuth case, $X_n \sim \mathcal{U}(\{1, -1\})$ is a random variable applied to assign positive and negative sign to the angles, and variable $Y_n \sim \mathcal{N}(0, (\sigma_{\text{ESA}}/7)^2)$ additionally introduces random variation. The LOS angle defined from geometry is denoted by $\theta_{\text{LOS},\text{EoA}}$.

3

System-Level Modeling of Geometry-based Stochastic Channel Model

In this chapter, the system-level modeling of a 3-dimensional (3D) geometry-based stochastic channel model (GSCM) is studied. The main target is to achieve an efficient design and adjustment of the highly complex 3D GSCM when integrating it in system-level tools.

Antennas with a massive amount of elements at one end are among fifth generation (5G) mobile communication key technologies for which spectral efficiency is enhanced by serving many users in parallel over tailored minimally interfering beams. Existing work on directional beamforming mostly assumes simplistic signal propagation characteristics under line of sight (LOS) conditions, where only log-distance dependent path loss is taken into account, while the impact of the channel is not considered [34, 36, 50, 39, 58, 60]. Nevertheless, the channel will alter the beam and, hence, considerably impact the achievable spatial resolution of the antenna array. Thus, for the evaluation of massive multiple-input multiple-output (MIMO) technology, it is important to consider channel models, that characterize the propagation environment in both azimuth and elevation.

Motivated by the need for evaluation of massive MIMO and 3D beamforming on simulation tools, at the beginning of 2015, 3rd Generation Partnership Project (3GPP) introduced a 3D GSCM model specified in Technical Report TR36873 [43], subsequently denoted as 3GPP 3D channel model. Yet, only few simulation studies, including reports from the 3GPP TSG RAN WG1 meetings, have been published that claim the practical implementation of the model [47, 49]. Moreover, the employed tools are mainly developed by network operators and vendors, and thus typically intended for commercial use.

My work in [54] is the first to provide a guideline for the practical implementation of the GSCM 3D model specified with 3GPP TR36873. The MATLAB source code is (since 2015) openly available for download under an academic, noncommercial use license. It is provided as a stand-alone package in [90] and is also part of the Vienna Cellular Communication Simulators (link- and system-level simulators) [106]. The 3GPP 3D channel model implementation has experienced more than 500 users worldwide. I believe that open access is a key prerequisite for reproducible simulation studies, and hope to inspire researchers and developers of link- and system-level simulation tools to further elaborate on these topics by directly applying or reusing my implementation approach.

Based on my work in [54, 63, 64, 87], the contributions of this chapter are:

- Design of the integration of the 3D GSCM on system-level tools. The focus is on modeling aspects of large and small-scale fading being position and time dependent, a challenge for the already complex structure of system-level tools. A novel design is proposed for spatial granularity and time line structure of simulation tools that reduces the simulation complexity and enables the generation of the channel impulse response at runtime. It is shown that this structure is a key element in shaping the design of new 5G system-level tools.
- The impact of modeling both the desired as well as the interfering channels with the 3D GSCM is investigated. A comparison to the simplistic Rayleigh fading is carried out, indicating that simple channel models may underestimate the achievable performance. Furthermore, the dependency of the simulation complexity on the size of antenna arrays as well as on the number of users and base stations (BSs) is investigated.
- Investigation of the achievable spatial resolution of beams in vertical direction when using large antenna arrays. A systematic procedure is introduced to evaluate the spatial resolution of 2-dimensional (2D) antenna arrays in a 3GPP consistent scenario under realistic channel conditions. Particularly, the focus lies on evaluating the channel energy and the average throughput of typical indoor and outdoor users by means of system-level simulations.

3.1. GSCM 3D MIMO Channel Model in System-Level Tools

In this section, modeling aspects on how to integrate the 3GPP 3D channel model into system-level tools are discussed. I consider the system-level model from Section 2.2, which is also a generic model and common for system-level tools [33].

Given the time-frequency structure of a system, i.e., Long Term Evolution (LTE) standard, in system-level simulator channel realizations are commonly generated per physical resource block (RB) and subframe (subsequently also denoted as transmission time interval (TTI)) [61]. On the other hand, on link-level, channel realizations are typically calculated per orthogonal frequency division multiplexing (OFDM) symbol and LTE subcarrier [41]. For the GSCM case, the target is to compute

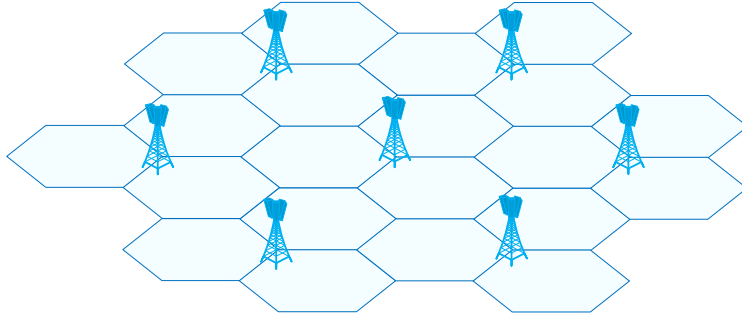


Figure 3.1.: Hexagonal-grid macro-cell scenario with seven macro BS, each three-sectorized.

a $N_{Rx} \times N_{Tx}$ MIMO-channel matrix $\mathbf{H}(t, f)$ for each sampling point on the time-frequency grid, where N_{Tx} and N_{Rx} refer to the number of transmit- and receive antenna *ports*, respectively [61].

In the 3GPP 3D channel model, the channel coefficients depend on the geometry, respectively on the transmitter and receiver locations in the 3D space and, thus, have to be calculated *at runtime*. The calculation complexity directly scales with the number of links that depends on the number of transmitters and receivers. For example, considering a typical cellular network with hexagonally arranged and sectorized macro-sites as illustrated in Fig. 3.1, the number of channel coefficients for a 4×4 MIMO configuration, that needs to be generated in each time instant of the simulation is 1.41×10^8 , assuming 21 BS sectors and 50 users per base station sector. Hence, in order to reduce complexity, the challenge is to perform computationally intensive tasks *off-line* or *on demand*, whenever possible. In addition, modeling of interfering channels introduces a further increase in the complexity. In view of this, a complexity reduction can be achieved by neglecting the contribution of those interferers that have a received power below a certain threshold (e.g., the noise power).

3.1.1. Procedure for Generating Channel Coefficients

Next, following the stepwise procedure¹ as specified in [43, Sec. 7.3] and illustrated in Fig. 3.2, I will explain its expedient partition for implementation on system-level tools. In the remainder of this chapter, only the downlink is considered. Since the channel model from [43] is applicable for both uplink and downlink, the notions transmitter and receiver interchangeably refer to the antenna elements of the BSs and the users, respectively.

¹The steps are denoted as *Step N* with $N \in \{1, \dots, 12\}$.

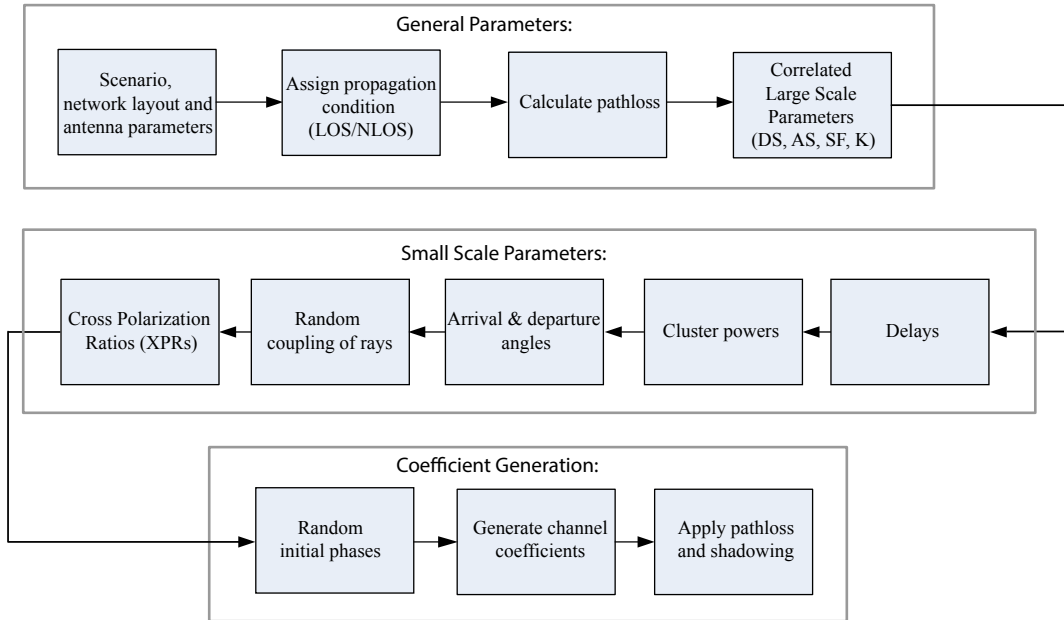


Figure 3.2.: Procedure for generating channel coefficients in the 3GPP 3D channel model.

General Parameters

Referring to the procedure for generating channel coefficients in the 3GPP 3D channel model, the first step is to generate the *general parameters*. It starts with specifying the network layout, the scenario environment and the antenna array parameters (*Step 1*). Currently, the standard specifies three scenarios, 3D-urban macro cell (UMa), 3D-urban micro cell (UMi) and 3D-rural macro cell (RMa), and various planar antenna array structures, defining the location and polarization of each antenna element, as well as the element-to-port mapping. *Step 2* is to assign the propagation condition, i.e., either LOS or non line of sight (NLOS), separately for indoor and outdoor users. The decision is based on the LOS probability as specified in [43, Tab. 7.2-2], which is dependent on the user's height and its distance to the BS. Different path loss models are applied for LOS, NLOS and outdoor-to-indoor (O-to-I), as defined in [43, Tab. 7.2-1]. The experienced path loss is calculated in *Step 3*. In *Step 4*, the large-scale parameters (LSPs) are generated. In the following, a detailed description of *Step 4* is presented.

Generation of LSPs

The LSPs define parameters such as the root mean square (RMS) delay spread, angular spread of departure- and arrival in azimuth and elevation, shadow fading and K-Ricean factor, which mostly change prominently over larger distances (i.e., larger than several wavelengths). In the system-level simulator, with the presence of multiple links, the correlation properties that describe variations of

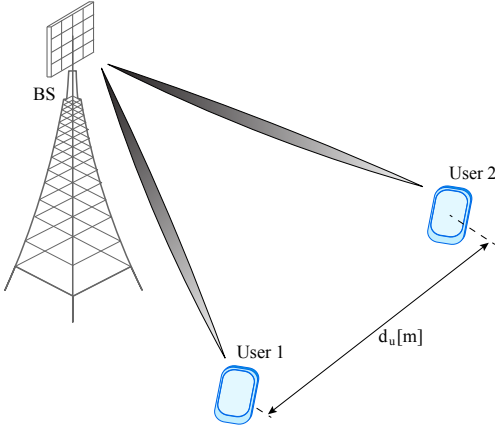


Figure 3.3.: Auto-correlation of LSPs: links toward the same BS experience correlations that are proportional to user's relative distance, denoted by d_u .

LSPs over distance have to be considered. For instance, the LSPs of two user links towards the same BS would experience correlations that are proportional to the relative distance between the two users, as illustrated in Fig. 3.3. This correlation, known as auto-correlation, is often modeled such that it reflects an exponential decay over distance. Additionally, there exists an inter-dependency between LSPs itself (e.g., cross-correlation between delay spread and shadow fading term), that is described with the cross-correlation coefficient measure. The 3GPP 3D channel model follows the approach presented in [18, Sec. 3.3.1], where a detailed procedure on how to generate cross-correlation and auto-correlation of LSPs is described.

According to several investigations reported in literature [9, 11, 15], the correlation properties of links from the same user toward multiple BSs are considered to be zero. Several results from different measurement campaigns could not show a clear behaviour of correlation between different BSs, therefore no correlation is assumed. Consequently, on system-level modeling, the generation of LSPs is performed per BS. If a BS serves more than one user, both auto-correlation and cross-correlation are considered. Whereas for a scenario with a single user, only cross-correlation is applied. Similarly, for interfering links only cross-correlation is employed. On the other hand, for sectorized BSs, links from different sectors of the same BS to a user are considered to have the same correlated LSP. In this way, for each user the correlated LSPs consist of LSPs for desired and interfering links and can be represented by the matrix

$$\mathbf{M}_{\text{LSP}} = \begin{bmatrix} \delta_{0,\text{SF}} & \delta_{0,\text{K}} & \delta_{0,\text{DS}} & \delta_{0,\text{ASD}} & \cdots & \delta_{0,\text{ESA}} \\ \delta_{1,\text{SF}} & \delta_{1,\text{K}} & \delta_{1,\text{DS}} & \delta_{1,\text{ASD}} & \cdots & \delta_{1,\text{ESA}} \\ \vdots & \vdots & \vdots & \vdots & \ddots & \vdots \\ \delta_{i,\text{SF}} & \delta_{i,\text{K}} & \delta_{i,\text{DS}} & \delta_{i,\text{ASD}} & \cdots & \delta_{i,\text{ESA}} \end{bmatrix}, \quad (3.1)$$

where δ denotes the corresponding correlated LSP. The model considers in total seven² parameters consisting of shadow fading, K-factor, delay spread, azimuth spread of departure angles, azimuth spread of arrival angles, elevation spread of departure and elevation spread of arrival angles (*SF*, *K*, *DS*, *ASD*, *ASA*, *ESD*, *ESA*), denoted in each column of matrix \mathbf{M}_{LSP} . Rows of matrix \mathbf{M}_{LSP} represent LSPs for different links, where the link towards serving BS is denoted by index 0 and links toward interfering BSs are denoted by the indices $i = \{1, \dots, I\}$.

In regard to the system-level tool's structure, the generation of LSPs can be performed off-line, i.e., before entering the actual simulation loop. The only prerequisite is the user-to-BS assignment in order to generate only the necessary parameters and reduce the calculation overhead. Moreover, simultaneous tasks for serving- and interfering BSs can be carried out, allowing to employ, e.g., MATLAB's parallel computing toolbox. As a result, for each simulated user, a matrix of correlated LSPs is saved and this information is later applied on the following small-scale parameter (SSP) stepwise generation.

Small Scale Parameters

In the 3GPP 3D channel model, channel coefficients $H_{i,n,u,s}(t)$ are determined individually for each BS denoted with i , each cluster n and each receiver- and transmitter *antenna element* pair $\{u, s\}$, respectively. The calculation of $H_{i,n,u,s}(t)$ requires to generate delays (*Step 5*), cluster powers (*Step 6*) as well as arrival- and departure angles for both azimuth and elevation (*Step 7*). After coupling the rays within a cluster (*Step 8*), cross polarization power ratios (XPRs) and random initial phases are drawn (*Step 9 and 10*). Together with the calculation of the spherical unit vectors and the Doppler frequency component (both *Step 11*), all parameters mentioned above are commonly applied to each antenna element pair $\{u, s\}$ and thus *have to be determined only once per antenna array and BS*. The Doppler component accounts for the time variance of the channel. The frequency selectivity is determined by the channel impulse response $H_{i,n,u,s}(t)$ and the sampling frequency, which is directly related to the system bandwidth.

Coefficient Generation

After generating the channel coefficients for each antenna element pair $\{u, s\}$, the channel coefficients for an antenna array are combined according to the antenna element-to-port mapping. A detailed discussion on antenna array modeling in system-level tools will be shown later in Section 3.1.2. Then, the combined channel $\mathbf{H}_{i,n}^c(t)$, for each cluster n is sampled based on the delay taps m defined as

$$m = \left\lfloor \frac{\tau_n}{T_s} \right\rfloor, \quad (3.2)$$

²In case the user is in NLOS of BS, there are only six parameters. For this case $\delta_{0,\text{K}=0}$.

where T_s is the sample interval in the time domain and τ_n denotes the actual delay of the n -th cluster. The sampled $N_{Rx} \times N_{Tx}$ channel matrix is denoted as $\hat{\mathbf{H}}_{i,m}(t)$, with an element $[\hat{\mathbf{H}}_{i,m}(t)]_{r,p}$, referring to the sampled channel coefficient for receive antenna port r and transmit antenna port p , respectively. It is important to note that the model is designed such that the channel impulse response before sampling has unit sum power on average over t , i.e., $\mathbb{E}_t \left[\sum_n |[\mathbf{H}_{i,n}^c(t)]_{r,p}|^2 \right] = 1$, when assuming antenna elements with *omni-directional* gain pattern and 0 dB gain, as well as an XPR of one. In order not to change the sum power after the sampling, the sampled channel coefficients $[\hat{\mathbf{H}}_{i,m}(t)]_{r,p}$ are multiplied with the factor $\sqrt{\sum_n |[\mathbf{H}_{i,n}^c(t)]_{r,p}|^2 / \sum_m |[\hat{\mathbf{H}}_{i,m}(t)]_{r,p}|^2}$.

The channel transfer function is obtained by performing a Fast Fourier Transform (FFT) over the sampled and normalized channel impulse response

$$\tilde{\mathbf{H}}_i[k, t] = \sum_{m=0}^{N-1} \hat{\mathbf{H}}_{i,m}(t) e^{-j2\pi k \frac{m}{N}}, \quad (3.3)$$

where, $k = 0, 1, \dots, N - 1$. The term N represents the number of FFT samples which is the maximum number of delay taps m . For example, assuming a transmission bandwidth of 10 MHz, according to [20] for LTE standard, the sampling interval is $T_s = 65$ ns and the number of FFT samples is $N = 1024$.

3.1.2. Antenna Array Modeling

The 3GPP 3D channel model enables to scrutinize 2D planar antenna arrays, also known as rectangular arrays. The antenna elements can either be linearly polarized (*co-pol*) or cross polarized (*cross-pol*), as shown in Figure 3.4. In this regard, the model represents a compromise between practicality and precision as it does not include the mutual coupling effect as well as different propagation effects of horizontally and vertically polarized waves. Nevertheless, a well-structured implementation is important and substantially facilitates the implementation of further techniques and enhancements regarding different polarization modes such as the one proposed in [28].

The antenna elements are equidistantly spaced in the y- and the z-direction. For static electrical beam steering, also known as *electrical tilting*, a complex weight is applied to each antenna element in the vertical direction. For an antenna element in the q -th row, it is given as

$$w_q = \frac{1}{\sqrt{Q}} \exp \left(-j \frac{2\pi}{\lambda} (q-1)d_V \cos \theta_{\text{etilt}} \right), \quad (3.4)$$

where Q represents the total number of antenna elements in the vertical direction and θ_{etilt} is the steering angle in the vertical plane. Afterwards, the beamforming weights are applied to the channel coefficients for each antenna element,

$$[\mathbf{H}_{i,n}^c(t)]_{r,p} = \sum_{u \in \mathcal{P}_r} w_u \sum_{s \in \mathcal{P}_p} w_s H_{i,n,u,s}(t), \quad (3.5)$$

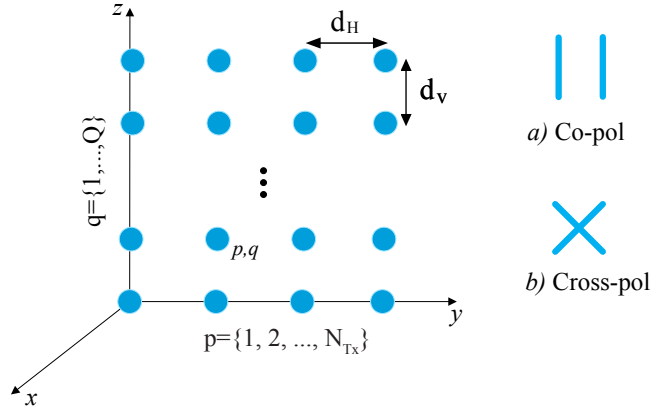


Figure 3.4.: Geometry and polarization modes of a planar antenna array. The antenna elements in horizontal and vertical direction are indexed by p and q , respectively. ©2016 EURASIP, [63].

where $[\mathbf{H}_{i,n}^c(t)]_{r,p}$ represents the weighted and combined channel coefficients. The index i indicates the i -th BS. The terms \mathcal{P}_r and \mathcal{P}_p denote the sets of antenna elements that belong to receive antenna port r with $r \in \{1, \dots, N_{Rx}\}$ and transmit antenna port p with $p \in \{1, \dots, N_{Tx}\}$, respectively, i.e., $\mathcal{P}_p = N_{Tx} \times Q$. The terms ω_u and ω_s are complex weights that account for phase shifts as applied for static beamforming (e.g., electrical downtilting), respectively.

3.2. Spatial Granularity and Complexity Reduction

The channel parameters for the GSCM can be classified as position-dependent (path loss and LSPs) and position- and time-dependent (SSPs). Considering a user with a fixed location in 3D space and a static environment, SSPs have to be calculated only in the first time instant of the simulation. Afterwards, the channel will remain static over time (no Doppler effect). If the user is moving, in principle, all channel parameters (path loss, LSPs and SSPs) have to be updated at runtime in each time instant of the simulation.

When applying the 3GPP 3D channel model, this implies the generation of new scattering clusters and random initial phases for each user (i.e., a complete change of the multipath propagation environment). Thus, it is considered reasonable from a physical perspective (see, e.g., [18] for quasi-stationary intervals), as well as in view of computational complexity to partition the scenario into equally sized cubes. As long as the user resides within the same cube, it is assumed to experience the same path loss, shadow fading, propagation conditions (LOS/NLOS/O-to-I) and LSPs. In this way, on the one hand, a cube represents the spatial granularity of the position-dependent parameters, and, on the

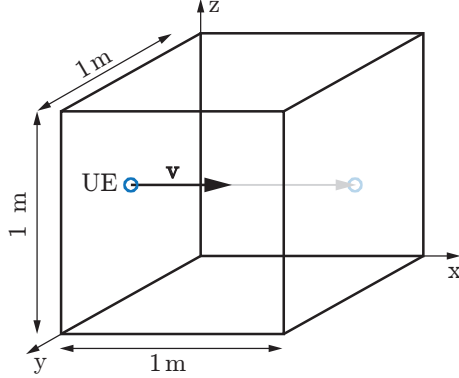


Figure 3.5.: User travels through cube with an edge length of 1 m. ©2016 EURASIP, [63].

other hand, it denotes the quasi-stationary region where the time-dependent parameters have to be calculated only once and each time the user transfers to another cube. Note that a cube does not represent the time granularity of the simulation, as within a cube still the channel varies over time due to the Doppler-shift of the signal, only the parametrization remains constant. Assuming a spatial resolution of 1 m and a temporal resolution of 1 ms, referring to the length of an LTE subframe, a user moving at $v = [27.78, 0, 0]$ m/s requires 36 ms to travel from one face of the cube to the other, as indicated in Fig. 3.5. In this case, path loss, LSPs and SSPs have to be updated every 36 sub-frames, while the small-scale fading varies over time on a subframe basis.

In order to provide continuity between cubes for the case of moving users, at the beginning of each cube, channel parameters are updated, as indicated in Fig. 3.6. Since path loss and LSPs are only position-dependant, they can be recalculated or updated according to the new user position. In the case of LSPs, the continuity is enabled due to the fact that LSPs are spatially correlated, already at *Step 4* in general parameters, as explained in Section 3.1.1. Figure 3.7 illustrates a map of correlated LSPs considering a cell size³. It is important to note that several maps consisting of spatially correlated LSPs are generated for each of the LSPs. Therefore, at the beginning of each cube, the corresponding LSP values for a user location are extracted from the correlated maps. If the user trace is known (e.g., in train and car scenarios), the simulation complexity can be reduced even further. In such scenarios, the path loss and correlated LSPs can be pre-generated off-line before the main simulation and applied in the updating phase which is performed at *run time*. Regarding the SSPs, a reduction in complexity is achieved by pre-calculating the Doppler frequency component (which is part of the SSP generation) in the first time instant of the simulation, and reuse in subsequent time instances (subframes) as long as the user stays within the same cube.

³Recall that a correlation among LSPs is established for all users served by the same BSs, referred to as cell.

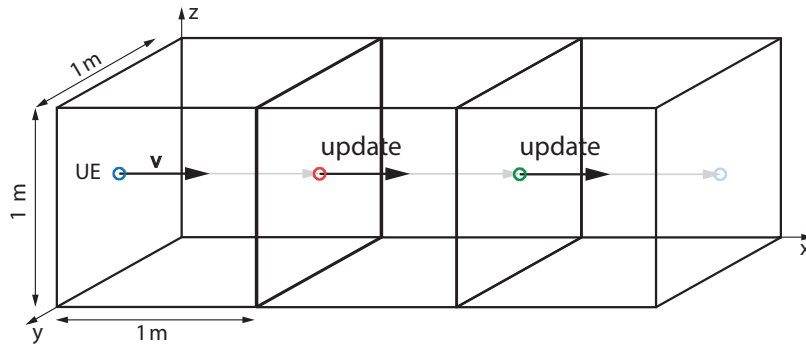


Figure 3.6.: User travels longer distances passing through several cubes. At the beginning of each channel parameters are updated.

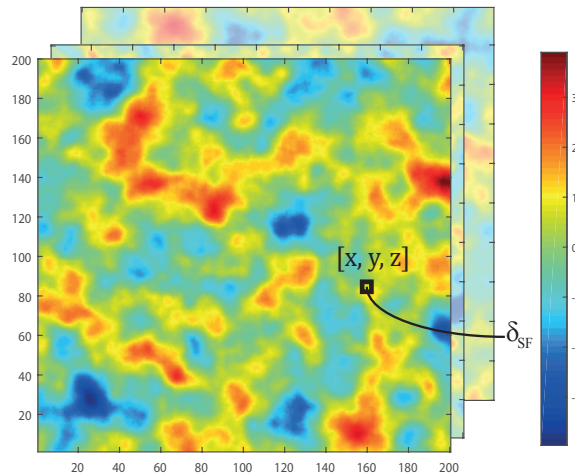


Figure 3.7.: Spatially correlated LSP maps. For each of the LSPs, a spatially correlated log normally distributed map is generated, as indicated in the figure. ©2018 EURASIP, [87].

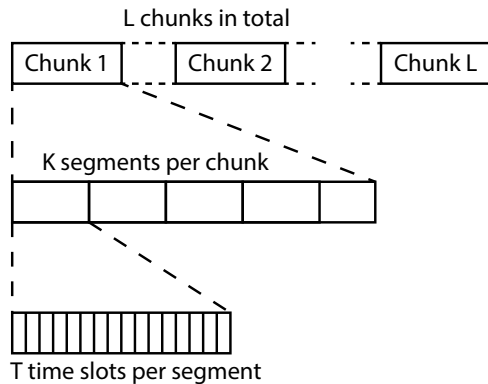


Figure 3.8.: The time line structure of the Vienna 5G System-level simulator. The simulation time in the simulator is divided into chunks, segments, and time slots. ©2018 EURASIP, [87].

3.2.1. Time line Structure for 5G and Beyond Simulation Tools

Commonly the time line structure of system-level tools is resolved on a subframe level, referred to as TTI in the LTE standard, with a duration of 1 ms. As shown in Section 2.2, to measure the quality of the received signal, denoted as link quality model, on system-level tools, the block fading assumption is utilized. This means that the channel is assumed constant over the duration of one 1 ms subframe, and denotes the first step towards complexity reduction of system-level tools [37].

However, with the introduction of GSCM on system-level tools, new challenges arise. On the one hand, due to the high number of parameters that need to be generated in GSCM, simulation efforts become enormous, and on the other hand, the spatio-temporal structure of this type of channel model does not fit in the common time line structure of system-level tools. Therefore, based on the description above following the *cube concept*, a new time line structure for system-level tools is proposed. It consists of three time partitions: *time slots*, *segments* and *chunks*, as illustrated in Fig. 3.8.

A *time slot* is the shortest time unit on which the channel coefficients are generated. It can be an 1 ms subframe compatible for LTE or a shortened version of TTI known as short TTI (sTTI)⁴ that is proposed in Release 15 of 3GPP for 5G New Radio. A *segment* represents the cube, denoting thus the time span during which the values of path loss and LSPs are assumed to be constant, whereas SSPs change only due to the Doppler-shift. One segment consists of several time slots and its length is determined based on the network characteristics such as user speed, trajectories and decorrelation

⁴According to the 3GPP, in the design of 5G New Radio, a scalable TTI scheme is expected similar to the frequency domain, considering a shorter TTI of about 1/8 ms. This flexibility allows the air interface to optimize for lower latencies considering shorter TTI or trading off for higher spectral efficiency for delay-tolerant use cases with a longer TTI.

distances. In this way, path loss, LSPs and SSPs are only updated once per segment, at the beginning of each segment. For a static network conditions, i.e., stationary users, the time line consists of one segment only. A *chunk* represents a sequence of segments. As indicated in Fig. 3.8, a considerable amount of time, that is not simulated, passes between segments, such that the position of mobile users changes significantly between chunks. Irrespective of mobility, it is assumed that the scattering environment changes significantly between chunks, and thus, channel coefficients are uncorrelated. This time line structure has been recently resolved in the Vienna 5G System-Level Simulator [87, 105].

Nonetheless, when applying the GSCM models on system-level tools, and the 3GPP 3D model as a special case, an important issue arises that is the lack of *spatial consistency*⁵. As aforementioned, the LSPs already incorporate spatial-dependency over positions and path loss follows a deterministic model being dependent on the geometry only. However, as soon as other random parameters are updated, i.e., from one segment to the other, the channel behavior will change completely. This spatial inconsistency is captured in:

- *Propagation conditions of LOS/NLOS and Indoor/Outdoor*: for two closely located users, propagation conditions are uncorrelated since they are determined from independent trials for each user location by a distance-dependent Bernoulli distribution.
- *The SSPs*: the location of scatterers is random and therefore it yields to an uncorrelated behavior between neighboring locations. In other words, two users at almost the same location do not share any scatterers.

The time duration of the updating procedure is not relevant in this case, as the model delivers completely uncorrelated behaviour of propagation condition or small-scale fading each time these parameters are generated or re-calculated. In other words, two users at almost the same location do not share similar propagation characteristics. The same is true also for static users, where there is no correlation between their respective locations. This is very important for system-level investigations, in particular for the investigation of beamforming, user grouping, interference mitigation techniques.

This chapter does not address the spatial consistency problem. Modeling of spatial consistency is treated in particular in Chapter 4 and Chapter 5, considering the proposed time line structure. In the remainder of this chapter, performance evaluation of scenarios not influenced by spatial inconsistency is presented.

⁵The term *spatial consistency* denotes the channel property of propagation characteristics reflecting distance-dependency, i.e., one would expect a high correlation between two neighboring locations and a low correlation between locations separated by a larger distance.

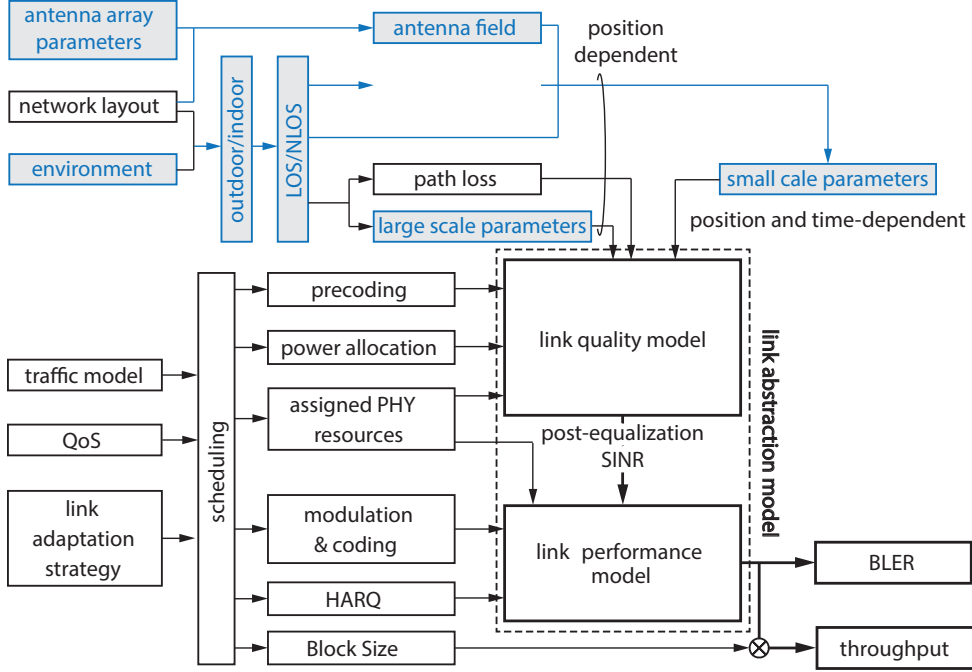


Figure 3.9.: Enhanced link abstraction model for enabling 3D channel modeling. ©2016 EURASIP, [63].

3.3. System-level Performance Evaluation

In this section, the application of the proposed procedure in an existing system-level simulation tool is demonstrated. The 3GPP 3D channel model is integrated into the Vienna LTE-Advanced (LTE-A) Downlink System-Level Simulator (starting from v1.8r1375) [61]. A full calibration of the 3GPP 3D channel model implementation is provided in Appendix B. Also, calibration for the implementation of the extended version of the 3GPP 3D channel model, specified with 3GPP TR 38901 [72], including a larger frequency range up to 100 GHz is available in the latest release of Vienna LTE-A Downlink System-Level Simulator (current version v2.0 Q3-2018) [105]. Additionally, the probability distribution functions of angular statistics are provided in Appendix C.

The simulator is implemented in object-oriented MATLAB and is made openly available for download under an academic, non-commercial use license. Counting more than 30.000 downloads, the Vienna LTE-A Downlink System-Level Simulator has become a reliable tool for companies and well as academia worldwide. It is built according to the commonly employed structure for system-level simulation tools (see, e.g., in [33, 52]), as illustrated in Fig. 3.9 and, thus, serves as a representative example. This structure is prevailed also in simulation tools for 5G, as presented in [87, 102, 52]. The enhancements that were necessary to enable the 3GPP 3D channel model for desired and interfering signals, are depicted by the boxes shaded in gray, as illustrated in Fig. 3.9.

3.3.1. Simulation Run Times

In this section, the simulation run time of the 3GPP 3D channel model is investigated considering the Vienna LTEA Downlink System-Level Simulator. The goal is to observe how the 3GPP 3D channel model affects the simulation run time. For a fair comparison, all simulations are carried out on the same hardware, an Intel(R) Core(TM) i7-3930K CPU@3.20 GHz, equipped with 32 GB of DDR3 1333 quad-channel RAM.

The network comprises seven hexagonally arranged macro-sites, each employing three BS sectors spaced out at 120° , as shown in Fig. 3.10. Hence, a user will experience a maximum of $N_{\text{sector}} = 20$ interfering BS sectors. Simulations are carried out with the antenna port configuration $N_{\text{Tx}} \times N_{\text{Rx}} = 4 \times 2$ and $\mathcal{P}_p = \{8, 24, 40, 80\}$ antenna elements at the antenna array in the transmitter, yielding $Q = \{2, 6, 10, 20\}$ antenna elements per port (see Fig. 3.14). Simulation lengths $N_{\text{TTI}} = \{10, 50, 100\}$, where N_{TTI} denotes the number of simulated 1 ms subframes are considered, and $K = \{2, 20, 50\}$ users per BS sector. The results are averaged over five simulation runs per individual configuration. The simulation parameters are summarized in Table 3.1. Figure 3.11 provides the results in terms of simulation run time measured in [s]. In Fig. 3.11a it is observed that the results scale approximately linearly with the number K of users and with the simulation length N_{TTI} . Such behavior was already observed in [61] together with a more detailed description by also comparing it with link-level where only a single link is evaluated. The particular focus of this section is the impact of the elevation dimension and the application of the 3GPP 3D channel model for both desired and interfering channels on the simulation run time. From the results it is further observed that the simulation run time increases with a higher number \mathcal{P}_p of antenna elements. In order to make that trend more clear, the simulation run time over \mathcal{P}_p for various numbers K of users is depicted. It is noted that the run times grow approximately linearly with the number of antenna elements per antenna array. This confirms the expected result that the price to pay for modeling more than one antenna element per antenna port is nearly a linear increase in complexity for each additional antenna element per antenna port.

By modeling both the desired as well as the interfering channels by the 3GPP 3D channel model, in the next step, it is investigated how simulation run time scales by successively increasing N_{sector} , starting with two interfering BS sectors. The selection of interfering sectors is carried out randomly. For example, $N_{\text{sector}} = 2$ means that two out of the 20 interfering BS sectors were taken into account but might not necessarily be the two strongest ones. The strength of the interferers is of no relevance for this evaluation as the interest is mainly in simulation run times, i.e., the complexity of generating the interfering channels by means of the 3GPP 3D channel model. Considering $K = \{2, 20, 50\}$ users per cell at a simulation length of 20 TTI, $\mathcal{P}_p = \{8, 24, 40\}$ antenna elements per antenna array and varying the number of interfering BS sectors, simulation run times are measured. The simulation results are provided in Fig. 3.11b. It is found that the run time scales linearly with the number of interfering BS sectors. On the other hand, for a large number of interfering BS sectors, there is

Table 3.1.: Common simulation parameters.

Parameter	Value
Carrier frequency	2 GHz
LTE bandwidth	10 MHz
Macro-site deployment	hexagonal grid, one tier
Interfering BS sectors	$N_{\text{sector}} = \{2, 8, 14, 20\}$
Number of users per cell	$K = \{2, 20, 50\}$
Antenna elements per antenna array	$\mathcal{P}_p = \{8, 24, 40, 80\}$
Antenna elements per antenna port	$Q = \{2, 6, 10, 20\}$
3GPP scenario	3D-UMa
Inter-site distance	500 m
BS transmit power	46 dBm
Antenna element gain pattern	3D pattern [43, Tab. 7.1-1]
Antenna polarization	co-pol
Polarized antenna modeling	model 2 [43, Sec. 7.1.1]
Maximum antenna element gain	8 dBi
Vertical antenna element spacing	$\lambda/2$
Horizontal antenna element spacing	$\lambda/2$
User distribution	uniform
User speed	3 km/h
User antenna gain pattern	omni-directional
User antenna array polarization	co-pol
Wrapping method	center users evaluated
Receiver type	zero forcing
Channel knowledge	perfect
Feedback delay	3 TTI
Noise power density	-174 dBm/Hz
LTE transmission mode	4
Scheduler	proportional fair
Traffic model	full buffer
Simulation length	$N_{\text{TTI}} = \{10, 50, 100\}$

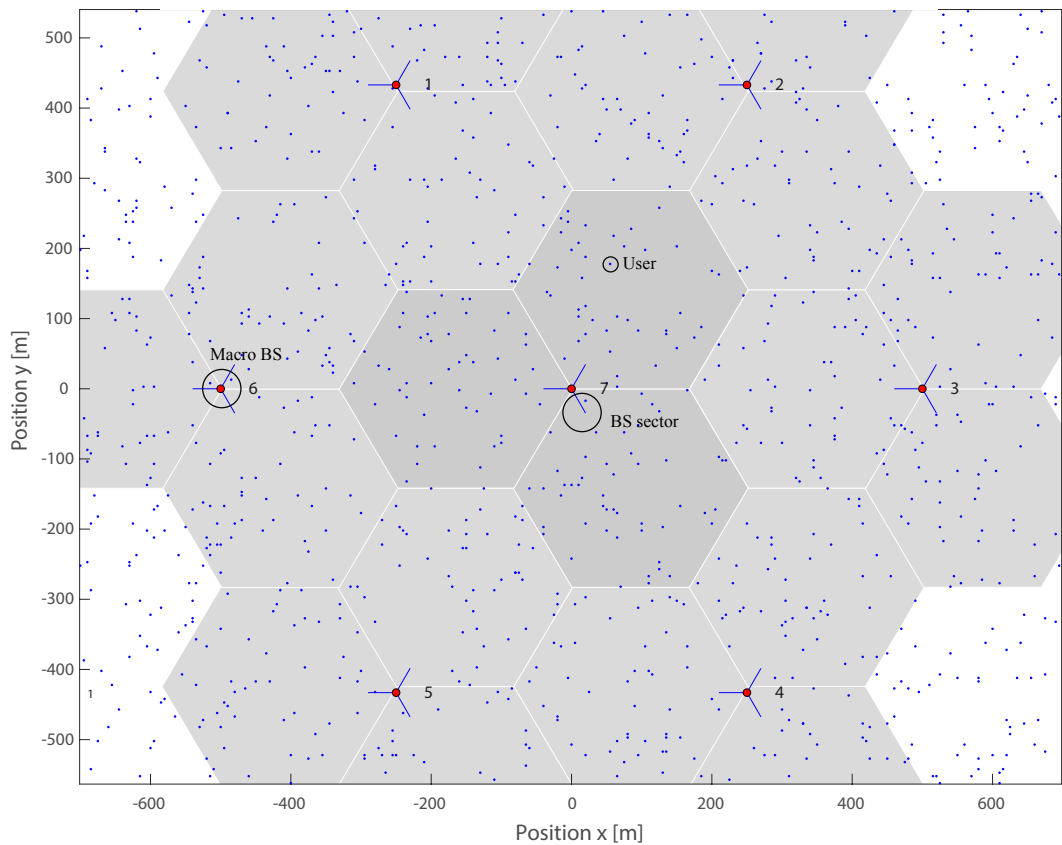


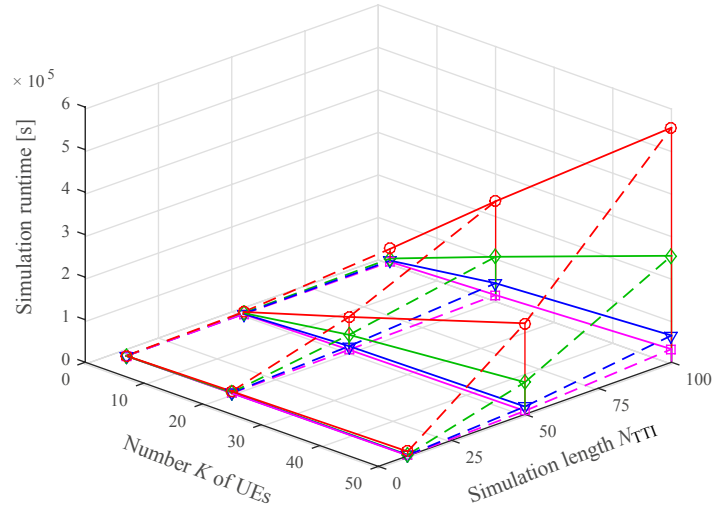
Figure 3.10.: Urban scenario consisting of three-sectorized macro BS and uniformly distributed users with K per cell. Users share various propagation conditions, being in LOS or NLOS, indoors or outdoors.

a non-linearity with the number of users. This results from the fact that the contribution of those interferences that have a received power below a certain threshold (e.g. the noise power) is neglected. Hence, the users will in general experience a different amount of interfering BS sectors. Furthermore, investigation on the simulation run times over the number \mathcal{P}_p of antenna elements assuming two simulation lengths $N_{\text{TTI}} = \{50, 100\}$ and including all the interfering BS sectors is performed. The simulation results are provided in Fig. 3.12. Again, the results exhibit an approximately linear growth in the simulation run time over \mathcal{P}_p antenna elements for various number K of users and various simulation lengths. Hence, in scenarios with large antenna arrays, the simulation run time will scale roughly proportional with the number of antenna elements.

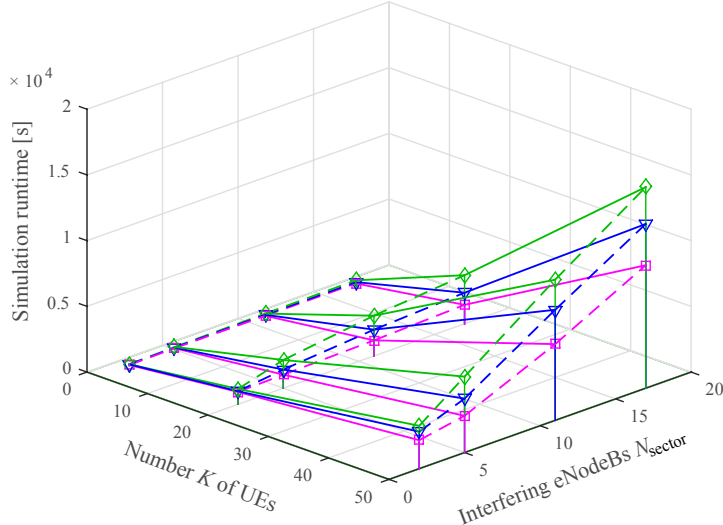
In the next step, two types of GSCM are compared, the 3GPP 3D model and the Wireless World Initiative New Radio (WINNER) model. The implementation of the WINNER channel model taken from [17] was already integrated in the Vienna LTE-A Downlink System-Level Simulator [37]. In both models, the generation of the channel coefficients follows a similar procedure. The main difference is that the WINNER model implemented in the Vienna LTE-A Downlink System-Level Simulator is a 2D model, i.e., it does not incorporate the elevation dimension. Consequently, it only allows to apply linear antenna arrays where $Q = 1$. In contrast, the 3GPP 3D model enables to scrutinize 2D antenna arrays. Simulations with an antenna port configuration of $N_{\text{Tx}} \times N_{\text{Rx}} = 4 \times 2$ are carried out. In order to unveil the impact of including the elevation information onto the simulation run time, I consider $Q = \{1, 2, 10\}$ antenna elements in vertical dimension, while for the WINNER model, $Q = 1$ restriction applies. Various simulation lengths $N_{\text{TTI}} = \{10, 50, 100\}$ are evaluated with $K = \{2, 20, 50\}$ users per BS sector. The results in terms of simulation run times are provided in Fig. 3.13. When comparing the simulation run times of the 3GPP 3D channel model and the WINNER model using a linear antenna array, it is observed that for $K = 50$ users and $N_{\text{TTI}} = 100$, the run time increases by a factor of 3.1. Thus, by taking into account the elevation dimension, the simulation run time more than triples. For planar antenna arrays with $Q = 10$, the run time is increased by a factor of 27.49, when comparing with the WINNER model. Hence, the complexity grows roughly proportional with the number of antenna elements, which becomes a prominent factor for simulations of scenarios with large antenna arrays (i.e., full dimension (FD)- MIMO, massive MIMO).

3.3.2. Throughput Performance Evaluation

Previously it has been shown that there is a significant increase in simulation complexity when considering a higher number of interfering links. In this section, in particular modeling of the interfering channels is investigated. The goal is to compare the performance in terms of average user throughput when modeling each of the interfering channels with the 3GPP 3D channel model and when using a simplified channel models such as Rayleigh fading.



(a) Fixed number of interfering BS sectors (one tier).



(b) Varying number of interfering BS sectors for $N_{\text{TTI}} = 20$.

Figure 3.11.: Simulation run times for various antenna array geometries, simulation lengths N_{TTI} , number K of users and number N_{sector} of interfering BS sectors. ©2016 EURASIP, [63].

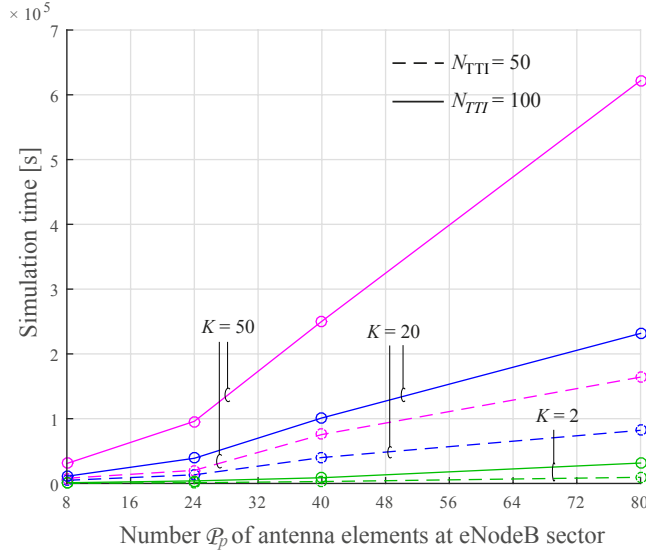


Figure 3.12.: Simulation run time [s] over number of antenna elements P_p . Dashed lines denote a simulation length of $N_{TTI} = 50$ TTI, solid lines refer to a simulation length of $N_{TTI} = 100$ TTI. ©2016 EURASIP, [63].

WINNER	3D model, Q=1	3D model, Q=2	3D model, Q=10
--------	---------------	---------------	----------------

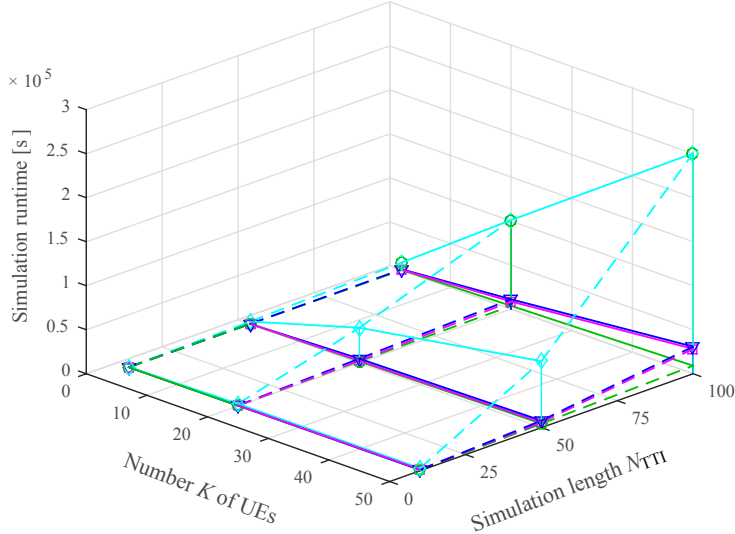


Figure 3.13.: Simulation run times [s] of two channel models: 3GPP 3D model and WINNER model for various simulation lengths N_{TTI} and number K of users. For observing the elevation information added in the 3GPP 3D model, a linear array with $Q = 1$ and a planar array with $Q = 2$ and $Q = 10$ are considered, while the WINNER model employs a linear array. ©2016 EURASIP, [63].

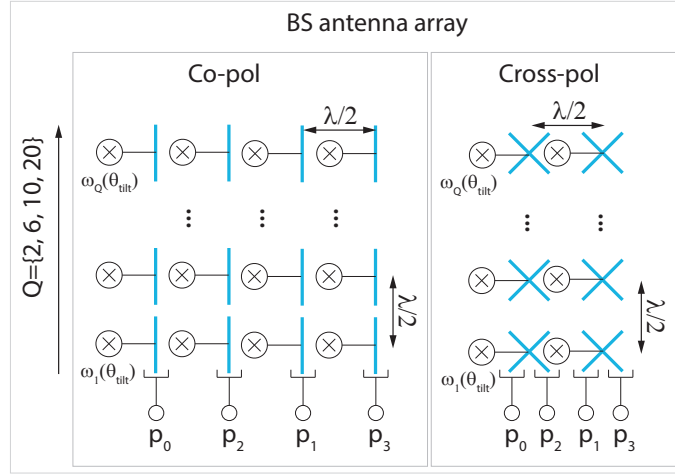


Figure 3.14.: Antenna array port virtualization applied on system-level for *co-pol* and *cross-pol* polarization modes. The antenna ports are denoted as p_i with $i \in \{1, \dots, 4\}$. The parameters $\omega_q, q \in \{1, \dots, Q\}$ are the phase shifts for static beamforming (e.g., electrical downtilting). ©2016 EURASIP, [63].

Similar as before, a network with seven macro-BSSs is considered, each employing three sectors and a total of 50 randomly distributed users per BS sector. The simulation parameters are summarized in Table 3.1.

Rayleigh versus 3GPP 3D Model

A performance comparison in terms of average user throughput is carried out considering:

- (i) a noise-limited network as a baseline,
- (ii) interference channels modeled by Rayleigh fading,
- (iii) interference channels modeled by the 3GPP 3D channel model.

The desired channel in all cases is modeled with the 3GPP 3D channel model. Four antenna ports are considered at the transmitter, i.e., $N_{\text{Tx}} = 4$ and a planar antenna array with $Q = 10$ linearly polarized antenna elements per antenna port. The antenna elements Q of an individual port are stacked in vertical direction with a spacing of 0.5λ , as indicated in Fig. 3.14. This configuration is known as *sub-array partition model* since the same weight vector ω_q is applied for each port [53, Sec. 5.2.2]. The users are equipped with a linear antenna array consisting of two antenna elements, each being associated to an individual antenna port.

Figure 3.15 depicts the results in terms of average user throughput statistics. It is observed that modeling interference channels by the 3GPP 3D model provides a more optimistic view on the

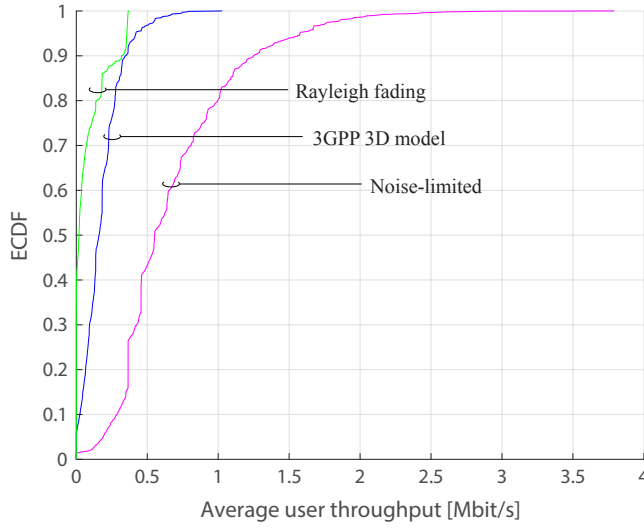


Figure 3.15.: Average user throughput [Mbit/s] empirical cumulative distribution function (ECDF) curves considering three different channel models for interfering links. ©2016 EURASIP, [63].

performance compared to Rayleigh fading case. The noise-limited scenario serves as a best-case reference. The difference between modeling interfering channels by the 3GPP 3D model and Rayleigh fading stems from the fact that in the 3GPP 3D model, the SSPs incorporate the antenna element field patterns while in the Rayleigh fading case, they only affect the path loss. Consequently, the small-scale fading in the 3GPP 3D channel model case has a stronger tendency to result in quasi-orthogonal signal spaces of desired and interfering signals. In the next section, further investigations on the impact of antenna array size and focusing of the beam in specific locations is investigated. The results from Fig. 3.15 indicate that simple channel models may underestimate the throughput performance, therefore it is important that channel models applied for system-level performance evaluations capture the main characteristics of signal propagation.

3.4. Spatial Resolution of Antenna Arrays

In this section, a systematic procedure to evaluate the spatial resolution of 2D antenna arrays in a 3GPP consistent scenario under realistic channel conditions is introduced. The real promise of large antenna arrays is to increase the spatial resolution of beams toward specific directions/user locations in both elevation and azimuth.

On the other hand, existing work on directional beamforming mostly assumes simplistic signal propagation characteristics under LOS conditions, where only log-distance dependent path loss is taken into account, while the impact of the channel is omitted [59, 60].

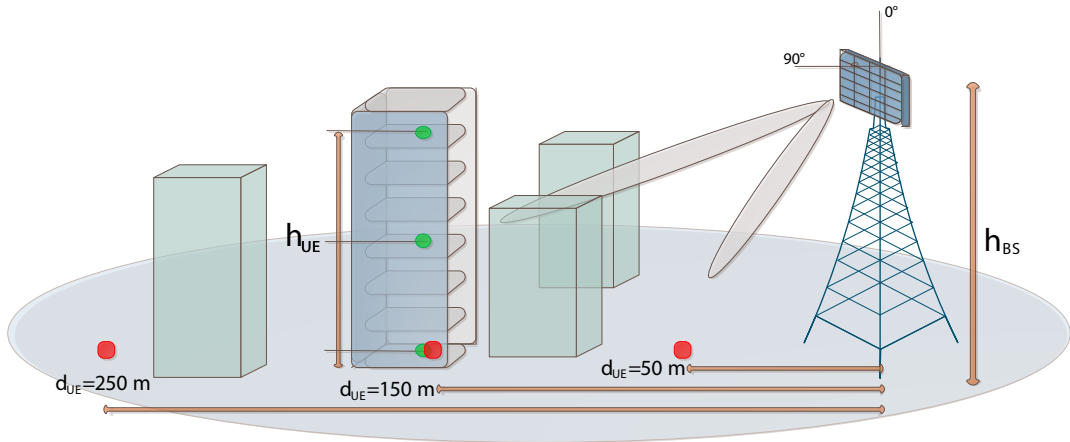


Figure 3.16.: System model comprising a single BS equipped with a 2D antenna array. Indoor users are denoted by green circles, outdoor users are indicated by red squares. ©2016 IEEE, [64].

In order to explicitly identify the impact of the 3GPP 3D channel on the spatial resolution of a planar antenna array, a single-BS-single-user scenario is considered. Such scenario is advantageous because it excludes any plausible side effects produced by the lack of spatial consistency. Furthermore, a simplification of the already complex structure of a system-level simulator into a single link is beneficial for explicitly analysing the impact of channel model on directional beamforming.

3.4.1. System Model

The system model comprises a single BS and a single user, as illustrated in 3.16. Various user locations, such as indoors and outdoors, are considered under both LOS and NLOS propagation conditions⁶. A typical indoor user is considered to be at a fixed distance from the BS d_{UE} , and its height h_{UE} is varied, representing users on different floors of a building (green circles in Fig. 3.16). For the outdoor user, the height is fixed, whereas the distance to the BS is varied, representing outdoor users (red squares in Fig. 3.16). The user is equipped with linearly-polarized antenna elements with an omni-directional gain pattern, where a single antenna element is associated to a single antenna port r , as illustrated in Fig. 3.17.

The BS is equipped with a 2D antenna array that is mounted at a height h_{BS} and comprises of equidistantly spaced antenna elements in the vertical dimension, as depicted in Fig. 3.17. The horizontal dimension represents the number N_{Tx} of antenna ports. The vertical dimension represents the number Q of antenna elements mapped to one antenna port. In order to form and steer beams in the analog domain, complex weights ω_q , where q denotes the q -th antenna element in the vertical

⁶An indoor user in LOS represents the case when the building where the user is located is in LOS.

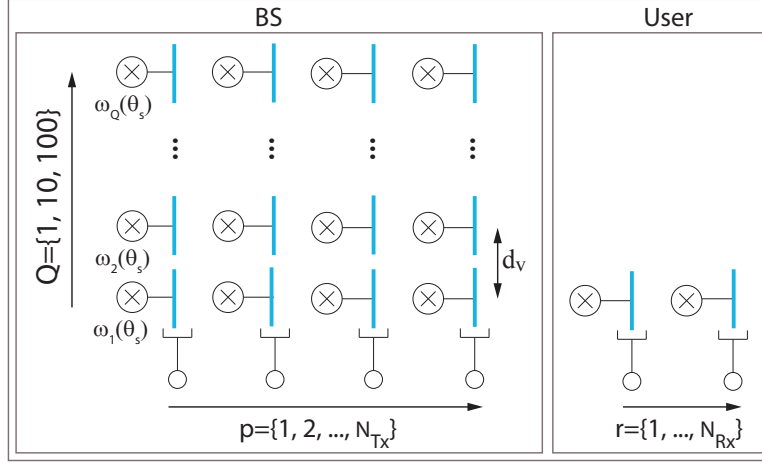


Figure 3.17.: Antenna array structure at BS consisting of N_{Tx} antenna ports and Q antenna elements in elevation associated to a single antenna port. At the user side, a single antenna element is associated to a single port r . ©2016 IEEE, [64].

direction, are applied to the antenna elements, as indicated in Figure 3.17. Following main radiation direction θ_s in elevation, complex weights are defined as

$$w_q = \frac{1}{\sqrt{Q}} \exp \left(-j \frac{2\pi}{\lambda} (q-1)d_V \cos \theta_s \right), \quad (3.6)$$

where d_V is the distance between two antenna elements in vertical direction and λ denotes the wavelength. The angle θ_s is considered to be 90° in the direction of the array's boresight, and has a range of 0° to 180° , as indicated in Fig. 3.16.

The channel⁷ description from Section 2.4 is employed, where channel coefficients are generated for each *transmitter-receiver* antenna port. They are generated for each cluster n and ray l within the cluster, representing the multipath propagation. For a static user, considering NLOS propagation transmission, the channel coefficients for transmit antenna port p and receive antenna port r are given as

$$h_{n,r,p} = \sqrt{\frac{P_n}{L}} \sum_{l=1}^L \begin{bmatrix} F_{r,\theta}(\theta_{n,l,EOA}, \phi_{n,l,AOA}) \\ F_{r,\phi}(\theta_{n,l,EOA}, \phi_{n,l,AOA}) \end{bmatrix}^T \begin{bmatrix} e^{(j\Psi_{n,l}^{\theta\theta})} & \sqrt{K_{n,l}^{-1}} e^{(j\Psi_{n,l}^{\theta\phi})} \\ \sqrt{K_{n,l}^{-1}} e^{(j\Psi_{n,l}^{\phi\theta})} & e^{(j\Psi_{n,l}^{\phi\phi})} \end{bmatrix} \begin{bmatrix} F_{p,\theta}(\theta_{n,l,EOD}, \phi_{n,l,AOD}) \\ F_{p,\phi}(\theta_{n,l,EOD}, \phi_{n,l,AOD}) \end{bmatrix}, \quad (3.7)$$

⁷Note that in the system model depicted in Fig. 3.16, buildings are placed only to illustrate different propagation conditions, however in the applied channel model no buildings are considered. The effects of having buildings, or other obstructions is modeled stochastically by means of various parametrized distributions.

where $F_{r,\theta}$ and $F_{r,\phi}$ are the field patterns at receive antenna port r , $\theta_{n,l,EOD/EOA}$ denoting the elevation direction and $\phi_{n,l,AOD/AOA}$ refers to the azimuth direction. The expressions $F_{p,\theta}$ and $F_{p,\phi}$ are the corresponding field patterns of transmit antenna port p . The term $K_{n,l}$ represents cross polarization power ratios for each cluster n and ray l , and $\Psi_{n,l}$ are random initial phases for four different polarization combinations. In the LOS case, the channel coefficients encompass a superposition of the channel impulse response of the LOS component, $h_{0,r,p}$ and multipath components $h_{n,l,r,p}$

$$h_{n,r,p}^{\text{LOS}} = \sqrt{\frac{K_R}{K_R + 1}} h_{0,r,p} + \sqrt{\frac{1}{K_R + 1}} h_{n,l,r,p}, \quad (3.8)$$

where

$$h_{0,r,p} = \begin{bmatrix} F_{r,\theta}(\theta_{0,EOA}, \phi_{0,AOA}) \\ F_{r,\phi}(\theta_{0,EOA}, \phi_{0,AOA}) \end{bmatrix}^T \begin{bmatrix} e^{j\Psi_0} & 0 \\ 0 & -e^{j\Psi_0} \end{bmatrix} \begin{bmatrix} F_{p,\theta}(\theta_{0,EOD}, \phi_{0,AOD}) \\ F_{p,\phi}(\theta_{0,EOD}, \phi_{0,AOD}) \end{bmatrix}, \quad (3.9)$$

represents the LOS component and is determined based on the geometry, i.e., angle of arrival and departure are deterministic, there is no randomness. The term K_R in Eq. (3.9) denotes the Rician K-factor.

The antenna field pattern at port p comprises the beam weights applied to each antenna element. Considering Q antenna elements connected to port, p , the antenna field pattern is given as

$$\begin{aligned} F_{p,\theta}(\theta, \phi) &= \sum_{q=1}^Q w_q \exp\left(j2\pi\lambda_0^{-1}\left(\hat{r}_q^T \bar{d}_q\right)\right) G_{q,\theta}(\theta, \phi), \\ F_{p,\phi}(\theta, \phi) &= \sum_{q=1}^Q w_q \exp\left(j2\pi\lambda_0^{-1}\left(\hat{r}_q^T \bar{d}_q\right)\right) G_{q,\phi}(\theta, \phi), \end{aligned} \quad (3.10)$$

where $G_{q,\theta}$ and $G_{q,\phi}$ denote the *antenna element field patterns* in elevation and azimuth, and the remaining part of the sum term represents the array factor (AF). According to the 3GPP 3D channel model specification, the antenna element field pattern in elevation is

$$G(\theta) = -\min \left\{ 12 \left(\frac{\theta - 90^\circ}{\theta_{3\text{dB}}} \right)^2, A_V \right\} \quad (3.11)$$

with 3 dB beamwidth $\theta_{3\text{dB}} = 65^\circ$ and front-to-back ratio $A_V = 30$ dB. In azimuth domain, the antenna element field pattern is modeled as

$$G(\phi) = -\min \left\{ 12 \left(\frac{\phi}{\phi_{3\text{dB}}} \right)^2, A_H \right\} \quad (3.12)$$

with 3 dB beamwidth $\phi_{3\text{dB}} = 65^\circ$ and front-to-back ratio $A_H = 30$ dB.

Figure 3.18 depicts antenna field patterns for $Q = \{1, 10, 100\}$ antenna elements in the vertical direction. The main radiation direction of these patterns can be controlled by the steering angle θ_s in Eq. (3.6).

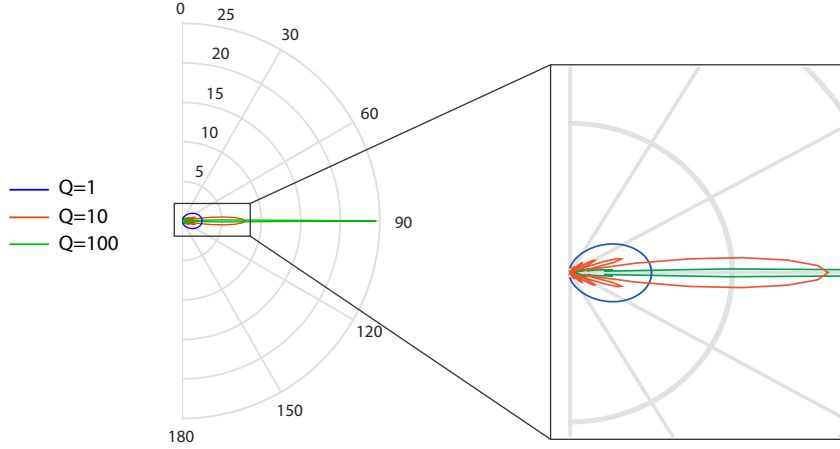


Figure 3.18.: Antenna array radiation pattern in elevation dimension, consisting of a single port p with $Q = \{1, 10, 100\}$ elements in vertical direction. ©2016 IEEE, [64].

3.4.2. Simulations

In this section, system-level simulations are employed to evaluate the introduced setup. The Vienna LTE-A Downlink System-Level Simulator [61] is considered. Two parameters are considered as performance measure: the received channel energy and the average user throughput.

The received channel energy measures the received energy of the channel in analog domain. It is determined by means of the squared Frobenius norm and formulates as

$$||\mathbf{H}||_F^2 = \sum_{p=1}^{N_{Tx}} \sum_{r=1}^{N_{Rx}} |h_{r,p}|^2, \quad (3.13)$$

where N_{Tx} refers to the number of transmit antenna ports, N_{Rx} is the number of receive antenna ports and $h_{r,p}$ denotes the channel coefficient of transmit antenna port p and receive antenna port r , after performing a FFT over the channel impulse response (channel transfer function) as inferred from Eq. (3.3). Note that time and frequency indices of the channel transfer function are omitted here, since the channel is observed for the duration of one TTI and averaged in the frequency domain over RBs.

The average user throughput, on the other hand, is evaluated in the digital domain, i.e., after applying the precoder in a LTE system, and extracted from system-level simulations. Hence, in the analog domain, the spatial resolution of sharp beams considering the impact of elevation dimension can be measured, whereas in the digital domain the output is generated per antenna port⁸.

⁸Note that Q antenna elements in vertical direction are mapped to a single antenna port (see Fig. 3.17). The maximum number of ports considering the LTE standard is restricted to $N_{Tx} = 8$.

Table 3.2.: Specific simulation parameters for single BS- single user scenario.

Parameter	Value
Carrier frequency	2 GHz
LTE bandwidth	10 MHz
BS transmit power	46 dBm
Antenna element gain pattern	3D pattern [43, Tab. 7.1-1]
Polarized antenna modeling	model 2 [43, Sec. 7.1.1]
BS antenna polarization	linear
Maximum antenna element gain	8 dBi
Vertical antenna element spacing	$\lambda/2$
Horizontal antenna element spacing	$\lambda/2$
User antenna gain pattern	omni-directional
User antenna array polarization	linear
User speed	5km/h
Receiver type	zero forcing
Channel knowledge	perfect
Feedback delay	3 TTI
Noise power density	-174 dBm/Hz
LTE transmission mode	4
Scheduler	proportional fair
Traffic model	full buffer

The channel parameters from a 3GPP 3D-UMa scenario are employed as specified in [43, Table 7.3-6] and use an $N_{Rx} \times N_{Tx} = 4 \times 2$ antenna port configuration, which is also utilized as a reference setting for calibrations [43, Table 8.2-2]. The BS is equipped with a 2D antenna array mounted at a height $h_{BS} = 25$ m. Three different cases with $Q = \{1, 10, 100\}$ antenna elements per antenna port are considered. The radiation pattern of a single antenna element is given by a combination of a vertical and a horizontal antenna element pattern, as specified in [43, Tab.7.1-1.].

At the user, a linear array consisting of two horizontal elements is considered. The target building of the indoor user is assumed to be located at a distance $d_{UE} = 150$ m away from the BS. This distance refers to the center of a typical macro-cell [43]. Three user heights are considered, $h_{UE} = \{1.5, 10.5, 22.5\}$ m, representing an indoor user in the ground floor, middle and top floor of the building, respectively. The outdoor user is considered at distances $d_{UE} = \{50, 150, 250\}$ m away from the BS, referring to three regions in the cell, near zone, cell center and cell-edge, respectively. The simulation parameters are summarized in Table 3.2.

Figure 3.19 provides simulation results in terms of received channel energy and average user throughput measured in [Mbit/s], as evaluated for the typical indoor user. The received channel energy is normalized to 1 Joule on a dB scale. Figure 3.19a shows the received channel energy for $Q = \{1, 10, 100\}$ antenna elements in elevation, while the user height is fixed at $h_{UE} = 1.5$ m, i.e., the lower floor of the building. It is observed that the antenna array geometry in elevation impacts

3.4. Spatial Resolution of Antenna Arrays

LOS and NLOS cases in a distinct manner. For the steering angle $\theta_s = 100^\circ$, which represents the case where the main radiation beam is directed toward the user location, increasing the number Q of antenna elements in elevation monotonically increases the channel energy only when the user is in LOS. Increasing Q from 1 to 10 results in 10 dB enhancement, while for $Q = 100$ results in only further 4 dB enhancement compared to $Q = 10$. Hence, a 10fold increase in Q does not result in a 10fold increase in $\|\mathbf{H}\|_F^2$. The reason for not achieving the expected 10fold enhancement in channel energy when increasing the number of antennas from 10 to 100 is the interaction with the scattering environment; specifically, the highly focused transmit beam produced by the antenna array is spread out by the transmission medium. For the NLOS case, the highest channel energy received results to be equal for both $Q = 10$ and $Q = 100$ when θ_s aims towards the user location. The spatial resolution between two neighbor steering angles, $\theta_s = 100^\circ$ and $\theta_s = 110^\circ$, results in 10 dB decrease for $Q = 10$ and 15 dB decrease for $Q = 100$ in NLOS case. The spatial resolution in LOS is higher compared to NLOS, indicating up to 23 dB decrease achieved for $Q = 100$.

Figure 3.19b provides the performance results in terms of average user throughput for the same system configuration. A setup with both $Q = 10$ and $Q = 100$ in LOS achieves the highest throughput, when the steering angle aims at the user location. With $Q = 100$, the performance is consistently lower than with $Q = 10$ for the neighboring steering angle values other than the steering angle aiming at the user location, reflecting the better spatial resolution achieved with a higher number of antenna elements. This improvement in spatial resolution can be translated to a corresponding enhancement of the cell capacity, by serving multiple spatially separated users in parallel over weakly interfering beams. Observing the NLOS case and a steering angle of $\theta_s = 100^\circ$, the setup with $Q = 10$ achieves the highest throughput. Remarkably, applying $Q = 100$ results in lower throughput, indicating that the spatial resolution in elevation is suppressed by the precoder in digital domain, while in terms of channel energy both $Q = 10$ and $Q = 100$ show the same behavior.

Figure 3.19c shows the received channel energy for user heights of $h_{\text{UE}} = \{1.5, 10.5, 22.5\}$ m and an antenna array with $Q = 10$ elements in elevation. Due to the different user heights, the peaks of the channel energy are obtained at different steering angles, indicating the cases when the steering angle aims at the user location, with $\theta_s = \{98.9^\circ, 95.5^\circ, 90.9^\circ\}$ corresponding to user heights $h_{\text{UE}} = \{1.5, 10.5, 22.5\}$ m. Furthermore, the results indicate the impact of the building blockage. More specifically, when the target building is in NLOS, for the outdoor-indoor connection, the energy decreases more at lower user heights. For the same configuration, the results in terms of average user throughput are provided in Fig. 3.19d. As expected, the highest throughput is achieved when target building is in LOS. However, a smaller spatial resolution is achieved compared to the NLOS propagation condition. The spatial resolution between neighbor steering angles $\theta_s = 100^\circ$ and $\theta_s = 110^\circ$ is much sharper for lower user heights, resulting in 20 dB decrease, whereas for the user located at top floor of the building, the spatial resolution is only 10 dB. This indicates that remarkably for NLOS transmissions, despite a more moderate resolution in terms of channel energy, the channel amplifies the distinction between two neighboring angles in terms of throughput.

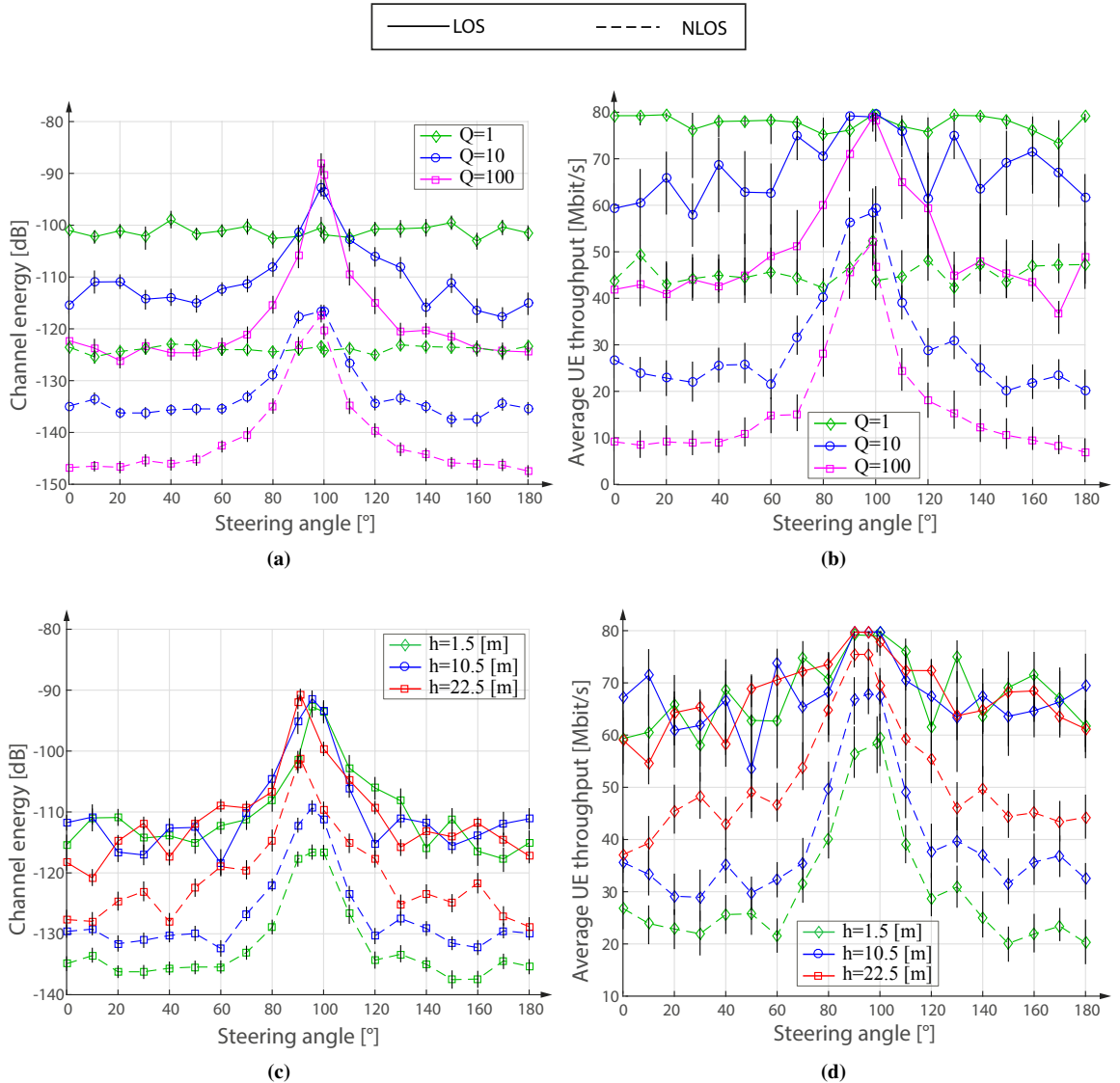


Figure 3.19.: Channel energy (a) (c) and average throughput [Mbit/s] (b) (d) of typical indoor user over steering angle. Results are shown for $Q = \{1, 10, 100\}$ antenna elements in elevation at a fixed user height of $h_{UE} = 1.5$ m and for various user heights of $h_{UE} = \{1.5, 10.5, 22.5\}$ m at $Q = 10$. Vertical black lines denote 95 % confidence intervals. ©2016 IEEE, [64].

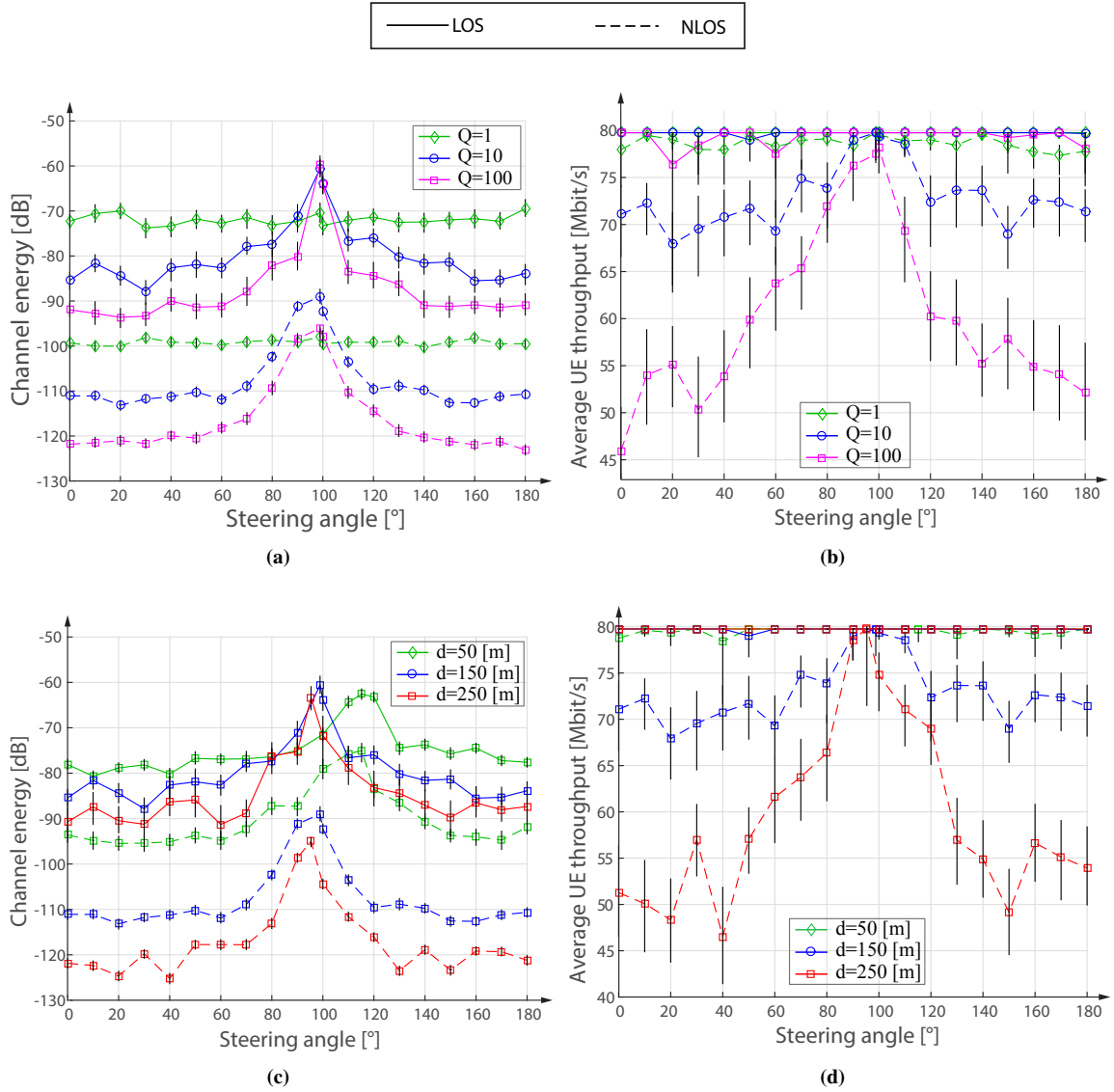


Figure 3.20.: Channel energy (a) (c) and average throughput [Mbit/s] (b) (d) of typical outdoor user over steering angle. Results are shown for $Q = \{1, 10, 100\}$ antenna elements in elevation at a fixed user distance of $d_{UE} = 150$ m and for various user distances of $d_{UE} = \{50, 150, 250\}$ m at $Q = 10$. Vertical black lines denote 95 % confidence intervals. ©2016 IEEE, [64].

Again, this improvement in spatial resolution can be translated to a corresponding enhancement of the cell capacity, where multiple spatially separated users can be served in parallel with suppressed interference.

Figure 3.20 provides the simulation results for a typical outdoor user. Figure 3.20a shows the received channel energy for $Q = \{1, 10, 100\}$ antenna elements in elevation, while the user distance from the BS is fixed at 150 m. The energy difference between LOS and NLOS conditions exhibits a similar behaviour as in the indoor case, while the absolute energy is higher. This is mainly due to the fact that the outdoor user does not experience wall penetration loss. In addition, the received channel energy experiences a larger decay from the target steering angle of 98.9° towards neighboring points. Particularly for the LOS transmission, the resolution between neighboring steering angles is larger than for the NLOS case. Figure 3.20b provides the performance results in terms of average user throughput for the same system configuration. Remarkably, in comparison to indoor users, the throughput performance under LOS conditions for various numbers Q of antenna elements is invariant with respect to the steering angle. This stems from the fact that in the digital domain, after applying the precoder, a further increase in throughput is not supported by the structure of the applied precoder. If 2D precoders would be applied, it would reflect in higher differences between the three cases. This also motivates the necessity for new precoder designs that are capable in preserving the spatial resolution achieved both in azimuth and elevation. However, this topic goes beyond the scope of this thesis and is not treated in this work. Under NLOS conditions, the throughput results indicate that the resolution between neighboring steering angles is more distinct. This is mainly due to the fact that the signal power is smaller compared to LOS and not capable of achieving the highest throughput.

Figure 3.20c shows the received channel energy of outdoor user at distances $d_{UE} = \{50, 150, 250\}$ m and a fixed antenna array geometry with $Q = 10$ antenna elements in elevation. Due to the various distances to the BS, the peak values are located at different steering angles, with $\theta_s = \{115.2^\circ, 103.2^\circ, 98.9^\circ\}$ corresponding to distances $d_{UE} = \{50, 150, 250\}$ m. As opposed to typical indoor user, the spatial resolution is now less sharp than the AF itself. Hence, the effect of the spatial resolution is paled by the channel itself. For the same configuration, the results in terms of average user throughput are provided in Fig. 3.20d. Remarkably, the throughput in the LOS case is again invariant with respect to the steering angle for all user distances d_{UE} , i.e., even at cell-edge. This is a particularity of the outdoor case and indicates that the indoor case is severely impacted by the wall penetration loss. The spatial resolution due to different steering angles is only observed under NLOS conditions and larger distances $d_{UE} = \{150, 250\}$ m.

3.5. Summary

This chapter introduces modeling of the 3D GSCM channel model in system-level tools. The first part of the chapter presents a detailed guideline for the practical implementation of the 3GPP 3D channel model into an existing system-level simulation tool. With previous state of the art channel models common for system-level tools, such as power delay profile (PDP)-based channels, Rayleigh or Rician fading, there is no interaction and no dependency of the channel generation with the geometry (i.e., location of users and BSs). Only a time dependency that is solved by pregenerating channel traces for longer periods of time. However with the GSCM channel model, the channel impulse response is both position and time dependent, therefore the channel has to be calculated at runtime. Facing the challenge of calculating the channel impulse response at simulation runtime, a model for partitioning the generation of the channel in several steps is introduced. From this point, a new time line structure for system-level tools is proposed that considers the spatio-temporal structure of the GSCM. Starting with the smallest resolution in time domain, that is the subframe level, referred to as time slot, quasi-stationary regions are defined denoting a larger time span during which large-scale parameters stay approximately constant. This time span is named *segment*, and several consecutive segments determine a chunk. Between chunks the scattering environment changes considerably, while within a chunk spatial correlation properties are preserved. Such structure simplifies the overall generation of the channel impulse response, while preserving the spatio-temporal characteristics of the channel model.

The validity of this modeling approach is demonstrated by integrating it into the Vienna LTEA Downlink System-Level Simulator, and recently in the novel Vienna 5G System-level simulator. The proposed time line structure for system-level tools paves the way for more advanced studies on the performance of a mobile cellular system in realistic environments. It enables analysing massive MIMO, 3D beamforming and beamtracking strategies, millimeter-wave (mm-Wave) scenarios and vehicular-use case scenarios.

Another important factor investigated, is the complexity increase of system-level simulations when considering the GSCM model and planar antenna arrays consisting of a large number of antenna elements. Analysis in terms of simulation run time show an approximately linear increase in simulation complexity with the number of antenna elements per antenna array. This confirms the expected result that the price to pay for modeling more than one antenna element per antenna port is nearly a linear increase in complexity for each additional antenna element per antenna port.

In the last part of this chapter, a systematic procedure to evaluate spatial resolution of large 2D antenna arrays is introduced. This part aims to evaluate the impact of a realistic channel model that considers multipath components when introducing sharp beams focused on specific locations in the cell. These evaluations are completed by means of system-level simulations considering a single BS-single user scenario. In particular, the impact of increasing the number of antenna elements in the vertical domain of the antenna array is analysed. While there exists an increase in received channel

energy when increasing the beam spatial resolution in elevation, this increase is not proportional with respect to the increase in the number of antenna elements. Therefore, the difference between 10 and 100 antenna elements is by far not as distinct as one might expect. Nevertheless, the larger number of antenna elements still has the advantage of a much better spatial resolution. The fact that these results hamper the derivation of further simple rules of thumb should raise awareness on the distinct impact of the channel on both indoor and outdoor transmissions, especially under NLOS conditions.

The chapter does not address performance evaluation of multiple users in one cell, because a spatial separation between users is not supported by the considered channel model. The channel model is not spatially consistent, meaning that two users located in proximity to each other, have completely uncorrelated channels. Thus, the model cannot be used for simulations requiring spatial consistency and is therefore, without further enhancements, not well suited for system-level simulations. The next chapter provides modeling of spatial consistency to make the GSCM valid and applicable for system-level tools.

4

Modeling Spatial Correlation for Geometry-based Stochastic Channel Models

The key aspect of wireless cellular networks is that they allow for mobility of the users. In the context of such a dynamic setting, the propagation conditions will evolve over time [1, 56, 107]. Nevertheless, the environment, that defines the propagation path, will only change its characteristics gradually. As a consequence, the propagation characteristics of two closely spaced user positions are bound to be similar. This spatial correlation has to be captured by the applied channel model, and is true for the large-scale conditions of a link (e.g., shadowing by buildings) as well as for the evolution of the small-scale fading. In this chapter, spatial correlation of geometry-based stochastic channel models is studied. A novel model for spatial consistency that is applicable to all prevalent geometry-based stochastic channel models is introduced. The enhancement with spatial consistency enables investigations on system-level tools of various applications such as channel quality feedback, beam tracking strategies, advanced beam forming strategies based on user location or angular information, i.e., multi-layer precoding [46, 70].

The geometry-based stochastic channel modeling described in Section 3.1 has been designed according to the *drop concept*, thus being suitable for system-level tools, where simulations are performed in a sequence of drops [72, 18]. A drop is defined as one simulation run with a certain duration in time during which the random properties of the channel remain constant except the Doppler component. In this way, motion is only virtual and causes small-scale fading (small-scale parameters (SSPs)) to evolve only due to the Doppler component, other geometry-related parameters stay fixed. As soon as the large-scale parameters (LSPs) and SSPs are updated, i.e., to the new neighbouring position due to movement, the model fails to give an accurate performance due to the lack of spatial correlation in SSPs between spatial positions. The same is true for static user positions where regardless of their

respective locations, the corresponding propagation parameters appear to be completely uncorrelated between users. The reason for such behaviour comes from the fact that in SSPs modeling, random variables are assigned independently to each spatial position.

Additionally to the spatial inconsistency in small-scale fading, the geometry-based stochastic channel models exhibit lack of spatial correlation in propagation conditions for neighbouring locations. This includes, the line of sight (LOS) and non line of sight (NLOS) propagation condition as well as Indoor/Outdoor state of users, that are determined from Bernoulli distributed independent trials. For both cases, it results in having no correlation in neighbouring positions, a behaviour that does not reflect real-world scenarios.

With the aim to provide spatial consistency to such channel models and based on my work in [74, 92], the contributions of this chapter are:

- A model for spatially consistent LOS/NLOS propagation condition and Indoor/Outdoor state of the user. The model delivers a spatially correlated behaviour over user locations based on 2-dimensional (2D) spatial filtering, yielding a realistic behaviour in urban environments where the LOS/NLOS propagation condition and Indoor/Outdoor state are effected from blockages.
- A model for spatially consistent small-scale fading, applicable to all prevalent geometry-based stochastic channel models such as those specified in 3rd Generation Partnership Project (3GPP) TR36873 and TR38901. The main idea of the model stands in correlating random variables between spatial locations. The model is characterized by a single parameter, the de-correlation distance, that indicates the range in which random variables are independently generated.
- A general step-wise procedure on how to implement the channel model with spatial consistency is provided, thus supporting the ease of implementation in fifth generation (5G)-and beyond system-level simulation tools.

4.1. Introduction

To overcome the lack of spatial consistency, a few approaches have been reported in literature that tackle differently with the structure of geometry-based stochastic channels models. Thus, in the Wireless World Initiative New Radio (WINNER) II model, the propagation path is divided into smaller parts known as segments and a continuous channel evolution with smooth transitions between segments is considered. A channel segment represents a period of quasi-stationarity during which LSPs as well as velocity and direction-of-travel for mobile receiver, are practically constant. Two methods are proposed [18] to model the transition between the segments. The first one is based on the cluster death-birth process and recently has been resolved in the quasi deterministic radio channel generator (QuaDRiGa) model [48]. The second method is based on the appearance and disappearance of multipath components, according to a Markov process. Since for its application,

the parameters have not yet been extracted from measurements, this approach was never adjusted. Differently, in the COST 2100 channel model, a global set of scatterers is shared by all users through so-called visibility regions [32]. Even though this type of channel model supports spatial consistency, it is currently not widely accepted due to its high complexity and its limited support on propagation scenarios. Additionally, the few existing scenarios are parametrized only for a small range of carrier frequencies [68]. Furthermore, according to [35], this model is not suitable to be used with large antenna arrays since the spatial variation that comes with large antenna arrays is not considered in this model.

Recently, the 3GPP in the study item TR38901 specified a new 3-dimensional (3D) radio channel model, feasible for frequencies of future mobile networks ranging from 0.5 to 100 GHz that accounts also for spatial consistency. There exist major issues with this spatial consistency model; First of all, the model is not sufficiently detailed, by only describing the spatial correlation as a 2D random process based on the parameter-specific de-correlation distances. It is not clear how the parameter of de-correlation distance is applied to this 2D random process, and currently there is no openly available implementation of this method, nor results that show its behaviour. Although, in one of the 3GPP meeting reports in [62], a detailed spatial consistency description is provided, there is no evidence that links the two approaches together. By looking closely at the model in [62], it can be noticed that the interpolation method introduced there, fails to give a good approximation due to the fact that for equally separated locations, correlated values are different. Second, in the 3GPP TR38901, the same de-correlation distances are applied to all SSP parameters, even though each parameter, e.g., delay, azimuth of arrival (AoA), elevation of arrival (EoA), delivers different statistics and thus not necessarily the same de-correlation distance is applicable for all parameters. Third, in the 3GPP TR38901 some of the random parameters (i.e., cluster specific sign for angles of arrival and departure that fall in the range $[-180^\circ, 180^\circ]$) have to remain fixed during one simulation, regardless if the user changes its location, which imposes high correlation on the channel parameters. Similarly, the report in [62] employs the same method claiming that if this random parameter is not fixed but correlated over distance, it will lead to abrupt changes at certain locations along the distance. This issue will be treated in more detail in the next chapter, where we will see that fixing this parameter during one simulation regardless of the user changing its location, is also not a realistic assumption and will lead to the other extreme of introducing a very high correlation.

4.1.1. Spatial Consistency Model

In order to achieve spatial consistency to geometry-based stochastic channel models, a novel model is proposed in this chapter. The main idea of the model stands in correlating random variables between spatial locations. Figure 4.1 illustrates the extended version of this stepwise procedure, already discussed in Section 3.1, accounting for spatial consistency. Two additional steps are introduced, first in assigning spatially correlated propagation condition i.e., LOS/NLOS and Indoor/Outdoor state,

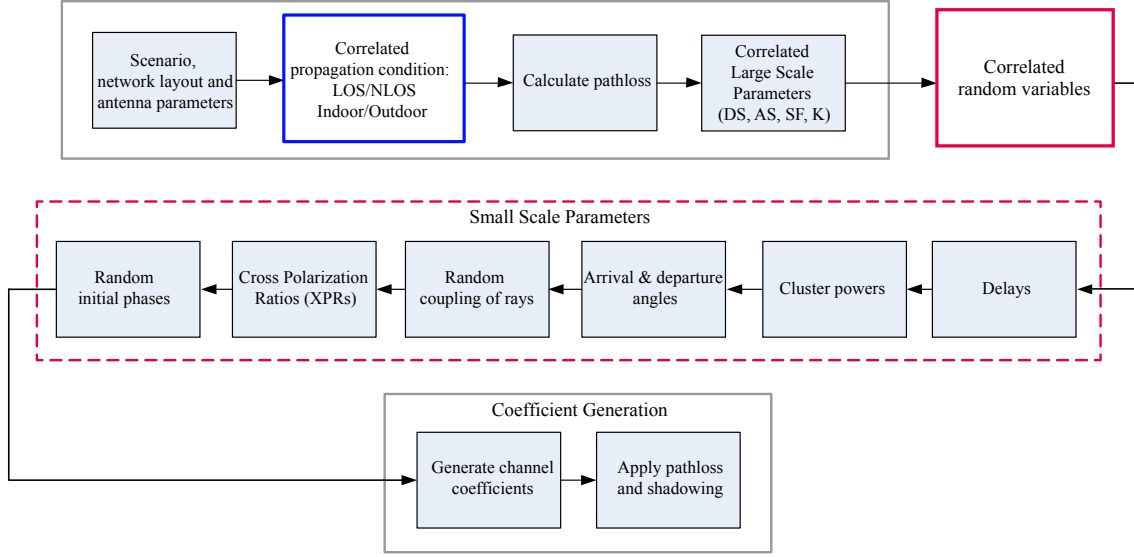


Figure 4.1.: Procedure of generating channel coefficients for geometry-based stochastic channel models, example of the 3GPP 3D channel model including necessary extensions to add spatial consistency, as indicated with blue and red color boxes.

and second, in spatially correlated SSPs, as denoted in Fig. 4.1 with the blue and red color boxes, respectively. Next, each of the two steps will be elaborated separately.

4.2. Modeling Spatially Correlated LOS/NLOS and Indoor/Outdoor state

4.2.1. Correlated LOS/NLOS State

Geometry-based stochastic channel models randomly select between LOS and NLOS propagation according to a distance dependent Bernoulli distribution defined with probability $p_{\text{LOS}}(d) \in [0, 1]$, where d denotes the distance between transmitter and receiver. When considering the 3GPP 3D urban macro cell (UMa) scenario, the probability of being in LOS is a function of the link between transmitter and receiver, considering both distance and receiver height $p_{\text{LOS}}(d, h_u)$,

$$p_{\text{LOS}}(d, h_u) = \begin{cases} 1, & d \leq 18 \text{ m} \\ \left[\frac{18}{d} + \exp\left(-\frac{d}{63}\right) \left(1 - \frac{18}{d}\right) \right] \left(1 + C'(h_u) \frac{5}{4} \left(\frac{d}{100}\right)^3 \exp\left(-\frac{d}{150}\right)\right), & d > 18 \text{ m} \end{cases}, \quad (4.1)$$

where

$$C'(h_u) = \begin{cases} 0, & h_u \leq 13 \text{ m} \\ \left(\frac{h_u - 13}{10}\right)^{1.5}, & 13 \text{ m} < h_u \leq 23 \text{ m} \end{cases}, \quad (4.2)$$

represents the dependency on the receiver height h_u . In the 3D urban micro cell (UMi) scenario, the probability of being in LOS simplifies to a distance-dependent function,

$$p_{\text{LOS}}(d) = \begin{cases} 1, & d \leq 18 \text{ m} \\ \frac{18}{d} + \exp\left(-\frac{d}{36}\right)\left(1 - \frac{18}{d}\right), & d > 18 \text{ m} \end{cases}. \quad (4.3)$$

Further, the LOS/NLOS condition for a specific position is obtained by a Bernoulli trial with the corresponding probability

$$k \sim \mathcal{U}(0, 1) \rightarrow \begin{cases} \text{LOS,} & \text{if } k \leq p_{\text{LOS}}(d) \\ \text{NLOS,} & \text{otherwise} \end{cases}, \quad (4.4)$$

where $\mathcal{U}(0, 1)$ denotes the uniform distribution in the interval $(0, 1)$. Figure 4.2a illustrates the LOS/NLOS condition relative to a transmitter located in the center (blue dot) for an area of size $500 \text{ m} \times 500 \text{ m}$. Since the LOS/NLOS realizations at all positions in the network are determined from independent trials by the distance-dependent Bernoulli distribution in Eq. (4.4), the LOS/NLOS conditions at two neighbouring positions are uncorrelated. This does not align with the behaviour that can be expected in a real-world scenario. In the 3GPP 3D channel model, the correlation of LSPs is achieved by correlating between normally distributed Gaussian random variables using an exponential filter function, as described in [18]. In order to introduce spatial correlation between LOS and NLOS condition, I propose to use an exponential filter impulse response similar to the correlation of LSPs, which is defined as

$$h(x, y) = \exp\left(-\frac{\|x - y\|_2}{\Delta}\right), \quad (4.5)$$

where $\|x - y\|_2$ denotes the distance between any two points x and y , and Δ represents the correlation distance. Instead of a uniform distribution for the LOS/NLOS decision as in Eq. (4.4), the approach is to start off with Gaussian distributions. For a map of size $M \times N$ pixels representing our region of interest (ROI), to each point $p_{m,n}$ independent and identically distributed (i.i.d.) Gaussian random variables are associated, $q_{m,n} \sim \mathcal{N}(0, 1)$. Next, by applying the spatial filter from Eq. (4.5) in x and y dimension, known as 2D filtering, correlated values $\tilde{q}_{m,n}$ are obtained for each point m, n in the map

$$\tilde{q}_{m,n} = \sum_{x=0}^M \sum_{y=0}^N h(x, y) q(m - x, n - y). \quad (4.6)$$

Knowing the cumulative distribution functions (CDFs) of the normal Gaussian distribution and the uniform distribution, the correlated Gaussian random variables are transformed into correlated

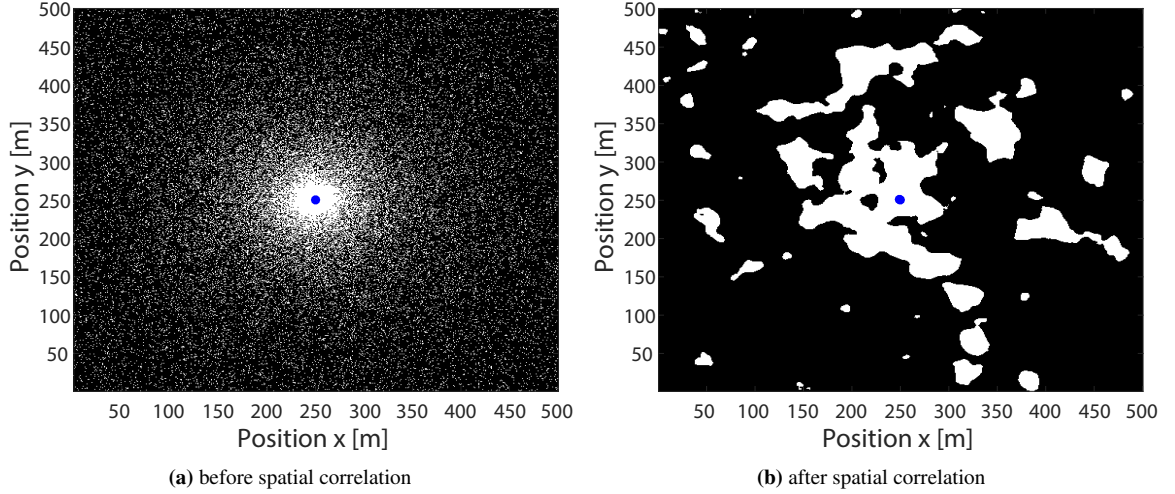


Figure 4.2.: LOS/NLOS state according to 3GPP 3D UMi scenario for an area $500 \text{ m} \times 500 \text{ m}$ with a transmitter located at the center. White pixels represent LOS state, black pixels NLOS. A correlation distance $\Delta = 15 \text{ m}$ is considered in the correlation model. ©2017 IEEE, [74].

uniform random variables by

$$\tilde{k} = g^{-1}(q) = F_{\tilde{k}}^{-1}(F_{\tilde{q}}(\tilde{q})), \quad (4.7)$$

where g^{-1} denotes the mapping function. The term $F_{\tilde{q}}(\tilde{q})$ represents the CDF of the Gaussian distribution and $F_{\tilde{k}}$ is the CDF of the uniform distribution. The correlated uniform random variable can be expressed as

$$\tilde{k} = \frac{1}{2} \left(1 + \operatorname{erf} \left(\frac{\tilde{q}}{\sqrt{2}} \right) \right), \quad (4.8)$$

where $\operatorname{erf}(x)$ is the error function [8]. Finally, to determine the LOS/NLOS condition, each correlated value \tilde{k} is compared to the LOS probability $p_{\text{LOS}}(d)$

$$a = \begin{cases} \text{LOS}, & \text{if } \tilde{k} \leq p_{\text{LOS}}(d) \\ \text{NLOS}, & \text{otherwise} \end{cases}. \quad (4.9)$$

One exemplary realization of a spatially correlated LOS/NLOS map is shown in Fig. 4.2b. As it can be seen, now clustered regions of LOS/NLOS positions are obtained, representing realistic behavior of urban environments on the horizontal plane. Increasing the distance from the transmitter, the size and the number of LOS regions reduces considerably.

To show the LOS/NLOS behavior determined by the obstruction of transmission link from explicitly placed blockages instead of probability functions, the Vienna 5G system-level simulator [87, 106] is considered. With 3D blockages resembling buildings, randomly generated cities can be created. A randomly generated urban environment with blockages randomly distributed on a simulation area of

500 m × 500 m is considered. Each blockage is characterized by a rectangular shape with dimensions 30 m × 30 m and a random height $h_b \sim \mathcal{U}(5, 20)$ m. The orientation of blockages with respect to the ground plane is also random. A representation of such environment in 3D and 2D is shown in Fig. 4.3a and Fig. 4.3b, respectively. Considering a transmitter placed at the center of simulation area with a height 25 m, the LOS/NLOS map of the simulation area is given in Fig. 4.3c. The white colour denotes LOS state, whereas the black one the NLOS state. The result shows than when considering an explicit modeling of blockages, the LOS/NLOS behaviour in terms of spatial correlation is similar to the one revealed from our model.

4.2.2. Correlated Indoor/Outdoor State

Similar to the LOS/NLOS case, in the 3GPP 3D channel model, the Indoor/Outdoor state for a specific position is obtained by a Bernoulli trial with the corresponding probability

$$l \sim \mathcal{U}(0, 1) \rightarrow \begin{cases} \text{indoor,} & \text{if } l \leq l_{\text{fraction}}, \\ \text{outdoor,} & \text{otherwise} \end{cases}, \quad (4.10)$$

where l_{fraction} is the fraction of area covered by buildings with $0 \leq l_{\text{fraction}} \leq 1$. If 50% of the area are covered by buildings, then $l_{\text{fraction}} = 0.5$.

Following the same procedure as described in Section 4.2.1, correlated uniform random variable are obtained,

$$\tilde{l} = \frac{1}{2} \left(1 + \text{erf} \left(\frac{\tilde{g}}{\sqrt{2}} \right) \right), \quad (4.11)$$

where \tilde{g} denotes the correlated Gaussian random variable similar to \tilde{q} obtained from Eq. (4.12),

$$\tilde{g}_{m,n} = \sum_{x=0}^M \sum_{y=0}^N h(x, y) g(m - x, n - y). \quad (4.12)$$

From this the Indoor/Outdoor state is determined by

$$b = \begin{cases} \text{indoor,} & \text{if } \tilde{l} \leq l_{\text{fraction}}, \\ \text{outdoor,} & \text{otherwise} \end{cases}. \quad (4.13)$$

The Indoor/Outdoor state generation considering an area of size 500 m × 500 m and $l_{\text{fraction}} = 0.5$ as defined in the 3GPP 3D channel model is shown in Fig. 4.4a. Figure 4.4b depicts the resulting spatially correlated Indoor/Outdoor state determined from Eq. (4.13) for $l_{\text{fraction}} = 0.5$ and $\Delta = 5$ m. The correlated map indicates a clustered behaviour of areas covered by buildings, representing a more realistic behaviour of the Indoor/Outdoor state.

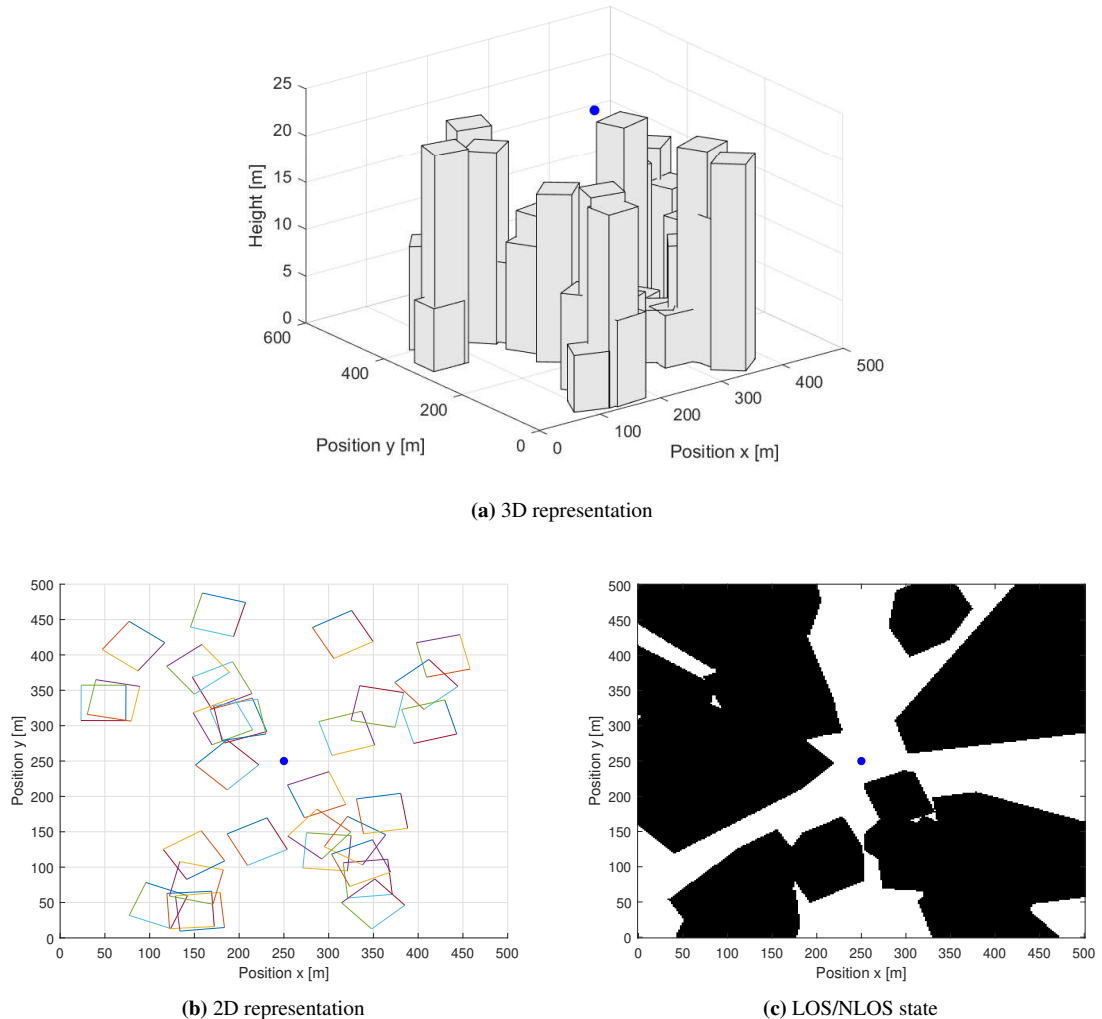


Figure 4.3.: Example of blockages randomly distributed and the corresponding LOS/NLOS state for the transmitter located in the center of an area $500 \text{ m} \times 500 \text{ m}$. White color denotes the LOS state, black color the NLOS state.

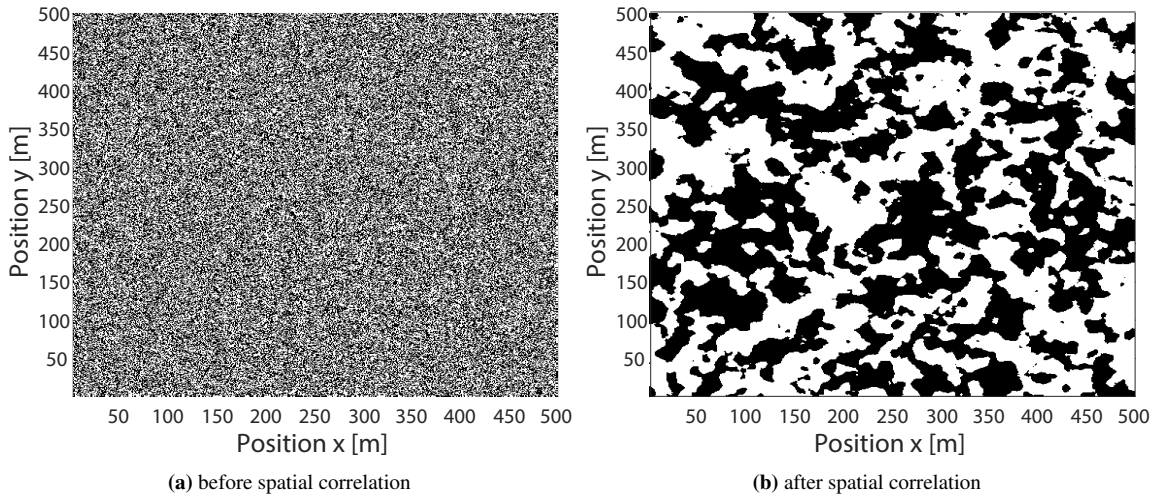


Figure 4.4.: Indoor/outdoor map of an area $500 \text{ m} \times 500 \text{ m}$ with $l_{\text{fraction}} = 0.5$ as specified in the 3GPP 3D channel model. A correlation distance $\Delta d = 5 \text{ m}$ is considered in the correlation model. ©2017 IEEE, [74].

4.2.3. Evaluation of Statistics

Now a statistical evaluation of the proposed method described above is presented. A single transmitter that is located in the center of a ROI of size $500\text{ m} \times 500\text{ m}$ is considered. Utilizing the distance-dependent LOS probability of the 3GPP 3D UMi scenario [43], a comparison between this probability and the LOS probability obtained from correlated LOS/NLOS map is carried out, averaged over 500 realizations with correlation distance $\Delta d = 20\text{ m}$. Figure 4.5 shows the probability of being LOS in dependence of the distance d to the transmitter in the center of the network, as obtained with spatially correlated maps and the the prescribed equation for LOS probability as given in [43, Tab. 7.1-2], denoted by magenta line. A good agreement is observed between both cases. Similarly, to evaluate the obtained threshold of area covered by buildings from Eq. (4.13), after correlating between indoor and outdoor states, a ROI of size $500\text{ m} \times 500\text{ m}$ is considered. Results are shown in Fig. 4.6. A perfect agreement is depicted between the given threshold, l_{fraction} , and the one obtained after correlation.

Note that in the case of small map size, in order to obtain correct LOS/NLOS and Indoor/Outdoor statistics, it is necessary to consider the empirical mean and standard deviation of the map after filtering, e.g., in LOS/NLOS case, for the entire map Eq. (4.8) formulates as

$$\tilde{K} = \frac{1}{2} \left(1 + \operatorname{erf} \left(\frac{\tilde{Q} - \mu}{\sigma \sqrt{2}} \right) \right). \quad (4.14)$$

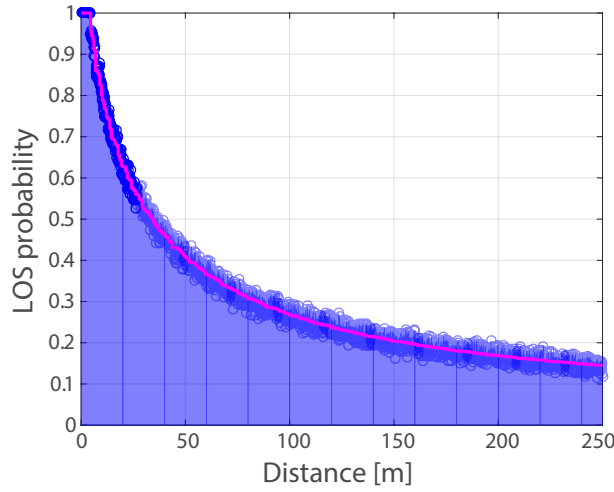


Figure 4.5.: LOS probability for outdoor users in the 3GPP 3D UMi scenario as specified in [43] and obtained with spatially correlated LOS/NLOS maps. ©2017 IEEE, [74].

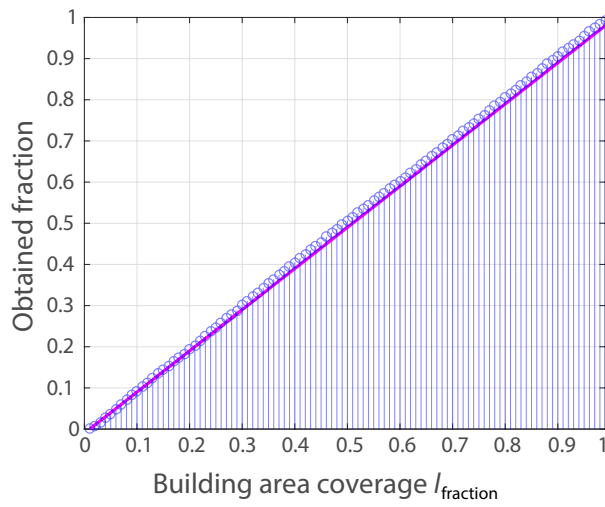


Figure 4.6.: Fraction of area covered by buildings as obtained with spatially correlated Indoor/Outdoor state maps, for $l_{\text{fraction}} = [0, 1]$ and correlation distance $\Delta = 5$ m. ©2017 IEEE, [74].

Table 4.1.: Random variables used in SSP as specified in the 3GPP 3D channel model [43, 72].

SSP specific random variables	Distribution
Cluster delay	$P \sim \mathcal{U}(0, 1)$
Cluster shadowing term	$Q \sim \mathcal{N}(0, \zeta^2)$
Cluster angle sign	$R \sim \mathcal{U}(\{-1, 1\})$
Cluster angular variation	$S \sim \mathcal{N}(0, \sigma_{AS}^2)$
Cluster and ray XPR	$V \sim \mathcal{N}(\mu_{XPR}, \sigma_{XPR}^2)$
Cluster and ray initial phase	$Z \sim \mathcal{U}(-\pi, \pi)$

4.3. Modeling Spatially Correlated Small-scale Parameters

The SSP stepwise model is already discussed in Section 3.1. In this model, as indicated in Fig. 4.1, the multipath components are characterized with delay, power and angels of arrival- and departure. Several distributions are considered to model the behaviour of multipath components. For instance, inverse Gaussian and inverse Laplacian are used to model angles of arrival and departure for azimuth and elevation, whereas multipath delays follow an exponential distribution. Additionally, several random variables are introduced either as input to the prescribed distribution functions or as additional components. Table 5.1 lists the random variables for the generation of SSPs according to the 3GPP 3D channel model in [43] and [72].

4.3.1. Correlated Random Variables

To introduce spatial correlation in SSPs, a correlation applied to all random variables is proposed. As indicated in red in Fig. 4.1 by the red box, the random variables are correlated separately before the actual SSP generation. This means that the spatio-temporal properties of the model will be inserted by pre-calculating all random variables for all user locations and moving user trajectories, and these are utilized correspondingly in the consecutive SSP generation steps. Details on how to generate correlated random variables in the model are described in the following.

1. Generate a matrix \mathbf{W} with its elements being independent random variables according to tabulated distributions from Table 5.1, e.g., $w_{i,j} \sim \mathcal{N}(\mu, \sigma^2)$. In relation to the geometry, matrix \mathbf{W} represents a grid of independent and uncorrelated random variables that is aligned with the scenario geometry, respectively with user positions in the horizontal plane. Therefore, the size of matrix \mathbf{W} is determined by the geometry of user locations. This is illustrated in Fig. 4.7, where gray circles represent entries of matrix \mathbf{W} , whereas coloured squares denote user locations. For K user locations given in Cartesian coordinates, $(x_1, y_1), (x_2, y_2), \dots, (x_K, y_K)$, the

size $I \times J$ of matrix \mathbf{W} is determined in x -direction as

$$J = \left\lceil \frac{|\min(x_1, x_2, \dots, x_K) - \max(x_1, x_2, \dots, x_K)|}{\Delta d} + 1 \right\rceil, \quad (4.15)$$

and in y -direction as

$$I = \left\lceil \frac{|\min(y_1, y_2, \dots, y_K) - \max(y_1, y_2, \dots, y_K)|}{\Delta d} + 1 \right\rceil. \quad (4.16)$$

The parameter Δd represents the geometrical resolution that comes with matrix \mathbf{W} and indicates the range in which random variables are independently generated. I will refer to Δd as de-correlation distance in the rest of the paper. It should be noted that Δd is a statistical parameter and does not represent the actual distance in meters as for example the well-known model in [5]. Choosing different values of Δd , the model yields different correlation levels of channel parameters.

2. For each user location, the four neighbouring entries of matrix \mathbf{W} are determined by mapping functions in x and y directions

$$j = \left\lceil \frac{x - \max(x_1, x_2, \dots, x_K)}{\Delta d} \right\rceil, \quad (4.17)$$

and

$$i = \left\lceil \frac{y - \max(y_1, y_2, \dots, y_K)}{\Delta d} \right\rceil, \quad (4.18)$$

where x and y denote the actual user location.

3. To get the correlated random variable $\tilde{w}(x, y)$ for the corresponding user position (x, y) , a bilinear interpolation is applied

$$\begin{aligned} \tilde{w}(x, y) = & \frac{1}{(x_i - x_{i-1})(y_j - y_{j-1})} [x_i - x \quad x - x_{i-1}] \\ & \begin{bmatrix} w_{i-1,j-1} & w_{i-1,j} \\ w_{i,j-1} & w_{i,j} \end{bmatrix} \begin{bmatrix} y_j - y \\ y - y_{j-1} \end{bmatrix}. \end{aligned} \quad (4.19)$$

with $w_{i-1,j-1}, w_{i-1,j}, w_{i,j-1}, w_{i,j}$ being the four neighbouring entries from matrix \mathbf{W} .

4.3.2. Statistical Properties

Correlation Coefficient

The correlation and covariance of two random variables provide second-order measures of the statistical dependence between these two variables. The correlation coefficient between two random

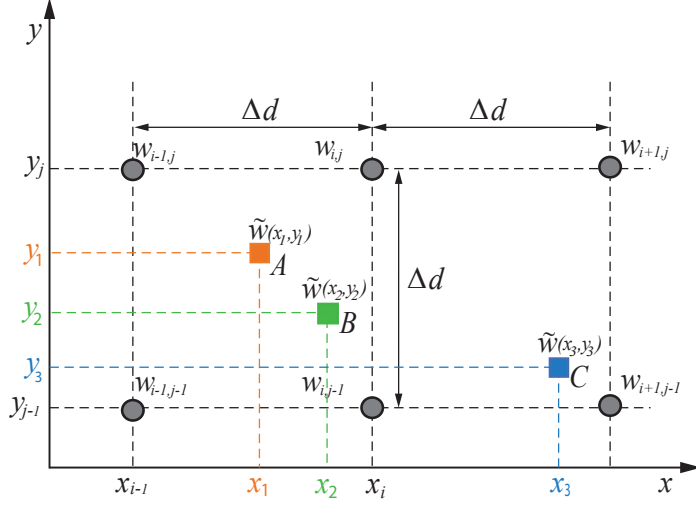


Figure 4.7.: Independent and randomly distributed variables generated on a rectangular grid denoted by gray circles. The grid size spans the entire simulation area and has a fixed resolution, the de-correlation distance Δd . For each user location A, B and C, correlated random variables are estimated by bilinear interpolation.

variables E_0, E_1 is defined as

$$\rho(E_0, E_1) = \frac{\text{Cov}(E_0, E_1)}{\sqrt{\text{Var}(E_0)\text{Var}(E_1)}}. \quad (4.20)$$

The maximum and minimum values of correlation coefficient are,

- $\rho(E_0, E_1) = 0$ as lower bound when E_0, E_1 are uncorrelated random variables as covariance $\text{Cov}(E_0, E_1) = 0$,
- $|\rho(E_0, E_1)| = 1$ as upper bound.

Let $\mathcal{T} \in \mathbb{R}^2$ be a set of consecutive locations in Cartesian coordinates (x_k, y_k) with $k \in \{0, 1, 2, \dots, 150\}$ following a straight line, as illustrated in Fig. 4.8. Now, consider a set of random and independent variables, $E \sim \mathcal{N}(0, 1)$, distributed in a grid with resolution Δd , as shown in Section 4.3. The set of random variables E can be seen as entries of matrix \mathbf{W} from our previous explanation. By applying our correlation model, after bilinear interpolation, a correlated random variable is assigned to each location, e.g., \tilde{E}_0 is the random variable at location x_0, y_0 , whereas \tilde{E}_k is the random variable at location x_k, y_k . The correlation coefficient between the correlated random variable in the first location, \tilde{E}_0 and consecutive locations \tilde{E}_k , denoted as $\rho(\tilde{E}_0, \tilde{E}_k)$, considering 500 realizations, is shown in Fig. 4.9, represented with dashed lines. As expected, the correlation drops to zero at Δd , due to the fact that the random variables are independent at Δd .

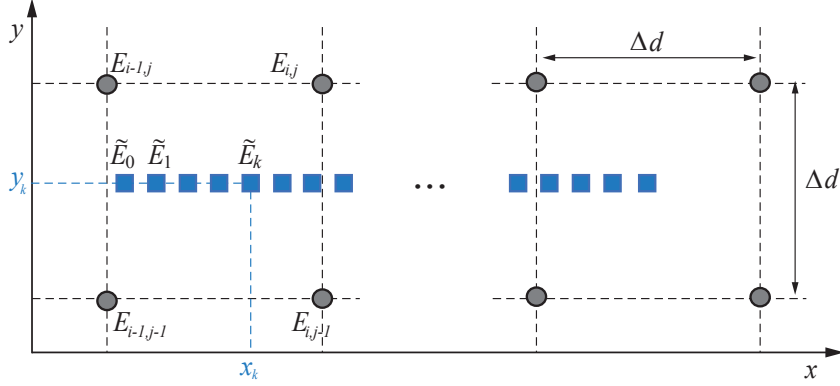


Figure 4.8.: Consecutive locations in Cartesian coordinates (x_k, y_k) following a straight line and independent random variables E distributed in a grid with resolution Δd .

Correlation function

Our correlation model, depending on the de-correlation distance Δd , can be approximated as sum of sinusoids with the function,

$$\Psi(x) = \begin{cases} a_1 \sin(b_1 (\Delta d)^{-1} x + c_1) + \\ a_2 \sin(b_2 (\Delta d)^{-1} x + c_2), & 0 \leq x \leq \Delta d \\ 0, & x > \Delta d \end{cases} \quad (4.21)$$

with parameters $a_1 = \frac{136}{125}$, $b_1 = \frac{5}{4}$, $c_1 = \frac{37}{20}$, $a_2 = \frac{1}{16}$, $b_2 = \frac{200}{31}$ and $c_2 = -\frac{3}{4}$. As shown in Fig. 4.9, the approximated function $\Psi(x)$ represented by the solid blue line is a good fit to our correlation model.

4.3.3. Spatially Correlated SSP Model

In the step-wise procedure of generating the SSPs as provided in the 3GPP 3D channel model and elaborated in Section 3.1, multipath delays are modeled following an exponential distribution [43, Tab. 7.3-6]. In this way, the delay for each cluster is defined as

$$\tau_n = -r_\tau \sigma_{DS} \ln(X_n), \quad (4.22)$$

where r_τ is the delay proportionality factor, σ_{DS} denotes the delay spread, $n = 1, 2, \dots, N$ is the cluster index and $X_n \sim \mathcal{U}(0, 1)$ is the random variable that needs to be correlated.

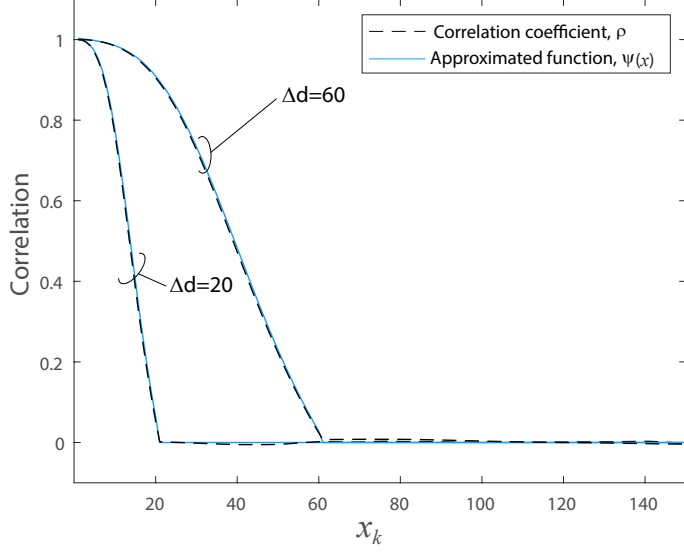


Figure 4.9.: Correlation of random variables for different values of de-correlation distance using the correlation coefficient ρ and approximated correlation function $\Psi(x)$.

By applying our model model for spatial consistency, instead of variable X_n , independent random variables $L \sim \mathcal{U}(0, 1)$ are generated according to a grid with geometrical resolution Δd , as described in Section 4.3. After obtaining the correlated random variables for each user location, Eq. (4.22) is modified by introducing the correlated random variable $\tilde{l}_n(x, y)$ for the corresponding user position x, y and n -th cluster,

$$\tau_n = -r_\tau \sigma_{\text{DS}} \ln(\tilde{l}_n(x, y)). \quad (4.23)$$

This describes *Step 5* of SSP for the channel models in [43, 72], modeling multipath delays.

Following our correlation method, the subsequent steps in SSP model as given in [43, 72] are modified as below:

Step 6: Cluster powers:

$$P_n = \exp\left(-\tau_n \frac{r_\tau - 1}{r_\tau \sigma_{\text{DS}}}\right) 10^{\frac{-\tilde{q}_n(x, y)}{10}}, \quad (4.24)$$

where $\tilde{q}_n(x, y)$ is the correlated random variable obtained by bilinear interpolation of $Q \sim \mathcal{N}(0, \zeta^2)$, with ζ being the variance of shadowing term.

Step 7: Arrival- and departure angles for azimuth (ϕ) and elevation (θ):

$$\phi_{n, \text{AoA}} = \tilde{r}_n(x, y) \phi'_{n, \text{AoA}} + \tilde{s}_n(x, y) + \phi_{\text{LOS}, \text{AoA}}, \quad (4.25)$$

and

$$\theta_{n, \text{EoA}} = \tilde{t}_n(x, y) \theta'_{n, \text{EoA}} + \tilde{u}_n(x, y) + \theta_{\text{LOS}, \text{EoA}}, \quad (4.26)$$

where $\tilde{r}_n(x, y)$ and $\tilde{t}_n(x, y)$ are correlated random variables drawn after the bilinear interpolation of $\mathcal{U}(\{-1, 1\})$. Since the generation of azimuth and elevation angles is done independently, I distinguish between $\tilde{r}_n(x, y)$ and $\tilde{t}_n(x, y)$. The component $\tilde{s}_n(x, y)$ denotes the correlated random variable obtained by bilinear interpolation of $S \sim \mathcal{N}(0, \sigma_{ASA}^2)$ that introduces an angular variation. Similarly, for elevation case, $\tilde{u}_n(x, y)$ is the correlated random variable after interpolation of $U \sim \mathcal{N}(0, \sigma_{ESA}^2)$. The third term in Eqs. (5.11) and (4.26), $\phi_{LOS,AoA}$ and $\theta_{LOS,EoA}$, represents the angle of the LOS link between transmitter and receiver location for azimuth and elevation respectively. The parameters $\phi'_{n,AoA}$ and $\theta'_{n,EoA}$ denote the probability distribution functions for azimuth and elevation angles and are defined with Eq. (2.5) and Eq. (2.7) from Section 2.4.3.

Step 8: Coupling of rays within a cluster for both azimuth and elevation:

The random coupling between arrival and departure angles is kept fixed during one simulation.

Step 9: Cross polarization power ratios:

$$\kappa_{n,m} = 10^{\frac{\tilde{v}_{x,y}}{10}}, \quad (4.27)$$

where $\tilde{v}_{x,y}$ is the correlated random variable obtained by bilinear interpolation of $V \sim \mathcal{N}(\mu_{XPR}, \sigma_{XPR}^2)$. The cross polarization ratio is specific for each cluster and ray within cluster, as denoted by indices n and m , respectively, therefore matrix \mathbf{V} will have four dimensions, $I \times J \times N \times M$.

Step 10: Draw initial phases:

$$\varphi_{n,m} = \tilde{z}(x, y), \quad (4.28)$$

where $\tilde{z}(x, y)$ is the correlated random variable obtained from $Z \sim \mathcal{U}(-\pi, \pi)$. Initial phase is specific for each cluster and ray within the cluster.

4.4. Summary

In this chapter, two models are presented that add spatial consistency to the geometry-based stochastic channels. The first model, introduces spatial correlation among neighbouring user locations for LOS/NLOS propagation condition and Indoor/Outdoor state. The model applies a 2D spatial filtering on normally distributed random variables followed by a mapping from correlated normally distributed random variables to uniformly distributed random variables. It is observed that the model captures similar behaviour as in the case when considering an explicit modeling of blockages in 3D.

The second model introduces spatial consistency to small-scale fading enabling thus system-level investigations of scenarios with user mobility, massive multiple-input multiple-output (MIMO) and multi-user schemes, beamforming etc. A generalized procedure of spatial consistency is presented, applicable to all standardized geometry-based channel models and adjusted for system-level tools supporting 5G. The principle of the model is to correlate all random variables based on a distance-dependency, represented by the de-correlation distance parameter. The model allows a pre-generation step of all random variables that are correlated by employing bilinear interpolation. These correlated

random variables, are then applied in the SSPs step-wise generation. Analysing the statistical properties of the model, it is shown that second order sum of sinusoids is a good approximation of the correlation function that the proposed model achieves.

In the next chapter, a deeper investigation on spatial correlation of small-scale fading is introduced. In particular, ray-tracing simulations are carried out to statistically evaluate and validate the behavior in terms of spatial correlation over distance. The particular focus lies on parametrizing the spatial consistency model by finding the corresponding values for de-correlation distances that deliver a realistic behaviour in terms of spatial correlation.

5

Statistical Evaluation of Spatial Consistency Model based on Ray-Tracing

In this chapter, the spatial consistency model of small-scale fading, introduced in Chapter 4, is evaluated and validated by comparing with statistical channel properties from ray-tracing simulations. Following hypothesis testing over obtained ray-tracing statistics, the spatial consistency model is parametrized for various 3GPP scenarios under LOS and NLOS propagation conditions.

As discussed in Section 2.4, in the geometry-based stochastic channel models the location of scatterers is not explicitly modeled, but rather angles of arrival- and departure, delays and powers of multipath components follow defined distribution functions [43, 15, 18]. Deterministic channel models, on the other hand, completely depend on the geometry of the environment (which is known), and are by design spatially consistent. Therefore, in this chapter a ray-tracing simulator is utilized in order to validate and parametrize the proposed spatial consistency model of SSPs. However, to allow parametrization of a stochastic model, it is necessary to simulate many ray-tracing scenarios that share certain characteristics (i.e., building density, average building height, average street width, etc.) and obtain statistical measures. Such characteristics are carefully chosen to be consistent with the scenarios from 3GPP 3D channel model defined in Technical Reports TR 36973 and TR 38901 [43, 72], representing the most common model of standardized geometry-based stochastic channels. Another reason for depicting the 3GPP 3D channel model, is that it supports various scenarios such as urban, urban street canyon and rural, and is applicable to a large range of carrier frequencies that covers 0.5 to 100 GHz.

Based on my work in [91, 92, 84], the contributions of this chapter outline as follows:

- The behaviour of strongest multipath components over consecutive spatial positions is evaluated considering ray-tracing simulations in an urban environment. The spatial consistency model is able to capture similar characteristics as ray-tracing, where the propagation characteristics change gradually with distance reflecting the changes in geometry of surrounding objects along the propagation path.
- Validation of the spatial consistency model by performing extensive ray-tracing simulations and showing that the model is in a very good agreement with the statistical channel properties obtained from ray-tracing.
- Parametrization of de-correlation distance based on hypothesis testing over obtained ray-tracing statistics. The key idea is to find the de-correlation distance that gives the closest result to the ray-tracing statistics. This is achieved by employing rejection rates from hypothesis testing. Based on the results, de-correlation distance values for various scenarios are determined. The values distinguish between scenarios as well as LOS and NLOS propagation condition.

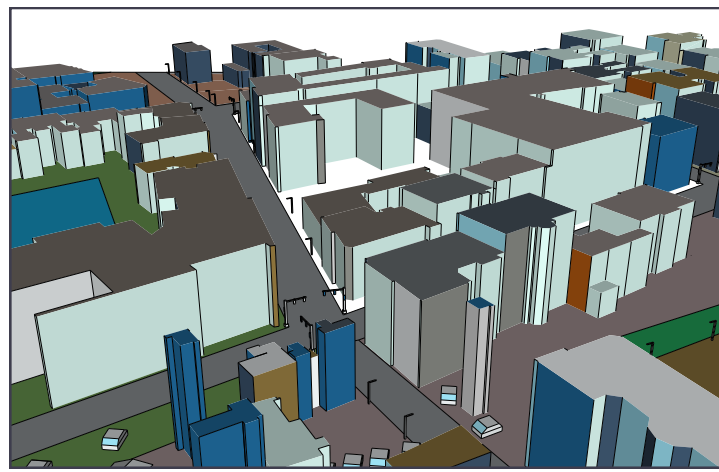
5.1. Deterministic Model - Ray Tracing

For validation of the behavior of the proposed spatial consistency model, a flexible ray-tracing simulator from [75, 77, 103] is employed. The ray-tracing is considered as a reference to compare with the spatial consistency model. Since the focus is to specifically observe the behaviour of small-scale parameters such as angles of arrival in azimuth and elevation, simulations with ray-tracing are advantageous because all the multipath characteristics are calculated and delivered as output. In contrary, when performing measurements, these parameters need to be estimated. Another advantage of ray-tracing tool is that various scenarios and unlimited number of realizations can be considered, without additional effort, except the computational one.

Ray-tracing applies as input a three-dimensional representation of the scenario, where the geometry and materials are carefully modeled. To model various scenarios handled then by ray-tracing, a 3D modeling software, SketchUP [104], is employed. In this way, artificial environments can be modeled based on geometric parameters of a realistic city (i.e., building density, building height, street width). Furthermore, to make the simulations even more realistic, there is the possibility to reproduce three-dimensional environments by getting the data from OpenStreetMap [101]. Examples of such environment representations are given in Fig. 5.1. Since the data from OpenStreetMap gives the geometry information only in 2D, the building height information can be added afterwards as for example, based on average building height parameter in compliance with the data from the 3GPP 3D channel model [43, 72].

Based on the geometry of the environment as well as location of transmitter and receiver, all ray paths are determined. The ray paths with their corresponding electromagnetic properties are considered

5.1. Deterministic Model - Ray Tracing



(a) urban environment



(b) rural environment

Figure 5.1.: Example of scenarios used in ray-tracing simulations. Different colours denote different material types.

for calculating and determining the complex field strengths of the multipath components. These calculations comprise of the free space loss, reflection losses as well as various diffuse scattering models such as the Kirchhoff and Lambertian scattering models [75, 86]. Depending on the scenario, various materials such as concrete, glass, metal, wood, marble, granite, etc., are considered. The electromagnetic permittivity and permeability of used materials is then handled by the ray-tracing simulator. Since the locations of the scatterers in a simulated environment are known, consequently the channel characteristics from a ray-tracing simulator are spatially consistent.

5.2. Analysis of Spatial Consistency in a Typical Urban Scenario

The characteristics of multipath components arriving at a specific location depend on the surrounding environment. By comparing these characteristics between different spatial positions, one can obtain insights on how fast the channel characteristics change due to the surrounding environment. Consider a straight trace with consecutive locations, $(x_0, y_0), (x_1, y_1), \dots, (x_K, y_K)$, equally separated with distance d , as illustrated in Fig. 5.2. The characteristics of multipath components will evolve with

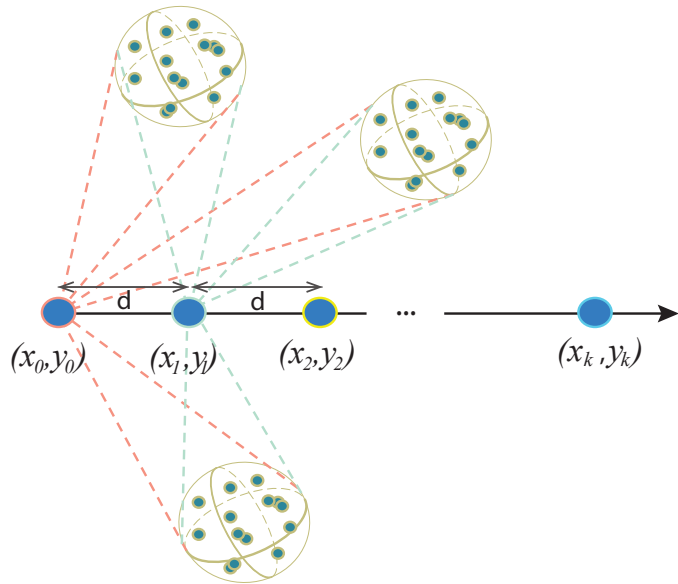


Figure 5.2.: Evolution of multipath characteristics over consecutive spatial locations.

distance. When such characteristics are described by stochastic models, as in the case of geometry-based stochastic channel models, it is desirable to observe a smooth and correlated behaviour in closely located positions, something that is easily observed in the case of deterministic models, i.e., ray-tracing simulations, or in the case of measurement data.

Table 5.1.: Simulation parameters.

Parameter	Value
Transmitter height	25 m
Receiver height	1.5 m
Average building height	20 m
Average street width	20 m
Antenna pattern	omni-directional
Carrier frequency	3.5 GHz

In this section, the behavior of the strongest multipath components over consecutive spatial locations is evaluated by means of ray-tracing and compared with the proposed model for spatial consistency considering urban environments as an example.

5.2.1. System Model

The macro cellular setup comprises a single base station and a straight user trace. The target is to analyze the behaviour of the strongest multipath components over consecutive spatial locations at the receiver. The 3GPP 3D channel model [63] is considered, extended with the spatial consistency model described in Section 4.3. With a view to urban environments where rich scattering occurs, the UMa scenario from [43] is selected. This scenario represents a typical urban environment considering a base station height of 25 m and an inter-site distance of 500 m. Therefore, for the single base station case, a simulation area of 300 m × 300 m is considered.

On the other hand, for comparison, a similar scenario geometry representing an urban environment is constructed to perform simulations with the ray-tracing from [103]. Figure 5.3a illustrates the scenario geometry together with base station and user trace locations. The base station is mounted on top of one of the buildings, whereas user locations are considered along a street. Individually, LOS and NLOS propagation conditions are analysed, thus two different transmitter locations are chosen, as indicated in Fig. 5.3a. Different material types for the constructed scenario are chosen from the material database provided in ray-tracing. Various colors in Fig. 5.3 represent different materials, e.g., brick, redbrick, glass, wood, tiles, asphalt, metal, etc.

In order to keep the comparison fair, in both channel models, 3GPP 3D model and ray-tracing, the parameters from Table 5.1 are applied. The building height follows the specifications in the 3GPP 3D model [43][Table 6-1 and Table 7.2-1], where the average building height is considered to be 20 m. The maximum height for a building according to this model is 24 m, representing approximately an eight-floor building which is typical for European cities. The same geometry of base station and user trace locations is applied in simulations with the 3GPP 3D channel model, as shown in Fig. 5.4. For

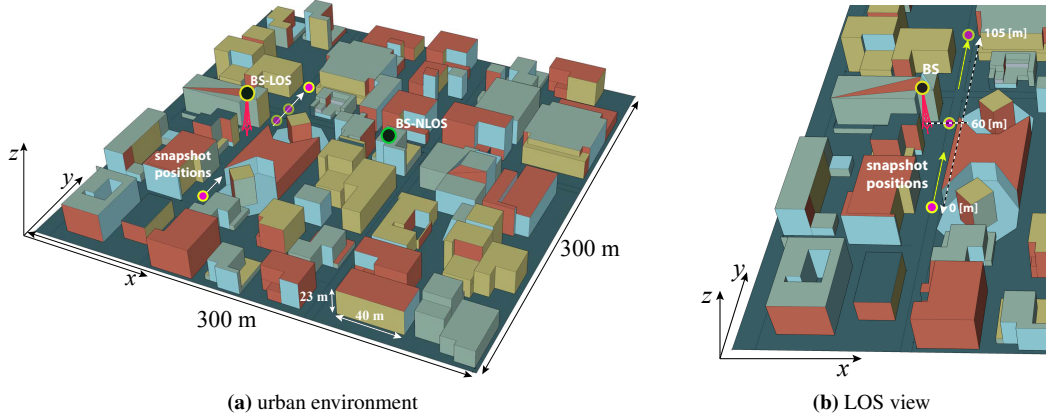


Figure 5.3.: The constructed scenario in 3D used in ray-tracing tool denoting base station positions and receive snapshot positions in LOS and NLOS. ©2019 IEEE, [91].

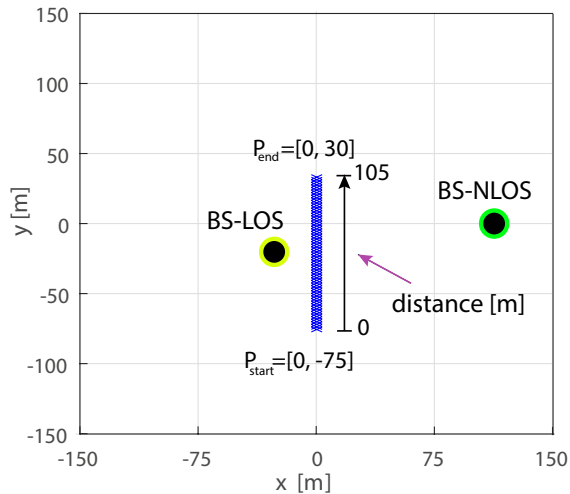


Figure 5.4.: Urban scenario with the corresponding geometry in 2D used with the 3GPP 3D channel model. The size of the scenario and corresponding transmitter- and receiver positions are the same as in the ray-tracing case. ©2019 IEEE, [91].

both cases, the base station consists of a single antenna with an omni-directional antenna pattern. Similarly, on the user side a single omni-directional antenna is considered.

5.2.2. Simulation Results

The length of recorded snapshots on the receive locations along the propagation path is 105 m, with a resolution every one meter between consecutive snapshots. The focus of these analysis is on observing three characteristics of multipath components: normalized delay, AoA and EoA. The normalized delay is defined as the multipath delay subtracted with the delay of the LOS path. Since in ray-tracing the number of multipath components is very high, only the strongest ones are considered. The behaviour of the direct path and the strongest multipath when considering the LOS propagation condition, is shown in Fig. 5.5. Ray-tracing results in Fig. 5.5 (a), (c) and (e) reveal a smooth behaviour of delay, AoA and EoA over spatial locations for the direct path, following the geometry of the surroundings at transmit-receive locations. Note that in the last spatial positions, the direct path shows some fluctuations in terms of delay, AoA and EoA, because the receiver locations are not in LOS any more due to obstruction from the building corner (see Fig. 5.3b). When looking at the first strongest multipath component, as expected, the behaviour is more disruptive over spatial locations compared to the LOS due to reflection, diffraction and scattering effects. Especially, more intersperse changes are noticed at the locations close to the base station where the buildings around consist of many corners and unflattering surfaces.

On the other hand, the results from the 3GPP 3D model, depicted in Fig. 5.5 (b), (d) and (f), indicate a similar behaviour when using spatial consistency model with presumed values of de-correlation distance, $\Delta d = \{5, 10, 15\}$. Since in the 3GPP 3D channel model, the scatterers are generated statistically, it is expected that the multipath components will not follow the exact behaviour as the ones in ray-tracing. However, the objective is to rather observe whether the spatial consistency model reveals similar characteristics as ray-tracing, with appearance and disappearance of scatterers over distance. In general, such behaviour is notable in both LOS and NLOS propagation conditions. The results for NLOS are depicted in Fig. 5.6. Furthermore, similarly to the ray-tracing results, abrupt changes of channel parameters occur with the spatial consistency model, reflecting thus the changes in geometry of surrounding objects along the propagation path. In contrary to the spatial consistency model, the results of the 3GPP 3D model without spatial consistency (green line in Fig. 5.5 and Fig. 5.6) show very large fluctuations along consecutive spatial positions resulting in a completely spatially inconsistent behavior.

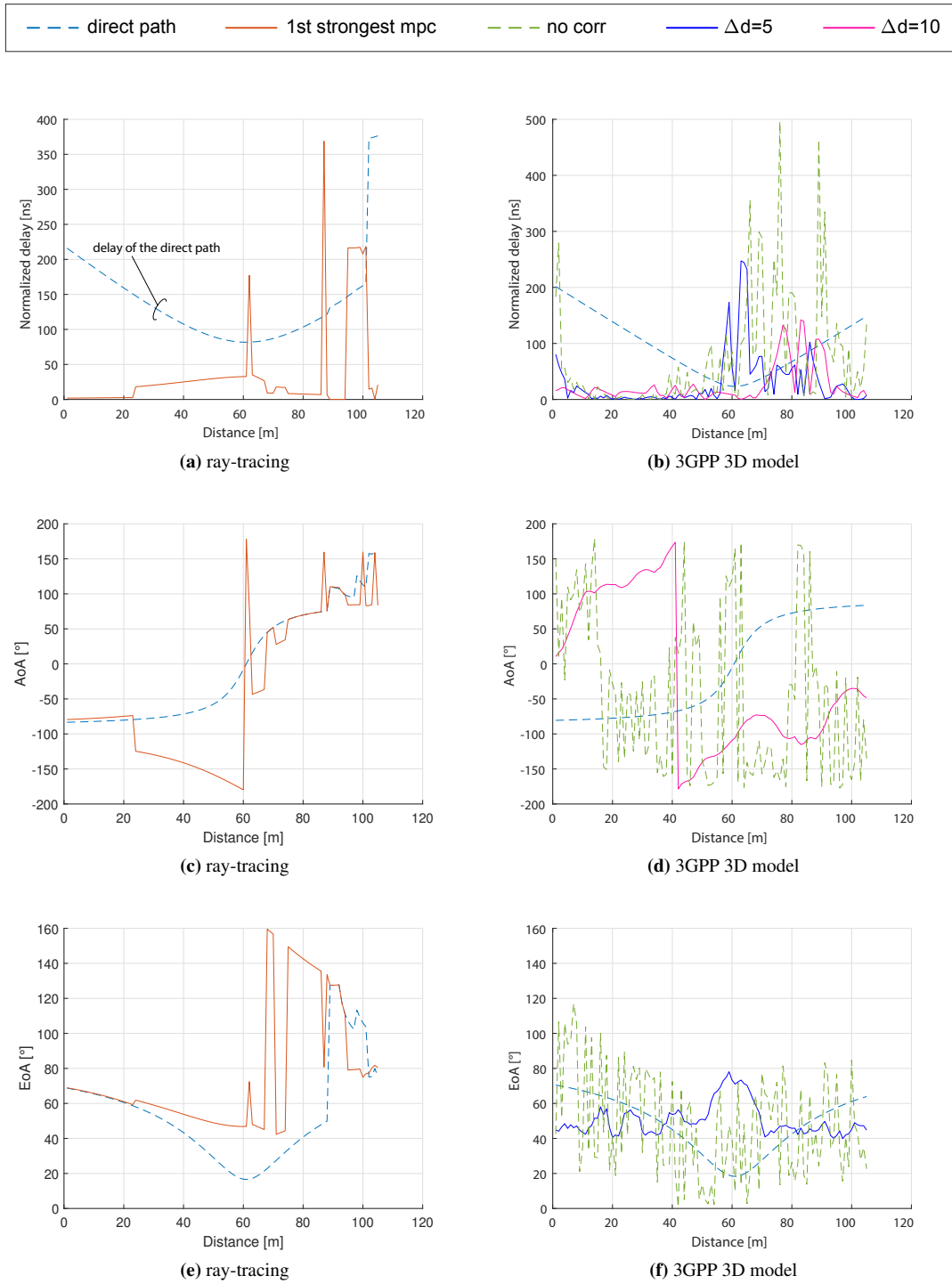


Figure 5.5.: Characteristics of the direct path and the strongest multipath components for spatial positions in LOS propagation condition for ray-tracing and 3GPP 3D model with- and without spatial consistency. ©2019 IEEE, [91].

5.2. Analysis of Spatial Consistency in a Typical Urban Scenario

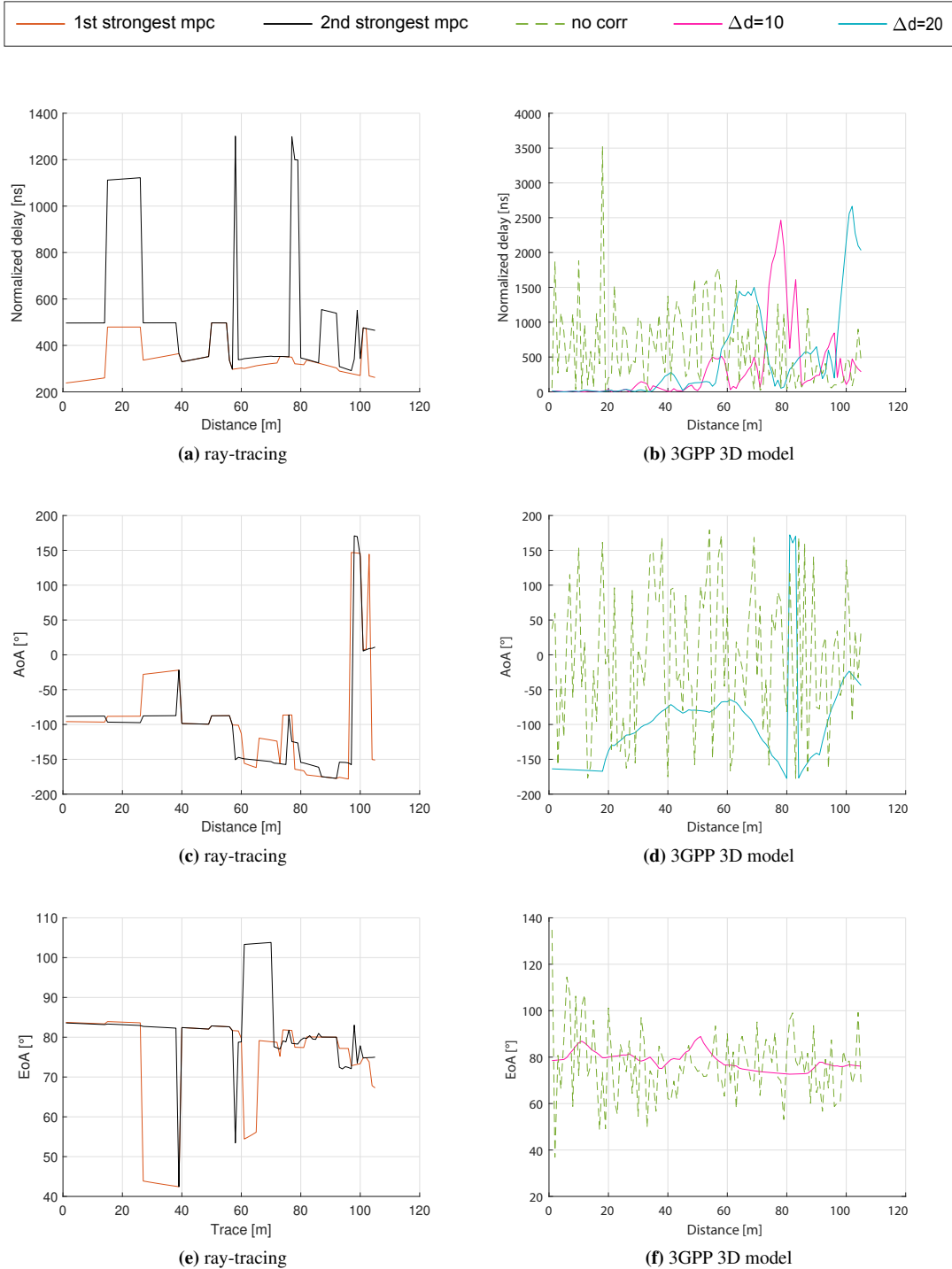


Figure 5.6.: Characteristics of the direct path and the strongest multipath components for spatial positions in NLOS propagation condition for ray-tracing and 3GPP 3D model with- and without spatial consistency. ©2019 IEEE, [91].

5.3. Statistical Evaluation of Spatially Correlated SSP Model

After observing the changes over distance of multipath components for a specific geometry, in this section, a statistical evaluation is conducted regarding both ray-tracing and geometry-based stochastic channel model. The aim is to first obtain statistical measures from ray-tracing and use those statistics to validate the proposed model for spatial consistency from Section 4.3.

5.3.1. Statistical Analysis

To measure the changes in all existing multipath components between spatial locations, the correlation coefficient is employed. Since in the SSP model, characterization of multipath components follows a stepwise generation of multipaths starting with delays, followed by multipath powers and next multipath angles, the focus of these analysis is on the angular characteristics at the receiver, i.e., AoA and EoA. In this way the accumulated impact of the correlation model applied to multipath delays, powers and angles of arrival/departure¹ is examined.

Since AoA and EoA are characterized by circular distributions, the circular correlation coefficient [4] is employed, in order to determine the correlation between two data sets of angular variables, i.e., α_0 and α_k at two different locations,

$$\rho_k = \frac{\sum_{m=1}^M \sin(\alpha_{m,0} - A_0) \sin(\alpha_{m,k} - A_k)}{\sqrt{\sum_{m=1}^M \sin^2(\alpha_{m,0} - A_0)} \sqrt{\sum_{m=1}^M \sin^2(\alpha_{m,k} - A_k)}}, \quad (5.1)$$

with angular sample means

$$A_0 = \tan^{-1} \frac{\sum_{m=1}^M \sin(\alpha_{m,0})}{\sum_{m=1}^M \cos(\alpha_{m,0})}, \quad (5.2)$$

and

$$A_k = \tan^{-1} \frac{\sum_{m=1}^M \sin(\alpha_{m,k})}{\sum_{m=1}^M \cos(\alpha_{m,k})}. \quad (5.3)$$

In this case, the variable M represents the total number of multipaths at a given spatial position, whereas the subscripts 0 and k denote the respective spatial positions under observation, as illustrated in Fig. 5.2.

5.3.2. Simulation Results

Geometry-based stochastic channel model

Three scenarios according to the 3GPP 3D channel model in [72] are analysed:

¹See e.g., Section 4.3.3 with details on correlated SSP stepwise generation procedure.

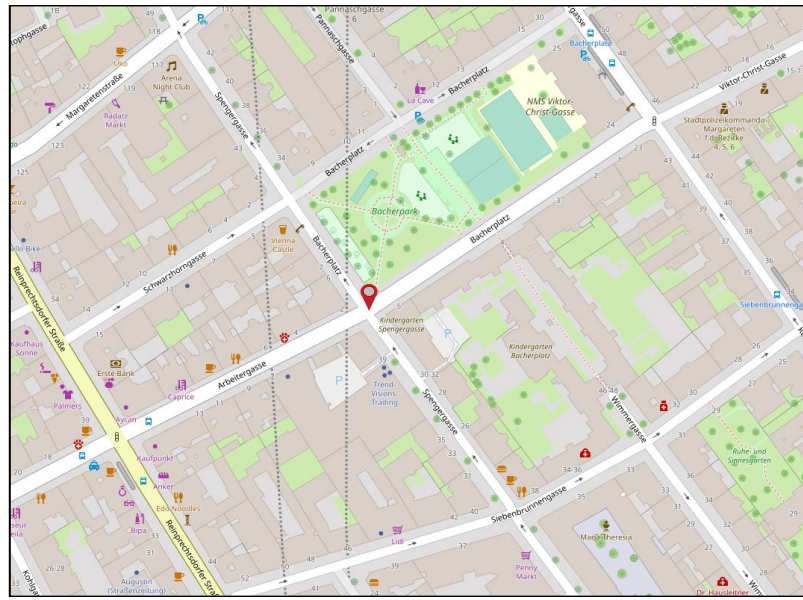
1. UMa - an urban environment with base station antenna height $h_{\text{BS}} = 25 \text{ m}$,
2. UMi street canyon - an urban environment with base station antenna height $h_{\text{BS}} = 10 \text{ m}$,
3. rural macro cell (RMa) - an rural environment with base station antenna height $h_{\text{BS}} = 35 \text{ m}$.

The implementation of the 3GPP 3D model from the Vienna LTE-A system-level simulator [63, 106] is considered, enhanced with the proposed model for spatial consistency as described in Section 4.3.3. For each of the three scenarios, a single antenna with an omni-directional pattern at both transmitter and receiver is assumed. Similarly as in the previous section, simulations comprising a single base station and a user trace with spatial positions following a straight line on the horizontal plane are carried out. A total of 300 realizations for each scenario are conducted, varying the base station and user trace positions in each realization.

Ray-tracing

Following the approach described in Section 5.1, extensive ray-tracing simulations are carried out. Individual environments are created, representing a similar geometry as the ones considered in 3GPP UMa, UMi and RMa scenarios. To make the simulations even more realistic, the data for the selected areas are taken directly from OpenStreetMap [101]. These data are then reproduced in 3D using the SketchUp tool. Since the data from OpenStreetMap provides the geometry information only in 2D (mostly), the building height information is added afterwards based on the details from 3GPP 3D channel model [43, 72], as already discussed in Section 5.1. In this way, for urban scenarios, parts of European cities such as Vienna, Rome and Budapest are considered. One example is depicted in Fig. 5.7, illustrating a part of the city of Vienna and the corresponding model in 3D utilized in ray-tracing simulations. For the rural scenario, regions in the neighbourhood of Krems in Austria and Padova in Italy are employed.

Similarly as in the 3GPP 3D model case, a single base station and a straight user trace are assumed with various locations in each realization. For each of the two urban scenarios, UMa and UMi, a total of 70 realizations (with different locations of base station and user trace as well as surrounding geometry, i.e., different streets) are simulated. In the rural scenario case where the size of the scenario is larger, approximately $2 \text{ km} \times 3 \text{ km}$, ray-tracing simulations become very extensive, at best 20 realizations are carried out. A carrier frequency of 2 GHz is considered for both ray-tracing and 3GPP 3D channel model simulations. All three propagation mechanisms are assumed: reflection, scattering and diffraction. Since the aim is to analyze the spatial consistency of multipath components, the direct path in the case of LOS is excluded from the analysis.



(a) 2D view from OpenStreetMap



(b) Modeling in 3D with SketchUP

Figure 5.7.: Example of a neighborhood in the city of Vienna taken from OpenStreetMap [101]. The same scenario is reconstructed in 3D using the SketchUP tool [104]. The size of the reconstructed scenario is 400 m × 450 m.

Results for Correlation Coefficient

Based on Eq. (5.1), the correlation coefficient for AoA and EoA is evaluated. For each of the scenarios, UMa, UMi and RMa, the LOS and NLOS propagation is investigated separately. For the UMa scenario, a trace length of 150 m is considered with a distance of 1 m between consecutive snapshots. The simulation results of averaged correlation coefficient are shown in Fig. 5.8. The results reveal first, that there are differences in correlation between AoA and EoA, and in general a higher correlation is observed in elevation compared to azimuth. This stems from the fact that angles in elevation are more confined in space, which is also reflected in a smaller angular spread². The same is true for ray-tracing and 3GPP 3D model with spatial consistency and a good agreement between the two cases is observed. As expected, increasing Δd in the proposed model, yields a higher correlation, whereas the correlation is always zero in the case of 3GPP 3D model without spatial correlation. Furthermore, differences between LOS and NLOS are noticed, captured by both 3GPP 3D model and ray-tracing statistics.

The results in terms of correlation coefficients for the UMi scenario are shown in Fig. 5.9, considering a trace length of 100 m. Similarly as in the UMa case, a good agreement is observed between the proposed model for spatial consistency and ray-tracing. Only for the AoA angle in LOS, a higher correlation is revealed by ray-tracing statistics when compared to my model. When looking at the spatial consistency model, it is observed that even for very high values of Δd the increase in correlation is not that noticeable. One would have to apply very-large values of Δd in order to introduce a higher correlation matching the one from ray-tracing statistics, but a Δd on the range of kilometers is not realistic for system-level simulations. On the other hand, this behaviour of the 3GPP 3D channel model when applying large values of Δd , reflects the statistics of the overall channel model, including here the correlated LSPs where in particular the azimuth angles in LOS follow a smaller correlation over distance (see [43][Tab. 7.5-6 Part-1]).

The results for the RMa scenario, employing a trace length of 150 m, are given in Fig. 5.10. As expected, a very high correlation is observed in the statistics from ray-tracing. This is due to the fact that the number of scatterers is very small in rural environments compared to urban, and multipath components change very slowly over distance. Furthermore, the distances to the base station (BS) are in the range of 0.2 – 3 km, in accordance with the 3GPP description which specifies an inter-site distance of 5 km. Such large distances, imply a smaller variation on the elevation angle, where the EoA becomes very close to the LOS angle. On the other hand, the results indicate that higher de-correlation values need to be applied in the model for spatial consistency in order to reflect this behaviour.

²See Fig. B.1 denoting elevation angular spreads for the 3GPP TR 36873 channel model.

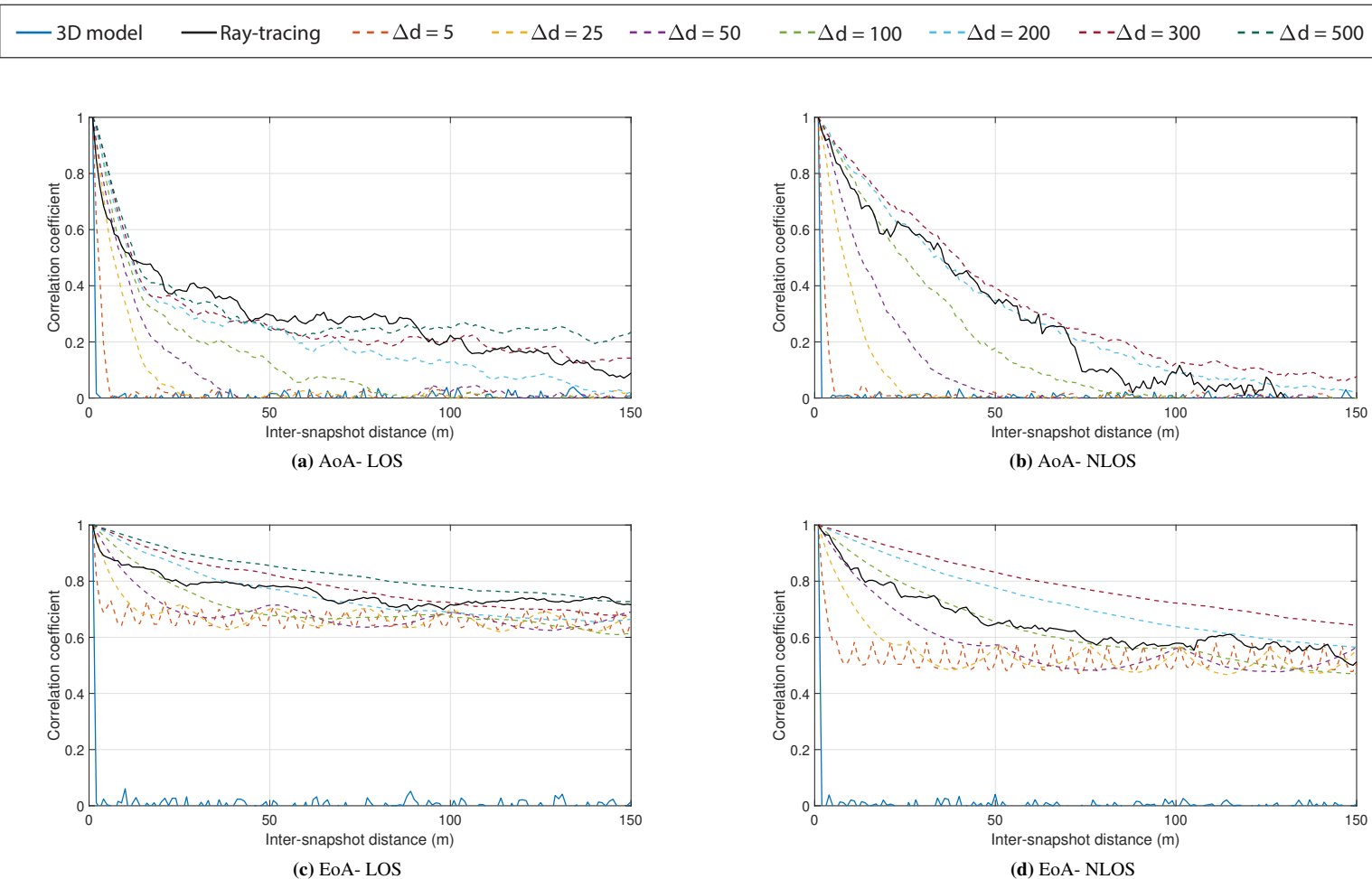


Figure 5.8.: Correlation coefficient of the 3GPP UMa scenario, considering the spatial consistency model with different values of de-correlation distance Δd and results from ray-tracing.

5.3. Statistical Evaluation of Spatially Correlated SSP Model

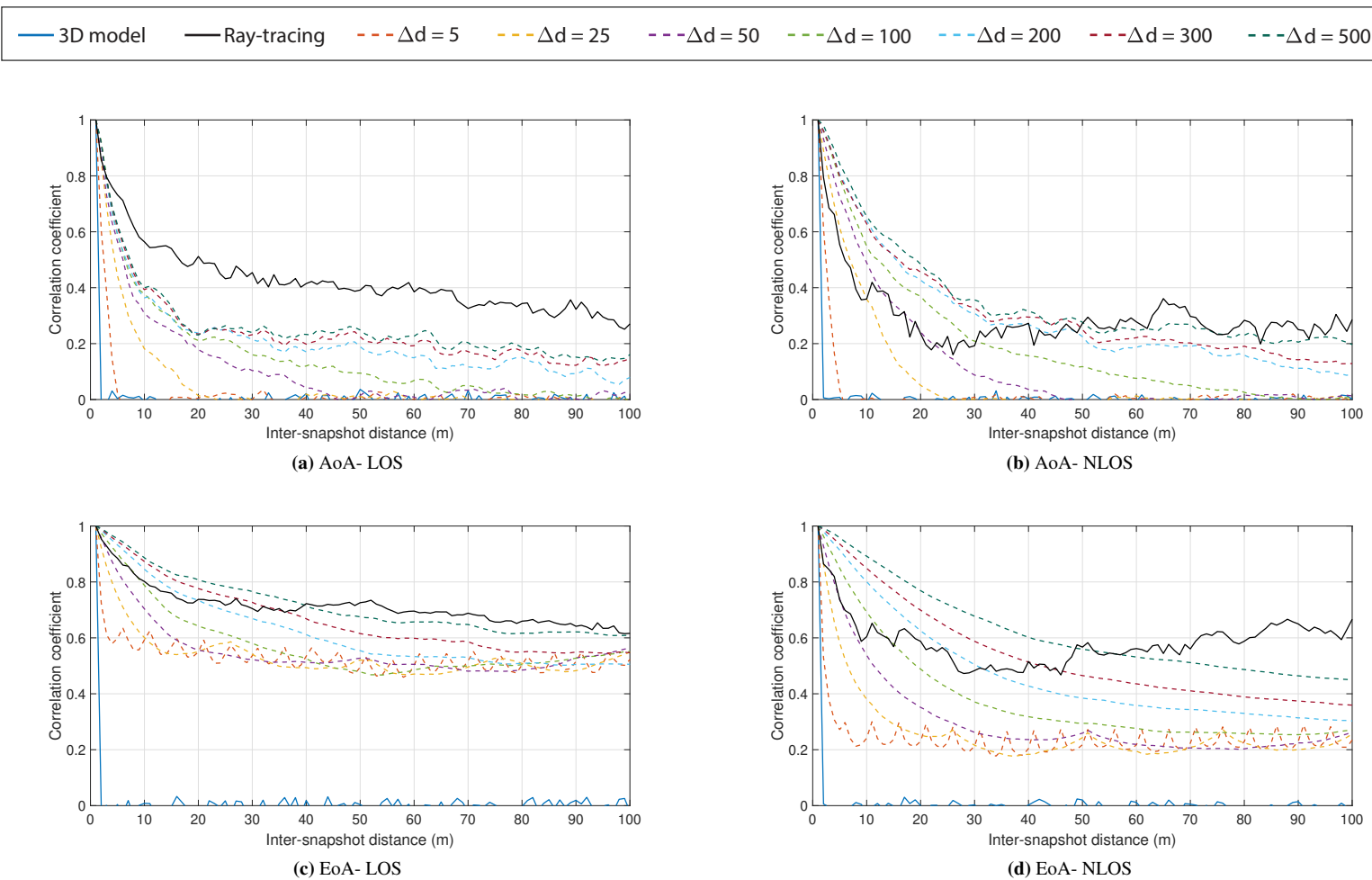


Figure 5.9: Correlation coefficient of the 3GPP UMi scenario, considering the spatial consistency model with different values of de-correlation distance Δd and results from ray-tracing.

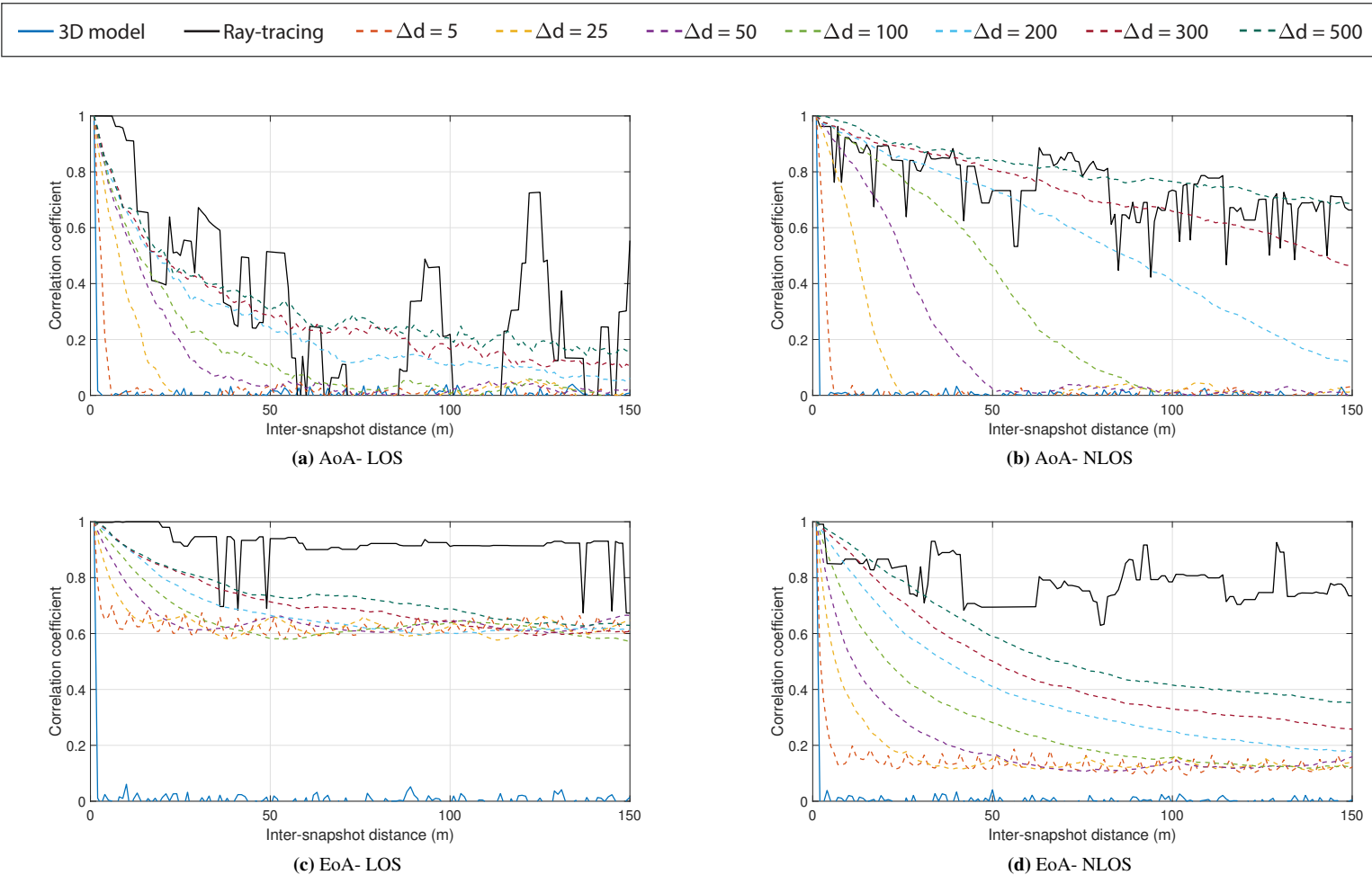


Figure 5.10.: Correlation coefficient of the 3GPP RMa scenario, considering the spatial consistency model with different values of de-correlation distance Δd and results from ray-tracing.

5.4. Model Parametrization

In this section, following the obtained ray-tracing statistics presented in the previous section, hypothesis testing is employed in order to parametrize the proposed spatial consistency model. For this parametrization, the 3GPP channel model statistics with three different scenarios [43, 72] under both LOS and NLOS propagation conditions are considered.

5.4.1. Hypothesis Testing

In order to find the corresponding value of de-correlation distance, Δd , such that the evaluated correlation is closest to the correlation revealed from ray-tracing statistics, binary hypothesis testing is employed. For a comparison between the correlation coefficients of the proposed model for various values of Δd , denoted by $\rho^{(3D)}$, with that of ray tracing denoted as $\rho^{(RT)}$, the binary hypothesis problem is mathematically defined as,

$$\mathcal{H}_{0,c} : \rho_{k,c}^{(3D)} = \rho_k^{(RT)} \quad \mathcal{H}_{1,c} : \rho_{k,c}^{(3D)} \neq \rho_k^{(RT)}. \quad (5.4)$$

Subscript k denotes the corresponding receiver spatial position or snapshot along a trace as explained in the previous section, whereas subscript c denotes the actual Δd applied to the 3GPP 3D channel model.

In order to compare the sample correlation coefficients, first Fisher's z-transformation [2] is applied,

$$\text{FT}(\rho_{k,c}^{(3D)}) = \frac{1}{2} \ln \left(\frac{1 + \rho_{k,c}^{(3D)}}{1 - \rho_{k,c}^{(3D)}} \right) \quad (5.5)$$

and

$$\text{FT}(\rho_k^{(RT)}) = \frac{1}{2} \ln \left(\frac{1 + \rho_k^{(RT)}}{1 - \rho_k^{(RT)}} \right) \quad (5.6)$$

where $\text{FT}(\cdot)$ is the approximate variance-stabilizing transformation which transforms the respective $\rho_{k,c}^{(3D)}$ and $\rho_k^{(RT)}$ to z-scores,

$$z_{k,c} = \frac{\text{FT}(\rho_{k,c}^{(3D)}) - \text{FT}(\rho_k^{(RT)})}{\sqrt{\frac{1}{n^{(3D)}-3} + \frac{1}{n^{(RT)}-3}}} \quad (5.7)$$

with $n^{(3D)}$ and $n^{(RT)}$ being sample sizes of respective models. Because the correlation coefficient is bounded, its distribution for highly correlated variables or barely correlated ones is strongly skewed. Therefore, Fisher's z-transformation transforms a skewed distribution into a normal distribution. This transformation ensures to select the de-correlation distance $\rho_{k,c}^{(3D)}$ from the 3GPP 3D model

which gives the most similar correlation to that of ray tracing statistics $\rho_k^{(\text{RT})}$, while being sensitive to both variance and mean in detecting similarities/changes. In this way, based on rejection rates of hypotheses, the parameter under investigation, Δd , can be parametrized.

The evaluation of similarity between $\rho_{k,c}^{(3D)}$ and $\rho_k^{(\text{RT})}$ is based on p-values, while the rejection rate is performed based on a significance level $\alpha = 0.05$. The rejection rates for each Δd denoted with c , can be expressed as,

$$R_c = \frac{\mathbb{P}(\text{reject } \mathcal{H}_{0,c} | \rho_{k,c})}{\mathbb{P}(\text{accept } \mathcal{H}_{0,c} | \rho_{k,c}) + \mathbb{P}(\text{reject } \mathcal{H}_{0,c} | \rho_{k,c})}. \quad (5.8)$$

Finally, according to the lowest rejection rate,

$$\Delta d \doteq \operatorname{argmin}_c R_c, \quad (5.9)$$

the actual Δd is determined.

5.4.2. Results

The parametrization model considering hypothesis testing explained above is applied on the statistical data from simulations as conferred in Section 5.3.2. For the 3GPP 3D model with spatial correlation model, a large range of values for de-correlation distance is selected, $\Delta d = \{5, 10, 15, \dots, 500\}$. From Eq. (5.7) and Eq. (5.8), the length of the trace considered for both the 3GPP 3D model and ray-tracing is important and affects the rejection rates. Therefore, it is important to select a length that is meaningful with respect to the scenario, i.e., for the UMi case where the inter-base station distance is no larger than 200 m according to 3GPP, a trace length is selecting to be 50 m for NLOS and 40 m for LOS, meaning that ρ_k is considered for $k = 1, 2, \dots, 50$ and $k = 1, 2, \dots, 40$, respectively. In this way, by focusing on the correlation properties in shorter-range distances, the accuracy of parametrization is increased and the Δd values that are closest to the observed ray-tracing behaviour are obtained. For the UMa scenario, $k = 1, 2, \dots, 100$ for NLOS and $k = 1, 2, \dots, 50$ for LOS is applied. For the RMa case, $k = 1, 2, \dots, 150$ is considered for both LOS and NLOS. The derived rejection rates for a selected range of Δd values are given in Table 5.2. It is observed that for the UMa and UMi scenario, the rejection rates go as low as around 0.01-0.1, meaning that statistics are matching with a very high confidence. In the RMa scenario, results reveal higher rejection rates, in particular for the elevation case, reflecting the difference between the very high correlation in ray-tracing statistics and the correlation of the 3GPP 3D channel model.

Following Eq. (5.9), Δd values with lowest rejection rates are presented in Table 5.3. In most of the scenarios, there is more than one value of Δd that give the lowest rejection rates, therefore applying any value from the given range is statistically valid. The proposed model for spatial consistency with the values presented in Table 5.3 is applicable to the 3GPP TR36873 and TR38901 channel models with scenarios such as UMa, UMi and RMa.

5.4. Model Parametrization

Table 5.2.: Rejection rates for different de-correlation distances for AoA and EoA in LOS and NLOS considering three 3GPP scenarios of UMa, UMi and RMa.

	UMa				UMi				RMa			
	Δd	R_{LOS}	Δd	R_{NLOS}	Δd	R_{LOS}	Δd	R_{NLOS}	Δd	R_{LOS}	Δd	R_{NLOS}
AoA	5	1.00	5	0.56	5	1.00	5	0.35	5	0.64	5	1.00
	25	0.88	25	0.54	50	0.57	10	0.17	50	0.62	50	0.98
	50	0.68	50	0.44	100	0.12	15	0.12	125	0.58	100	0.91
	75	0.38	75	0.12	150	0.07	20	0.02	175	0.55	150	0.81
	80	0.24	80	0.02	175	0.05	25	0.05	225	0.52	200	0.67
	85	0.08	85	0.01	200	0.02	30	0.07	250	0.51	250	0.58
	90	0.08	90	0.01	250	0.02	50	0.07	275	0.61	300	0.55
	95	0.08	95	0.01	300	0.02	65	0.15	300	0.62	325	0.56
	100	0.08	100	0.01	350	0.02	100	0.15	350	0.57	350	0.50
	105	0.10	105	0.03	425	0.02	150	0.20	400	0.56	400	0.50
	125	0.10	125	0.04	450	0.05	300	0.25	500	0.60	500	0.50
EoA	5	0.76	5	0.35	5	0.40	5	0.67	10	0.98	10	1.00
	25	0.60	25	0.33	25	0.42	20	0.52	100	0.97	100	0.98
	50	0.38	30	0.15	75	0.05	40	0.15	125	0.94	150	0.98
	75	0.14	40	0.02	80	0.02	45	0.07	150	0.94	200	0.97
	80	0.12	45	0.01	100	0.02	50	0.02	150	0.94	250	0.94
	85	0.12	50	0.01	125	0.05	55	0.05	250	0.94	300	0.92
	90	0.14	70	0.01	250	0.10	100	0.07	325	0.94	350	0.91
	95	0.14	95	0.01	350	0.20	150	0.22	350	0.95	375	0.90
	100	0.14	100	0.01	450	0.22	200	0.25	400	0.95	400	0.89
	125	0.20	125	0.11	100	0.20	300	0.37	500	0.96	500	0.84

Table 5.3.: Values of de-correlation distances (Δd) based on lowest rejection rates.

Δd	UMa		UMi		RMa	
	LOS	NLOS	LOS	NLOS	LOS	NLOS
Random variables for azimuth	85 – 100	85 – 100	200 – 425	20	250	350 – 500
Random variables for elevation	80 – 85	45 – 100	80 – 100	50	125 – 325	500

5.5. Complementary Aspects

In this section, complementary aspects of spatial consistency model are investigated such as the behaviour of the model in higher frequencies and a more detailed view on implementation and computational complexity.

5.5.1. Computational Complexity

In Section 3.3, the computational complexity of the geometry-based stochastic channel model is discussed, considering the 3GPP 3D channel model implementation from [63, 69]. The aim of this section is to show the additional complexity, in terms of simulation run time, induced when applying the proposed spatial consistency model. Again the 3GPP 3D model with parameters as specified in [72] and implementation from [69, 106] is considered. All simulations are carried out on the same hardware, an Intel(R) Core(TM) i7-3930K CPU@3.20 GHz, equipped with 64 GB of RAM.

The UMa scenario comprising of a single base station and a user trace with K snapshots is considered, where the channel impulse response is calculated for each snapshot. Both transmitter and receiver have single omni-directional antennas. The number of snapshots for channel calculation is varied by choosing $K = \{50, 100, 200, 300, 400, 500\}$ snapshots. The simulation results in terms of run time measured in seconds are provided in Fig. 5.11. The results reveal that the runtime scales approximately linearly with the number of snapshots K for the reason that the channel impulse response is generated for each snapshot location. A slight increase in terms of simulation runtime is observed when introducing the spatial consistency model compared to the case without spatial consistency. This is caused by the fact that, in the spatial consistency model, the bilinear interpolation needs to be performed for each snapshot location. From the results, this increase turns out to be around 4% when $K = 50$ and rising up to 16% for $K = 500$. Furthermore, it is observed that the value of de-correlation distance Δd in the proposed spatial consistency model does not impact the simulation run time, as indicated in Fig. 5.11. This stems from the fact that for the same number of snapshots, when applying a higher value of Δd , it only generates less random variables, however the same amount of computations is performed in order to get the correlated random variables for every user location or snapshot.

Most importantly, the proposed model for spatial consistency enables to parallelize the SSP generation over spatial positions or user locations, and thus allows to further enhance the computational efficiency of 5G system level tools such as the one in [87].

Compared to the computational complexity the 3D geometry-based stochastic channel, the simulation time in ray-tracing is very high. From the conducted simulations in this chapter, done with the same hardware, the simulation time is around 60 minutes per single snapshot, that leads to 3000 minutes for $K = 50$ snapshots. In the ray-tracing, the simulation time depends explicitly on the size of the

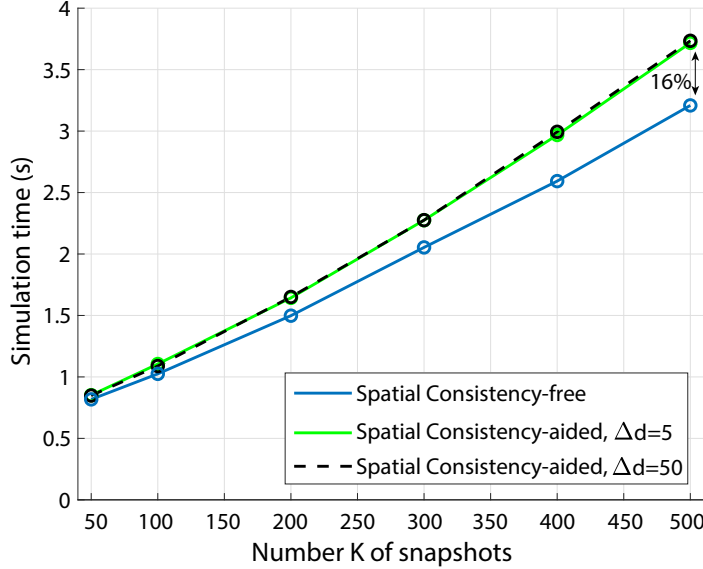


Figure 5.11.: Simulation run time of 3GPP TR38901 channel model with and without spatial consistency over number of snapshots K .

scenario in 3D and on the expansion of propagation mechanisms applied, i.e., reflections, diffractions and scattering.

5.5.2. Correlation of Angular Sign

As briefly discussed in Section 4.1, among those random variables that need to be correlated is also the angular sign, a variable that introduces a positive or negative sign to the angular direction of each multipath component. In the spatial consistency model from 3GPP from [72][Sec. 7.6.3.1], it is specified that this parameter, referred to as cluster specific sign, should be kept unchanged per simulation drop even if the user position changes during simulation. This means, if the AoA³ for the first five clusters is e.g., $\{-20^\circ, 85^\circ, -130^\circ, 50^\circ, 165^\circ\}$, after the user location is updated, the AoA for the first five clusters will be $\{-25^\circ, 80^\circ, -125^\circ, 55^\circ, 160^\circ\}$, assuming here a variation of $\pm 5^\circ$ for the purpose of an easier explanation. In this way, the first five clusters are always coming from similar directions while the absolute value of the angle will change in accordance with the de-correlation distance. Referring to the stepwise procedure of SSPs generation, Eq. (5.11) in *Step 7*, indicating the AoA correlation,

$$\phi_{n,\text{AoA}} = \tilde{r}_n(x, y)\phi'_{n,\text{AoA}} + \tilde{s}_n(x, y) + \phi_{\text{LOS},\text{AoA}}, \quad (5.10)$$

³The AoA $\in [-180^\circ, 180^\circ]$.

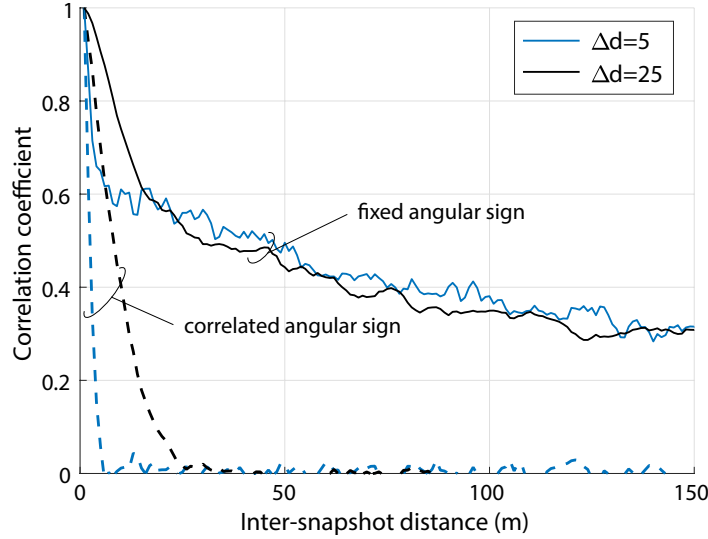


Figure 5.12.: Comparison of correlation coefficient for AoA when fixing the angular sign for a moving user.

according to [72] it becomes

$$\phi_{n,\text{AoA}} = \tilde{r}_n(x, y) \phi'_{n,\text{AoA}} + S_n + \phi_{\text{LOS},\text{AoA}}, \quad (5.11)$$

with $S_n \sim \mathcal{U}(0, \sigma_{ASA})$ denoting the cluster specific sign, which is generated at the beginning of each simulation and kept unchanged. The variable σ_{ASA} represents the angular spread for the azimuth angle.

After employing this approach into the proposed model for spatial consistency, a very high correlation is observed in terms of AoA for consecutive spatial locations (i.e., a user that is moving and thus its position changes during one simulation). Figure 5.12 shows this behaviour compared to the spatial consistency model as presented in Section 4.3, where the angular sign is correlated (interpolated) and updated over spatial positions depending on the value of de-correlation distance. Therefore, fixing any random parameter during one simulation regardless of the user changing its location, is also not a realistic assumption and will lead to the other extreme of introducing a very high correlation. Furthermore, as shown from the results in Section 5.3, when considering one specific urban environment with ray-tracing, abrupt changes of arrival angles occur, are realistic and reflect the changes in geometry of surrounding objects along the propagation path.

5.5.3. Frequency Impact on Spatial Correlation

In order to examine the impact of carrier frequency on spatial correlation, simulations with ray-tracing considering two carrier frequencies: 2 GHz, 28 GHz are conducted. Figure 5.13 shows the results

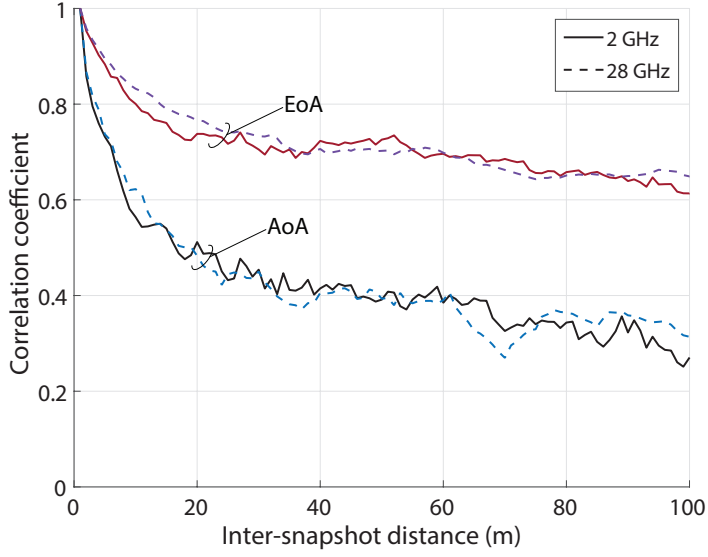


Figure 5.13.: Correlation coefficient of AoA and EoA for 2 GHz and 28 GHz from ray-tracing simulations.

in term of correlation coefficient for the UMi scenario in LOS for both AoA and EoA. Under an omni-directional antenna at both receiver and transmitter, there are no significant differences in the correlation when changing the carrier frequency. This is in agreement with findings from [65], where no changes in correlation were found between 2 GHz and 28 GHz and that the same value of de-correlation distances as the ones for 2 GHz apply for higher frequencies as well.

5.6. Summary

In this chapter, to have a better understanding on spatial consistency, ray-tracing simulations are carried out following real environments imported from OpenStreetMap. When analysing characteristics of strongest multipath components over consecutive spatial positions, a good agreement between ray tracing and the proposed spatial consistency model is observed. The spatial consistency model reveals similar characteristics with ray-tracing, in terms of spatial correlation, and is capable to mimic the appearance of new scatterers and disappearance of old ones.

Nevertheless, to allow parametrization of a stochastic model, it is necessary to simulate many ray-tracing scenarios that share certain characteristics (i.e., building density, building heights, street widths) and obtain statistical measures. Considering the obtained statistics from ray-tracing and applying binary hypothesis testing, the spatial consistency model is validated. Following a very good agreement with ray-tracing statistics, the model is parametrized for urban, urban street canyon and rural scenarios considering LOS and NLOS propagation conditions separately.

The chapter is completed by demonstrating that the proposed spatial consistency model is applicable also for higher frequency ranges as for example to the 3GPP channel model for millimeter-wave (mm-Wave) [72]. Additionally, the impact of the proposed spatial consistency model on the simulation complexity is investigated revealing only a small increase in simulation run time compared to the case without spatial consistency. Furthermore, the proposed model enables to parallelize the SSP generation over spatial positions or user locations, and thus allows to further enhance the computational efficiency of 5G system level tools.

An important aspect in the future, is to also support spatial consistency for device-to-device (D2D) scenarios in which both transmitter and receiver are in movement. I am confident that my model for spatial consistency is applicable also for D2D scenarios. In this context, an evaluation similar to the one presented in this work is necessary to extract the corresponding values of de-correlation distance that would reflect the realistic behaviour of D2D.

6

Conclusions

The integration of a 3-dimensional (3D) channel model into existing link- and system-level simulation tools paves the way for more advanced studies on the performance of a mobile cellular system in realistic environments. Existing channel models only support linear antenna arrays in the azimuth. With the introduction of the third dimension, not only higher-order multiple-input multiple-output (MIMO) schemes, but also a higher number of antenna elements per antenna array can be investigated. The number of antenna elements packed in an antenna array is expected to be increased in the coming years. A main enabler for this so called massive MIMO approach will be the adoption of higher carrier frequencies, also termed millimeter-wave (mm-Wave) communication, as it enables to considerably decrease the size of the antenna arrays.

With the additional elevation information carried for each path's propagation property, channel models become more complex and this demands a careful design for systematic performance evaluation. Furthermore, with the previous state of the art channel models common for system-level tools, such as power delay profile (PDP)-based channels, Rayleigh or Rician fading, there is no interaction and no dependency of the channel generation with the geometry (i.e., location of users and base stations (BSs)). Such channels are only time-variant, thus allowing for pregeneration of channel coefficients for a certain duration in time. With the 3D geometry-based stochastic channel model, the channel impulse response is both position- and time-dependent, therefore the channel has to be calculated at runtime.

The main contributions of this thesis are modeling of spatial consistency for 3D geometry-based stochastic channel models and a practical design for system-level tools with a novel spatial granularity structure for supporting 3D channel models. The following section summarizes the main contributions of this thesis.

6.1. Summary of Contributions

The first part of the thesis introduces modeling of the 3D geometry-based stochastic channel model in system-level tools.

Chapter 3 presents a detailed guideline for practical implementation of the 3rd Generation Partnership Project (3GPP) 3D channel model into an existing system-level simulation tool. Facing the challenge of calculating the channel impulse response at simulation runtime, a model for partitioning the generation of the channel in several steps is introduced. A new time line structure for system-level tools is proposed that considers the spatio-temporal structure of the geometry-based stochastic channel model. It starts with the smallest resolution in time domain, that is the subframe level, referred to as time slot, continuing with segments that represent quasi-stationary regions denoting a larger time span during which large-scale parameters stay approximately constant, and chunks representing larger spatial regions where spatial correlation properties are preserved. Such structure simplifies the overall generation of the channel impulse response, while preserving the spatio-temporal characteristics of the channel model. The validity of this modeling approach is demonstrated by integrating it into the Vienna LTE-Advanced (LTE-A) Downlink System-Level Simulator, and recently in the novel Vienna fifth generation (5G) System-Level Simulator.

The complexity increase of system-level simulations when considering the geometry-based stochastic channel model and planar antenna arrays consisting of a large number of antenna elements is investigated. Analysis in terms of simulation run time show an approximately linear increase in simulation complexity with the number of antenna elements per antenna array. In the last part of this chapter, a systematic procedure to evaluate spatial resolution of large 2-dimensional (2D) antenna arrays is introduced. In particular, the impact of considering a realistic channel model when introducing sharp beams focused on specific locations in the cell is investigated. The results reveal that different channel conditions impact the spatial resolution in a distinct manner. While there exists an increase in received channel energy when increasing the beam spatial resolution in elevation, this increase is not proportional with respect to the increase in the number of antenna elements. Therefore, the difference between 10 and 100 antenna elements is by far not as distinct as one might expect. Nevertheless, the larger number of antenna elements still has the advantage of a much better spatial resolution.

The second major part of this thesis is devoted to spatial consistency modeling. In Chapter 4, a novel approach for achieving spatially consistent geometry-based stochastic channel models is presented, consisting of two models. The first model introduces spatial correlation among neighbouring user locations for line of sight (LOS)/non line of sight (NLOS) propagation condition and Indoor/Outdoor state. In a further investigation, it is observed that the model captures similar behaviour as in the case when considering an explicit modeling of blockages in 3D. The second model introduces spatial consistency to small-scale fading enabling thus system-level investigations of scenarios with user mobility, massive MIMO and multi-user schemes, beamforming etc. The principle of the model is

to correlate all random variables based on a distance-dependency, represented by the de-correlation distance parameter. The model allows a pre-generation step of all random variables that are correlated by employing bilinear interpolation. These correlated random variables, are then applied in the small-scale parameters (SSPs) step-wise generation. Analysing the statistical properties of the model, it is shown that second-order sum of sinusoids is a good approximation of the correlation function that the proposed model achieves.

In Chapter 5, characteristics of strongest multipath components over consecutive spatial positions are analysed considering ray-tracing simulations. Real environments based on the data from Open-StreetMap are considered for ray-tracing simulations. The proposed spatial consistency model from Chapter 4 reveals similar behaviour, in terms of spatial correlation, with the one obtained from ray-tracing, and is capable to mimic the appearance of new scatterers and disappearance of old ones. Further, a statistical validation and parametrization of the spatial consistency model is presented, based on statistical measures obtained with a large set of ray-tracing simulation realizations. The model is parametrized for urban, urban street canyon and rural scenarios considering LOS and NLOS propagation conditions.

The thesis is completed by demonstrating that the proposed spatial consistency model is applicable also for higher frequency ranges as for example to the 3GPP channel model for mm-Wave [72]. Additionally, the impact of the proposed spatial consistency model on the simulation complexity is investigated revealing only a small increase in simulation run time compared to the case without spatial consistency.

6.2. Open Issues and Outlook

Although this thesis introduces a modeling of spatial consistency for 3D channel models and considers a system-level modeling of such channel models, still not all possible aspects are included.

The spatial consistency model for LOS/NLOS and Indoor/Outdoor propagation conditions shows a realistic behavior when compared to propagation conditions extracted by modeling the blockages explicitly. One aspect that is not treated in this part is modeling of the channel transition from one propagation condition to the other. When a user is moving, changing the propagation state i.e., from LOS to NLOS or Indoor to Outdoor, will cause a hard transition in the channel parameters. While for the LOS, the channel parametrization (parameters for large-scale parameter (LSP) and SSP generation) is different compared to the NLOS, a transition phase from i.e., LOS to NLOS is necessary in order to retain spatial consistency. In the contrary, the update of channel parameters will lead to an uncorrelated behavior. This issue is already addressed in the recent 3GPP TR38901, where the hard transitions between LOS and NLOS are modeled by means of a linear combination between LOS and NLOS. Whereas, the transition from Indoor to Outdoor state is not yet addressed and needs further investigation and modeling.

Another issue that is not sufficiently researched yet, is the investigation of spatial consistency for device-to-device (D2D) scenarios and in particular the vehicle-to-vehicle (V2V) case. The necessity to include a 3D geometry-based stochastic channel model in further analysis and evaluations of such mobile scenarios is becoming crucial with the introduction of mm-Wave. Being headed towards 5G of mobile communications, further investigations have to be directed towards enhancing 3D channel models and spatial consistency for V2V scenarios.

6.3. Conclusion

The presented framework and modeling in this dissertation resolves challenging issues related with the utilization of 3D geometry-based stochastic channel models on system-level tools. The proposed models and spatial granularity design for system-level tools paves the way for more advanced studies on the performance of a mobile cellular system in realistic environments. It enables analysing massive MIMO, 3D beamforming and beamtracking strategies, mm-Wave scenarios as well as vehicular use case scenarios. The proposed model is openly available as a stand-alone package and also part of the Vienna Cellular Communication Simulators. Believing that open access is a key prerequisite for reproducible simulation studies, I hope to inspire researches and developers of system-level simulation tools to further elaborate on these topics by directly applying or reusing my implementation approach and continue promoting the open access.

A

List of Abbreviations

2D	2-dimensional
3D	3-dimensional
3GPP	3rd Generation Partnership Project
4G	fourth generation
5G	fifth generation
AF	array factor
AMC	adaptive modulation and coding
AWGN	additive white Gaussian noise
AoA	azimuth of arrival
BICM	bit-interleaved coded modulation
BLER	block-error ratio
BS	base station
CDF	cumulative distribution function
D2D	device-to-device
ECDF	empirical cumulative distribution function
ESCM	extended-SCM
EoA	elevation of arrival
FBMC	Filter-bank multicarrier
FD	full dimension
FFT	Fast Fourier Transform
GSCM	geometry-based stochastic channel model
i.i.d.	independent and identically distributed
IMT	International Mobile Telecommunications

Appendix A. List of Abbreviations

ITU	International Telecommunications Union
ITU-R	International Telecommunication Union - Radiocommunication Sector
LDPC	low-density parity-check code
LOS	line of sight
LSP	large-scale parameter
LTE	Long Term Evolution
LTE-A	LTE-Advanced
MCS	modulation and coding scheme
MIESM	mutual information effective SINR mapping
MIMO	multiple-input multiple-output
MMSE	minimum mean-squared error
mm-Wave	millimeter-wave
NLOS	non line of sight
NR	new radio
O-to-I	outdoor-to-indoor
OFDM	orthogonal frequency division multiplexing
PDP	power delay profile
PHY	physical
RB	resource block
RMS	root mean square
RMa	rural macro cell
ROI	region of interest
SCM	Spatial Channel Model
SINR	signal to interference- and noise ratio
SSP	small-scale parameter
sTTI	short TTI
TTI	transmission time interval
UMa	urban macro cell
UMi	urban micro cell
V2V	vehicle-to-vehicle
WINNER	Wireless World Initiative New Radio
XPR	cross polarization power ratio
ZF	zero forcing

B

Calibration of the 3GPP 3D Channel Model

For calibration of the 3GPP 3D channel model implementation as presented in Chapter 3, system-level simulations are carried out with the setup as specified in [43, Table 8.2-2] and summarized in Table B.1. Two scenarios, 3D-urban macro cell (UMa) and 3D-urban micro cell (UMi) are investigated. The verification of the 3D channel model behaviour is shown by depicting the statistics of LSPs and SSPs. In particular, the angular spread statistics are observed, applying the *circular angle spread* method, as recommended in [30]. This method is used to evaluate the angular statistics from the angular parameters *a posteriori*, i.e., after generating the channel coefficients for each antenna element pair (*Step 11*). Compared to the case of extracting the angular spreads directly from LSPs (generated in Step 4), this procedure presents a more reliable verification of the channel model implementation, as it also validates SSPs (*Steps 5-11*).

Figure B.1 depicts the obtained statistics for zenith spread of departure- and arrival. In accordance with the results in [44], the distributions show similar characteristics for 3D-UMa and 3D-UMi scenarios. Furthermore, they exhibit a good agreement with results from [43] (dash-dotted curves), which were obtained by averaging over 21 sources as reported in [45]. In Fig. B.2 the calibration results for largest and smallest singular values of the channel are shown, as referred from [43, Table 8.2-2]. The singular values are generated on a resource block (RB) basis at $t = 0$ (i.e., TTI = 1) by considering channel coefficients consisting of small-scale fading only (without path loss and shadowing). The results show a good agreement with the results from [43] (dash-dotted curves), which were obtained by averaging over 21 sources as reported in [45].

Table B.1.: Simulation parameters for calibration as referred from [43].

Parameter	Value
Carrier frequency	2 GHz
LTE bandwidth	10 MHz
Macro-site deployment	Hexagonal grid
Scenarios	3D-UMa, 3D-UMi
BS antenna height (UMa)	25 m
BS antenna height (UMi)	10 m
BS antenna configuration	$N_{Tx} = 4$
User antenna configuration	$N_{Rx} = 2$
Polarized antenna modeling	Model 2 [43]
BS antenna polarization	X-pol (+/- 45°)
User antenna polarization	X-pol (0/ + 90°)
Antenna elements per port	$Q = 10$
Vertical antenna element spacing	0.5λ
Horizontal antenna element spacing	0.5λ
Maximum antenna element gain	8 dBi
User antenna pattern	Isotropic antenna gain
Electrical downtilt	12°
User distribution	Uniform in cell [43, Tab. 6-1]

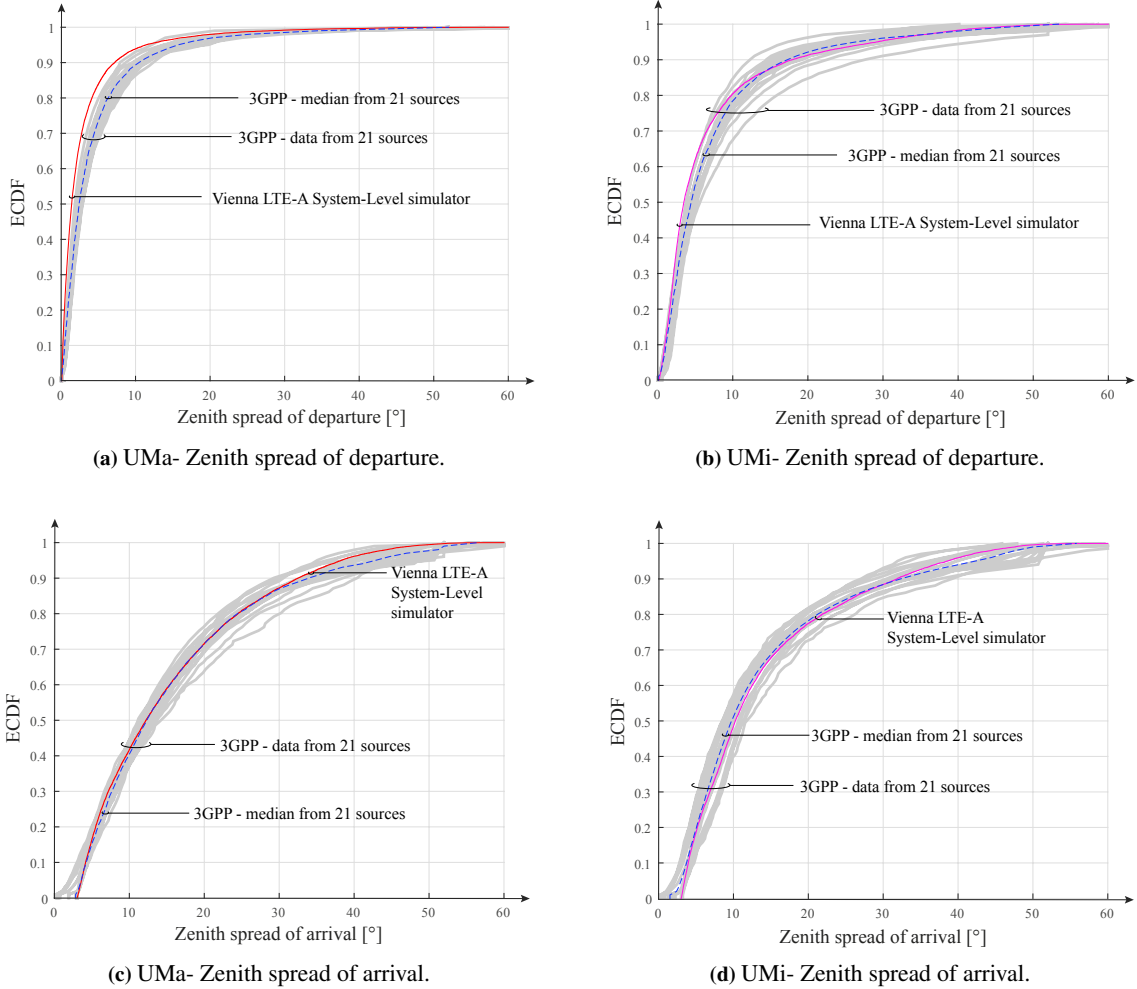


Fig. B.1.: Large-scale parameter statistics. Gray lines refer to results reported by 21 sources from [45]. Dashed curves denote the 3GPP reference results from [43, Figure 8.2-11, Figure 8.2-13].

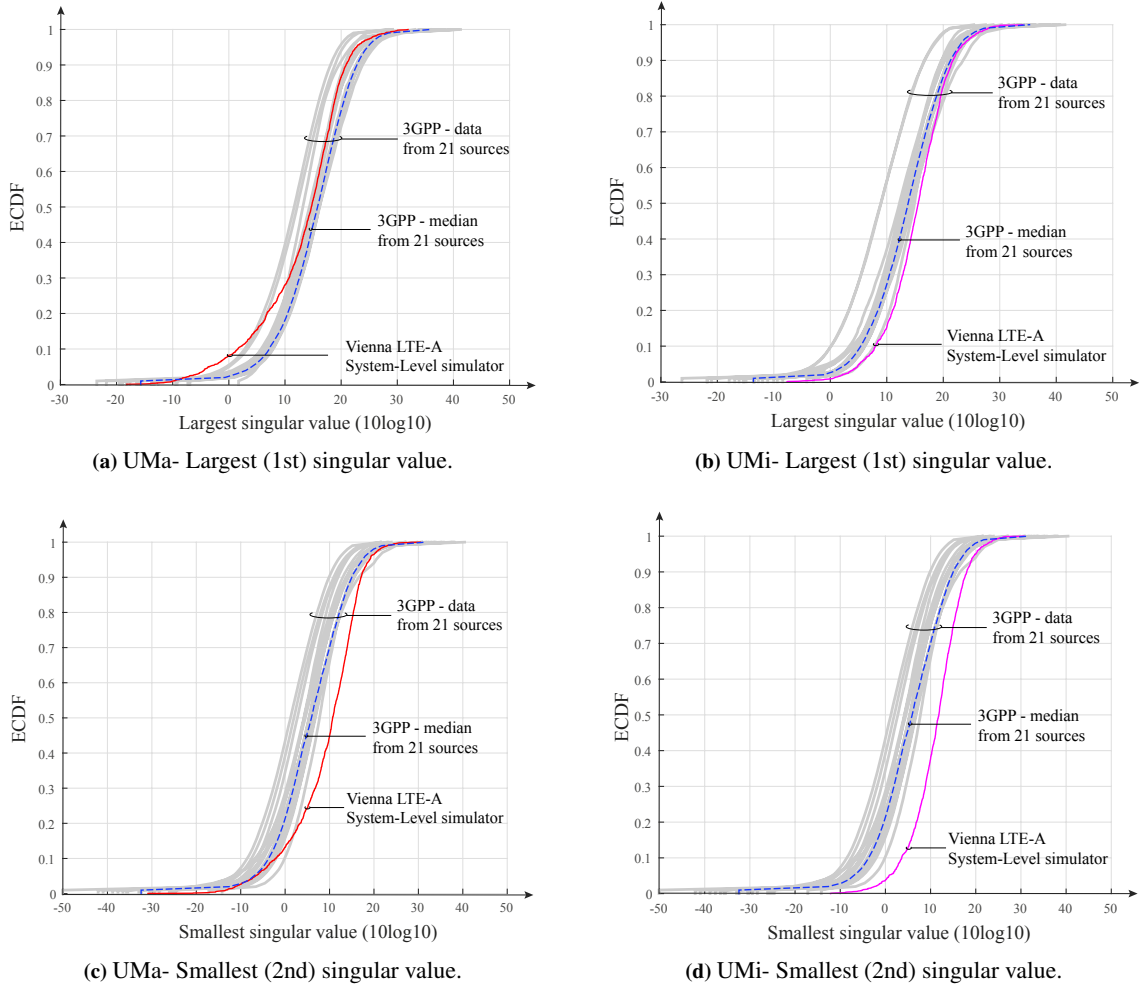


Fig. B.2: Largest and smallest singular value empirical cumulative distribution function (ECDF) in logarithmic scale. Gray lines refer to results reported by 21 sources from [45]. Dashed curves denote the 3GPP reference results from [43, Figure 8.2-17, Figure 8.2-19].

C

Angular Distributions

Referring to the 3GPP 3D channel model, in the SSP generation as elaborated in detail in Chapter 3, the actual angels of arrival and departure are calculated. Considering the UMa scenario and simulation parameters indicated in Table C.1, the probability density functions of angular spreads are observed. The simulation scenario consists of seven three-sectorized BS, each with 100 users uniformly distributed within a cell.

The probability density functions for azimuth angular spreads at the BS (azimuth of departure) and at the user (azimuth of arrival) are illustrated in Fig. C.1. For both cases, as expected, the angular densities follow the inverse Gaussian distribution, as indicated by the solid blue line.

The probability density functions for elevation angular spreads at the BS (elevation of departure) and at the user (elevation of arrival) are depicted in Fig. C.2. For both cases, as expected, the angular densities in elevation follow the Laplacian distribution, as indicated by the solid blue line. Since the elevation angles are confined in the positive angular domain of $[0^\circ, 180^\circ]$, this is also reflected in Fig. C.2, with only the right side of the resembled distribution.

Table C.1.: Simulation parameters.

Parameter	Value
Carrier frequency	6 GHz
LTE bandwidth	20 MHz
Macro-site deployment	Hexagonal grid
Scenarios	3D-UMa
BS antenna height (UMa)	25 m
BS antenna configuration	$N_{Tx} = 4$
User antenna configuration	$N_{Rx} = 2$
Polarized antenna modeling	Model 2 [43]
BS antenna polarization	X-pol (+/- 45°)
User antenna polarization	X-pol (0/+ 90°)
Antenna elements per port	Q = 10
Vertical antenna element spacing	0.5λ
Horizontal antenna element spacing	0.5λ
Maximum antenna element gain	8 dBi
User antenna pattern	Isotropic antenna gain
Electrical downtilt	12°
User distribution	Uniform in cell [43, Tab. 6-1]

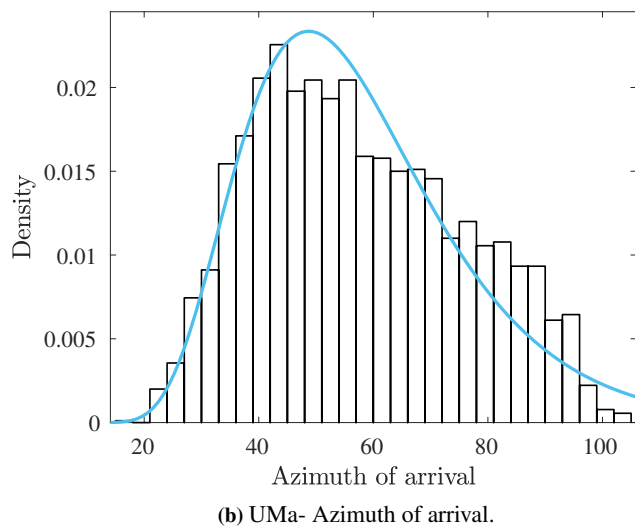
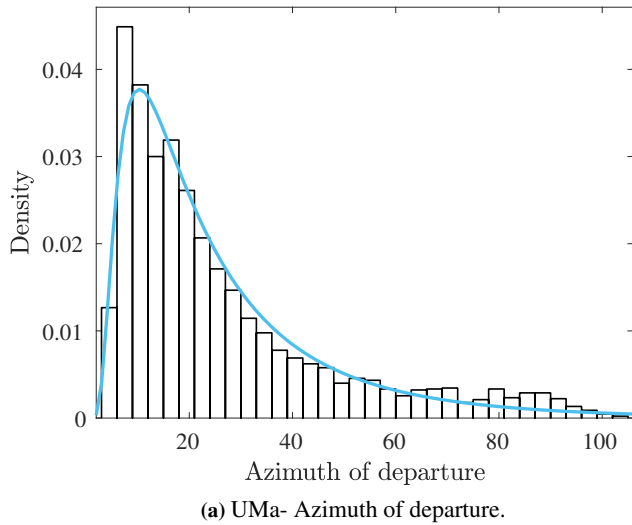


Figure C.1.: Probability distribution of azimuth departure and arrival angles considering the UMa scenario from 3GPP TR38901.

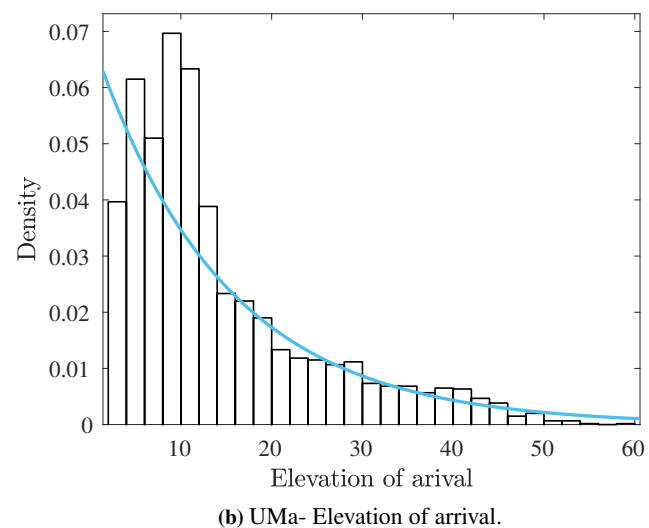
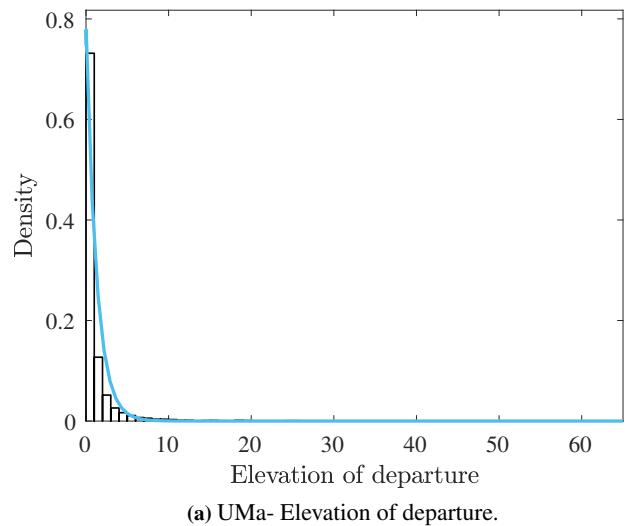


Figure C.2.: Probability distribution of elevation departure and arrival angles considering the UMa scenario from 3GPP TR38901.

Bibliography

- [1] T. Berisha, P. Svoboda, S. Ojak, and C. F. Mecklenbräuker, “SegHyPer: Segmentation- and Hypothesis based Network Performance Evaluation for High Speed Train users”, in *IEEE ICC - International Conference on Communications*, May 2017, Paris, France.
- [2] R. Fisher, “Frequency Distribution of the Values of the Correlation Coefficient in Samples from an Indefinitely Large Population”, *Biometrika*, vol. 10, no. 4, pp. 507–521, May 1915.
- [3] G. H. Spencer and M. V. R. K. Murty, “General ray-tracing procedure”, *Journal of the Optical Society of America*, vol. 52, no. 6, pp. 672–678, 1962.
- [4] N. Fisher and A. J. LEE, “A Correlation Coefficient for Circular Data”, vol. 70, 1983.
- [5] M. Gudmundson, “Correlation model for shadow fading in mobile radio systems”, *Electronics Letters*, vol. 27, no. 23, pp. 2145–2146, 1991.
- [6] J. Andersen, T. Rappaport, and S. Yoshida, “Propagation measurements and models for wireless communications channels”, *IEEE Commun. Mag.*, vol. 33, no. 1, pp. 42–49, 1995.
- [7] M. ITU-R, “Guidelines for evaluation of radio transmission technologies for IMT-2000”, *Report*, 1997.
- [8] L. C. Andrews, *Special Functions of Mathematics for Engineers*, 2nd ed., ser. Oxford Series Publications. SPIE Optical Engineering Press, 1998.
- [9] E. Perahia, D. C. Cox, and S. Ho, “Shadow fading cross correlation between base stations”, in *IEEE VTS 53rd Vehicular Technology Conference, Spring 2001*, vol. 1, May 2001, 313–317 vol.1.
- [10] J. Kermoal, L. Schumacher, K. Pedersen, P. Mogensen, and F. Frederiksen, “A stochastic MIMO radio channel model with experimental validation”, *IEEE Journal on Selected Areas in Communications*, vol. 20, no. 6, pp. 1211–1226, 2002.
- [11] J. Weitzen and T. J. Lowe, “Measurement of angular and distance correlation properties of log-normal shadowing at 1900 MHz and its application to design of PCS systems”, *IEEE Transactions on Vehicular Technology*, vol. 51, no. 2, pp. 265–273, 2002.
- [12] 3. G. P. P. (3GPP), “Spatial channel model for Multiple Input Multiple Output (MIMO) simulations”, 3rd Generation Partnership Project (3GPP), TR 25.996, 2003.
- [13] A. Rodriguez-Herrera, S. Mcbeath, D. Pinckley, and D. Reed, “Link-to-system mapping techniques using a spatial channel model”, in *Vehicular Technology Conference, 2005. VTC-2005-Fall. 2005 IEEE 62nd*, vol. 3, 2005, pp. 1868–1871.
- [14] E. Tuomaala and Haiming Wang, “Effective SINR approach of link to system mapping in OFDM/multi-carrier mobile network”, in *2005 2nd Asia Pacific Conference on Mobile Technology, Applications and Systems*, 2005, 5 pp.–5.

Bibliography

- [15] WINNER I WP5, “Final report on link level and system level channel models”, *IST-2003-507581 WINNER I Deliverable D5.4*, 2005.
- [16] P. Almers, E. Bonek, A. Burr, N. Czink, M. Debbah, V. Degli-Esposti, H. Hofstetter, P. Kyösti, D. Laurenson, G. Matz, A. Molisch, C. Oestges, and H. Ozcelik, “Survey of channel and radio propagation models for wireless MIMO systems”, *EURASIP Journal on Wireless Communications and Networking*, 2007.
- [17] L. Hentila, P. Kyosti, M. Kaske, M. Narandzic, and M. Alatossava, “Matlab implementation of the winner phase II channel model ver1.1”, 2007, Available: http://projects.celtic-initiative.org/winner+/phase_2_model.html.
- [18] WINNER II WP1, “WINNER II channel models”, *IST-4-027756 WINNER II Deliverable D1.1.2*, 2007.
- [19] 3GPP, *Technical Specification Group Radio Access Networks; Deployment aspects (Release 8)*, [Online]. Available: <http://www.3gpp.org/ftp/Specs/html-info/25943.htm>, 2008.
- [20] 3. G. P. P. (3GPP), “LTE Physical Layer - General Description”, 3rd Generation Partnership Project (3GPP), TS 36.201, 2009.
- [21] M. ITU-R, “Guidelines for evaluation of radio interface technologies for IMT-Advanced”, *Report*, 2009.
- [22] J. C. Ikuno, M. Wrulich, and M. Rupp, “System Level Simulation of LTE Networks”, in *2010 IEEE 71st Vehicular Technology Conference*, May 2010, pp. 1–5.
- [23] S. Max, D. Bültmann, R. Jennen, and M. Schinnenburg, “Evaluation of IMT-advanced scenarios using the open wireless network simulator”, in *Int. ICST Conf. on Simulation Tools and Techniques*, Torremolinos, Malaga, Spain, 2010, p. 26.
- [24] S. Schwarz, C. Mehlführer, and M. Rupp, “Low complexity approximate maximum throughput scheduling for LTE”, in *2010 Conference Record of the Forty Fourth Asilomar Conference on Signals, Systems and Computers*, 2010, pp. 1563–1569.
- [25] Y. Li, F. Yu, S.-l. Zheng, and C.-l. Yang, “LTE System Level Simulation with MATLAB”, in *Int. Conf. Internet Technology and Applications (iTAP)*, 2011, pp. 1–4.
- [26] D. Molteni, M. Nicoli, and U. Spagnolini, “Performance of MIMO-OFDMA Systems in Correlated Fading Channels and Non-Stationary Interference”, *IEEE Transactions on Wireless Communications*, vol. 10, no. 5, pp. 1480–1494, May 2011.
- [27] G. Piro, L. Grieco, G. Boggia, F. Capozzi, and P. Camarda, “Simulating LTE Cellular Systems: An Open-Source Framework”, *IEEE Trans. Veh. Technol.*, vol. 60, no. 2, pp. 498–513, 2011.
- [28] A. Weber and A. Bestard, “Modeling of X-pol antennas for LTE system simulation”, in *8th International Symposium on Wireless Communication Systems (ISWCS)*, 2011, 2011, pp. 221–225.

-
- [29] 3. G. P. P. (3GPP), “Evolved Universal Terrestrial Radio Access (E-UTRA), Physical Channels and Modulation (Release 11)”, 3rd Generation Partnership Project (3GPP), TS 36.211, 2012.
- [30] ———, “Spatial channel model for Multiple Input Multiple Output (MIMO) simulations”, 3rd Generation Partnership Project (3GPP), TR 325.996, 2012.
- [31] M. Gerasimenko, S. Andreev, Y. Koucheryavy, A. Trushanin, V. Shumilov, M. Shashanov, and S. Sosnin, “Performance Comparison of System Level Simulators for 3GPP LTE Uplink”, in *Internet of Things, Smart Spaces, and Next Generation Networking*, ser. Lecture Notes in Computer Science, S. Andreev, S. Balandin, and Y. Koucheryavy, Eds., vol. 7469, Springer Berlin Heidelberg, 2012, pp. 186–197.
- [32] L. Liu, C. Oestges, J. Poutanen, K. Haneda, P. Vainikainen, F. Qutin, F. Tufvesson, and P. D. Doncker, “The COST 2100 MIMO channel model”, *IEEE Wireless Communications*, vol. 19, no. 6, pp. 92–99, 2012.
- [33] S. Ahmadi, *LTE-Advanced: A Practical Systems Approach to Understanding 3GPP LTE Releases 10 and 11 Radio Access Technologies*, ser. ITPro collection. Elsevier Science, 2013.
- [34] F. Fernandes, A. Ashikhmin, and T. L. Marzetta, “Inter-Cell Interference in Noncooperative TDD Large Scale Antenna Systems”, *IEEE Journal on Selected Areas in Communications*, vol. 31, no. 2, pp. 192–201, 2013.
- [35] X. Gao, F. Tufvesson, and O. Edfors, “Massive MIMO channels - Measurements and models”, in *2013 Asilomar Conference on Signals, Systems and Computers*, 2013, pp. 280–284.
- [36] J. Hoydis, S. ten Brink, and M. Debbah, “Massive MIMO in the UL/DL of Cellular Networks: How Many Antennas Do We Need?”, *IEEE Journal on Selected Areas in Communications*, vol. 31, no. 2, pp. 160–171, 2013.
- [37] J. C. Ikuno, “System Level Modeling and Optimization of the LTE Downlink”, <http://theses.eurasip.org/theses/479/system-level-modeling-and-optimization-of-the-lte/>, PhD thesis, E389, Technische Universität Wien, 2013.
- [38] M. K. Müller, S. Schwarz, and M. Rupp, “QoS investigation of proportional fair scheduling in LTE networks”, in *2013 IFIP Wireless Days (WD)*, 2013, pp. 1–4.
- [39] H. Q. Ngo, E. G. Larsson, and T. L. Marzetta, “Energy and Spectral Efficiency of Very Large Multiuser MIMO Systems”, *IEEE Transactions on Communications*, vol. 61, no. 4, pp. 1436–1449, 2013.
- [40] F. Rusek, D. Persson, B. K. Lau, E. Larsson, T. Marzetta, O. Edfors, and F. Tufvesson, “Scaling up MIMO: Opportunities and challenges with very large arrays”, *IEEE Signal Processing Magazine*, vol. 30, no. 1, pp. 40–60, 2013.
- [41] S. Schwarz, J. Ikuno, M. Simko, M. Taranetz, Q. Wang, and M. Rupp, “Pushing the limits of LTE: A survey on research enhancing the standard”, *IEEE Access*, vol. 1, pp. 51–62, 2013.

Bibliography

- [42] V. Vakilian, T. Wild, F. Schaich, S. ten Brink, and J. Frigon, “Universal-filtered multi-carrier technique for wireless systems beyond LTE”, in *IEEE Globecom Workshops*, 2013, pp. 223–228.
- [43] 3. G. P. P. (3GPP), “Study on 3D channel model for LTE”, 3rd Generation Partnership Project (3GPP), TR 36.873, 2014.
- [44] 3GPP TSG RAN WG-1, “R1-140048: Phase 2 calibration results for 3D channel model”, 3rd Generation Partnership Project (3GPP), Tech. Rep., 2014.
- [45] ——, “R1-143469: Summary of 3D-channel model calibration results”, 3rd Generation Partnership Project (3GPP), Tech. Rep., 2014.
- [46] A. Alkhateeb, G. Leus, and R. W. Heath, “Multi-layer precoding for full-dimensional massive MIMO systems”, in *48th Asilomar Conference on Signals, Systems and Computers*, 2014, pp. 815–819.
- [47] Z. Hu, R. Liu, S. Kang, X. Su, and J. Xu, “Work in progress: 3D beamforming methods with user-specific elevation beamfoming”, in *International Conference on Communications and Networking in China (CHINACOM)*, 2014, pp. 383–386.
- [48] S. Jaeckel *et al.*, “QuaDRiGa: A 3-D Multi-Cell Channel Model With Time Evolution for Enabling Virtual Field Trials”, *IEEE Transactions on Antennas and Propagation*, vol. 62, no. 6, pp. 3242–3256, 2014.
- [49] A. Kammoun, H. Khanfir, Z. Altman, M. Debbah, and M. Kamoun, “Preliminary results on 3D channel modeling: From theory to standardization”, *IEEE Journal on Selected Areas in Communications*, vol. 32, no. 6, pp. 1219–1229, 2014.
- [50] Y. Kim, H. Ji, J. Lee, Y. Nam, B. L. Ng, I. Tzanidis, Y. Li, and J. Zhang, “Full dimension mimo (FD-MIMO): the next evolution of MIMO in LTE systems”, *IEEE Wireless Communications*, vol. 21, no. 2, pp. 26–33, 2014.
- [51] E. Larsson, O. Edfors, F. Tufvesson, and T. Marzetta, “Massive mimo for next generation wireless systems”, *IEEE Communications Magazine*, vol. 52, no. 2, pp. 186–195, 2014.
- [52] Y. Wang, J. Xu, and L. Jiang, “Challenges of system-level simulations and performance evaluation for 5G wireless networks”, *IEEE Access*, vol. 2, pp. 1553–1561, 2014.
- [53] 3. G. P. P. (3GPP), “Elevation Beamforming/Full-Dimension MIMO for LTE”, 3rd Generation Partnership Project (3GPP), TR 36.897, 2015.
- [54] F. Ademaj, M. Taranetz, and M. Rupp, “Implementation, validation and application of the 3GPP 3D MIMO channel model in open source simulation tools”, in *2015 International Symposium on Wireless Communication Systems (ISWCS)*, 2015, pp. 721–725.
- [55] K. Bakowski, M. Rodziewicz, and P. Sroka, “System-level simulations of selected aspects of 5G cellular networks”, in *2015 International Symposium on Wireless Communication Systems (ISWCS)*, 2015, pp. 711–715.

-
- [56] R. He, Z. Zhong, B. Ai, and C. Oestges, “Shadow fading correlation in high-speed railway environments”, *IEEE Transactions on Vehicular Technology*, vol. 64, no. 7, pp. 2762–2772, 2015.
- [57] *Riverbed*, <http://www.riverbed.com/products/performance-management-control/opnet.html?redirect=opnet>, Jan. 2015. (visited on 01/30/2015).
- [58] M. Soszka, S. Berger, A. Fehske, M. Simsek, B. Butkiewicz, and G. Fettweis, “Coverage and Capacity Optimization in Cellular Radio Networks with Advanced Antennas”, in *WSA 2015; 19th International ITG Workshop on Smart Antennas*, 2015, pp. 1–6.
- [59] M. Soszka, S. Berger, A. Fehske, M. Simsek, B. Butkiewicz, and G. Fettweis, “Coverage and capacity optimization in cellular radio networks with advanced antennas”, in *Proceedings of WSA 2015 in 19th International ITG Workshop on Smart Antennas*, 2015, pp. 1–6.
- [60] A. Tall, Z. Altman, and E. Altman, “Virtual Sectorization: Design and Self-Optimization”, in *2015 IEEE 81st Vehicular Technology Conference (VTC Spring)*, May 2015, pp. 1–5.
- [61] M. Taranetz, T. Blazek, T. Kropfreiter, M. K. Müller, S. Schwarz, and M. Rupp, “Runtime precoding: Enabling multipoint transmission in LTE-Advanced system-level simulations”, *IEEE Access*, vol. 3, pp. 725–736, 2015.
- [62] 3GPP TSG RAN WG-1, “R1-160437: Spatial consistency modeling in drop based model”, 3rd Generation Partnership Project (3GPP), Tech. Rep., 2016.
- [63] F. Ademaj, M. Taranetz, and M. Rupp, “3GPP 3D MIMO Channel Model: A Holistic Implementation Guideline for Open Source SImulation Tools”, *EURASIP Journal on Wireless Communications and Networking*, vol. 2016, no. 1, p. 55, 2016. [Online]. Available: <https://doi.org/10.1186/s13638-016-0549-9>.
- [64] ——, “Evaluating the spatial resolution of 2D antenna arrays for massive MIMO transmissions”, in *2016 24th European Signal Processing Conference (EUSIPCO)*, 2016, pp. 1995–1999.
- [65] S. Baek, Y. Chang, J. Hwang, S. Hur, and B. Kim, “A study on correlation properties of shadow fading of millimeter wave frequency spectrum”, in *2016 13th IEEE Annual Consumer Communications Networking Conference (CCNC)*, 2016, pp. 511–516.
- [66] R. W. Heath, N. González-Prelcic, S. Rangan, W. Roh, and A. M. Sayeed, “An Overview of Signal Processing Techniques for Millimeter Wave MIMO Systems”, *IEEE Journal of Selected Topics in Signal Processing*, vol. 10, no. 3, pp. 436–453, 2016.
- [67] T. L. Marzetta, *Fundamentals of Massive MIMO*, 1st ed. Cambridge University Press, 2016.
- [68] J. Medbo, P. Kyosti, K. Kusume, L. Raschkowski, K. Haneda, T. Jamsa, V. Nurmela, A. Roivainen, and J. Meinila, “Radio propagation modeling for 5G mobile and wireless communications”, *IEEE Communications Magazine*, vol. 54, no. 6, pp. 144–151, 2016.

Bibliography

- [69] M. Rupp, S. Schwarz, and M. Taranetz, *The Vienna LTE-Advanced Simulators: Up and Downlink, Link and System Level Simulation*, 1st ed., ser. Signals and Communication Technology. Springer Singapore, 2016.
- [70] S. Schwarz and M. Rupp, “Society in motion: challenges for LTE and beyond mobile communications”, *IEEE Communications Magazine*, vol. 54, no. 5, pp. 76–83, May 2016.
- [71] 3. G. P. P. (3GPP), “NR; Multiplexing and channel coding”, 3rd Generation Partnership Project (3GPP), TS 38.212, 2017.
- [72] ——, “Study on channel model for frequencies from 0.5 to 100GHz”, 3rd Generation Partnership Project (3GPP), TR 38.901, 2017.
- [73] ——, “Study on New Radio (NR) access technology”, 3rd Generation Partnership Project (3GPP), TR 38.912, 2017.
- [74] F. Ademaj, M. K. Müller, S. Schwarz, and M. Rupp, “Modeling of Spatially Correlated Geometry-Based Stochastic Channels”, in *2017 IEEE 86th Vehicular Technology Conference (VTC-Fall)*, 2017, pp. 1–6.
- [75] K. Guan, X. Lin, D. He, B. Ai, Z. Zhong, Z. Zhao, D. Miao, H. Guan, and T. Kürner, “Scenario modules and ray-tracing simulations of millimeter wave and terahertz channels for smart rail mobility”, in *2017 11th European Conference on Antennas and Propagation (EUCAP)*, 2017, pp. 113–117.
- [76] P. Guan, D. Wu, T. Tian, J. Zhou, X. Zhang, L. Gu, A. Benjebbour, M. Iwabuchi, and Y. Kishiyama, “5G field trials: OFDM-based waveforms and mixed numerologies”, *IEEE Journal on Selected Areas in Communications*, vol. 35, no. 6, pp. 1234–1243, 2017.
- [77] D. He, B. Ai, K. Guan, Z. Zhong, B. Hui, J. Kim, H. Chung, and I. Kim, “Channel Measurement, Simulation, and Analysis for High-Speed Railway Communications in 5G Millimeter-Wave Band”, *IEEE Transactions on Intelligent Transportation Systems*, pp. 1–15, 2017.
- [78] H. Ji *et al.*, “Overview of Full-Dimension MIMO in LTE-Advanced Pro”, *IEEE Communications Magazine*, vol. 55, no. 2, pp. 176–184, 2017.
- [79] L. Marijanovic, S. Schwarz, and M. Rupp, “Intercarrier interference of multiple access UFMC with flexible subcarrier spacings”, in *2017 25th European Signal Processing Conference (EUSIPCO)*, 2017, pp. 888–892.
- [80] R. Nissel, “Filter Bank Multicarrier Modulation for Future Wireless Systems”, PhD thesis, E389, Technische Universität Wien, 2017. [Online]. Available: http://publik.tuwien.ac.at/files/publik_265168.pdf.
- [81] R. Nissel, S. Schwarz, and M. Rupp, “Filter Bank Multicarrier Modulation Schemes for Future Mobile Communications”, *IEEE Journal on Selected Areas in Communications*, vol. 35, no. 8, pp. 1768–1782, 2017.

-
- [82] K. Sakaguchi *et al.*, “Where, When, and How mmWave is Used in 5G and Beyond”, *IEICE Transactions on Electronics*, vol. E100.C, no. 10, pp. 790–808, 2017.
- [83] 3. G. P. P. (3GPP), “Base Station (BS) radio transmission and reception”, 3rd Generation Partnership Project (3GPP), TS 36.104, May 2018.
- [84] F. Ademaj, S. Schwarz, K. Guan, and M. Rupp, “Ray-Tracing based Validation of Spatial Consistency for Geometry-Based Stochastic Channels”, in *2018 IEEE 88th Vehicular Technology Conference (VTC-Fall)*, 2018, pp. 1–5.
- [85] M. Han, J. W. Lee, C. G. Kang, and M. J. Rim, “5G K-SimSys: Open/Modular/Flexible System Level Simulator for 5G System”, in *2018 IEEE International Symposium on Dynamic Spectrum Access Networks (DySPAN)*, 2018, pp. 1–2.
- [86] D. He, B. Ai, K. Guan, L. Wang, Z. Zhong, and T. Kürner, “The Design and Applications of High-Performance Ray-Tracing Simulation Platform for 5G and Beyond Wireless Communications: A Tutorial”, *IEEE Communications Surveys Tutorials*, pp. 1–1, 2018.
- [87] M. K. Müller, F. Ademaj, T. Dittrich, A. Fastenbauer, B. R. Elbal, A. Nabavi, L. Nagel, S. Schwarz, and M. Rupp, “Flexible multi-node simulation of cellular mobile communications: The Vienna 5G System Level Simulator”, *EURASIP Journal on Wireless Communications and Networking*, vol. 2018, no. 1, p. 17, 2018.
- [88] R. Nissel and M. Rupp, “Pruned DFT-Spread FBMC: Low PAPR, Low Latency, High Spectral Efficiency”, *IEEE Transactions on Communications*, vol. 66, no. 10, pp. 4811–4825, 2018.
- [89] S. Pratschner, B. Tahir, L. Marijanovic, M. Mussbah, K. Kirev, R. Nissel, S. Schwarz, and M. Rupp, “Versatile mobile communications simulation: the Vienna 5G Link Level Simulator”, *EURASIP Journal on Wireless Communications and Networking*, vol. 2018, no. 1, 2018.
- [90] 3GPP 3D Channel Model Standalone MATLAB Code, <http://www.nt.tuwien.ac.at/downloads/>, 2019. (visited on 10/06/2019).
- [91] F. Ademaj and S. Schwarz, “Spatial Consistency of Multipath Components in a Typical Urban Scenario”, in *European Conference on Antennas and Propagation (EuCAP)*, 2019, pp. 1–5.
- [92] F. Ademaj, S. Schwarz, T. Berisha, and M. Rupp, “A Spatial Consistency Model for Geometry-based Stochastic Channels”, *submitted to IEEE Access*, 2019. [Online]. Available: <https://owncloud.nt.tuwien.ac.at/index.php/s/igAyCWnjRH3QFyL>.
- [93] GNS3, <http://www.gns3.com/>, May 2019.
- [94] Hurricane III WAN Emulation and Network Simulation, <https://packetstorm.com/packetstorm-products/hurricane-iii-software/>, 2019. (visited on 02/06/2019).
- [95] IT++, <http://itpp.sourceforge.net/4.3.1/>, May 2019. (visited on 05/08/2019).
- [96] L. Marijanovic, S. Schwarz, and M. Rupp, “Optimal Resource Allocation with Flexible Numerology”, in *16th International Conference on Communication Systems (ICC)*, 2019.

Bibliography

- [97] *Nomor System Level Simulation*, <http://www.nomor.de/home/solutions-and-products/system-level-simulation>, 2019. (visited on 02/06/2019).
- [98] *ns-2*, http://nsnam.sourceforge.net/wiki/index.php/User_Information, May 2019.
- [99] *ns-3*, <http://www.nsnam.org/>, May 2019.
- [100] *OMNeT++*, <http://www.omnetpp.org>, 2019. (visited on 02/06/2019).
- [101] *Openstreetmap*, 2019. [Online]. Available: <http://www.openstreetmap.org/>.
- [102] S. Pratschner, M. K. Müller, F. Ademaj, A. Nabavi, B. Tahir, S. Schwarz, and M. Rupp, “Verification of the vienna 5g link and system level simulators and their interaction”, in *2019 16th IEEE Annual Consumer Communications Networking Conference (CCNC)*, Jan. 2019, pp. 1–8.
- [103] *Ray-tracing*, <http://raytracer.cloud/>, 2019.
- [104] *SketchUp*, <http://www.sketchup.com/products/sketchup-pro/>, 2019. (visited on 01/04/2019).
- [105] *Vienna Cellular Communication Simulators*, <https://www.nt.tuwien.ac.at/research/mobile-communications/vccs/>, 2019. (visited on 10/06/2019).
- [106] *Vienna LTE-A Downlink System-Level Simulator*, <http://www.nt.tuwien.ac.at/research/mobile-communications/vccs/vienna-lte-a-simulators/lte-a-downlink-system-level-simulator/>, 2019. (visited on 10/06/2019).
- [107] E. Zöchmann, M. Hofer, M. Lerch, S. Pratschner, L. Bernado, J. Blumenstein, S. Caban, S. Sangodoyin, H. Groll, T. Zemen, A. Prokes, M. Rupp, A. F. Molisch, and C. F. Mecklenbräuker, “Position-Specific Statistics of 60 GHz Vehicular Channels During Overtaking”, *IEEE Access*, vol. 7, pp. 14 216–14 232, 2019.